Universidade de Aveiro Departamento de Física
2013

Ismael Filipe Correia de Castro

Desenvolvimento de câmaras gama de alta resolução baseadas em foto-sensores de silício

Development of high-resolution gamma cameras based on silicon photosensors

Universidade de Aveiro Departamento de Física
2013

Ismael Filipe Correia de Castro

Desenvolvimento de câmaras gama de alta resolução baseadas em foto-sensores de silício

Development of high-resolution gamma cameras based on silicon photosensors

Universidade de Aveiro Departamento de Física
2013

Ismael Filipe Correia de Castro

Desenvolvimento de câmaras gama de alta resolução baseadas em foto-sensores de silício

Development of high-resolution gamma cameras based on silicon photosensors

Tese apresentada à Universidade de Aveiro para cumprimento dos requisitos necessários à obtenção do grau de Doutor em Engenharia Física, realizada sob a orientação científica do Doutor João Filipe Calapez de Albuquerque Veloso, Professor Auxiliar do Departamento de Física da Universidade de Aveiro e co-orientação do Doutor Joaquim Marques Ferreira dos Santos, Professor Catedrático da Faculdade de Ciências e Tecnologia da Universidade de Coimbra.

Apoio financeiro da FCT (Bolsa de Doutoramento com a referência SFRH / BD / 61255 / 2009) e do FSE/FEDER no âmbito do Quadro de Referência Estratégico Nacional (QREN), através dos programas COMPETE e AdI, projeto GAMACAM (1607).

Aos meus pais e irmãs.

o júri / the jury

presidente / president

Doutor Carlos Manuel Martins da Costa
Professor Catedrático do Departamento de Economia, Gestão e Engenharia Industrial da Universidade de Aveiro

vogais / examiners committee

Doutor Joaquim Marques Ferreira dos Santos
Professor Catedrático da Faculdade de Ciências e Tecnologia da Universidade de Coimbra

Doutora Maria da Conceição Abreu e Silva
Professora Catedrática Aposentada da Faculdade de Ciências e Tecnologia da Universidade do Algarve

Doutor Luís Filipe dos Santos Garcia Peralta
Professor Auxiliar com Agregação da Faculdade de Ciências da Universidade de Lisboa

Doutor Augusto Marques Ferreira da Silva
Professor Auxiliar do Departamento de Eletrónica, Telecomunicações e Informática da Universidade de Aveiro

Doutor João Filipe Calapez de Albuquerque Veloso
Professor Auxiliar do Departamento de Física da Universidade de Aveiro

agradecimentos /
acknowledgements

Ao longo dos últimos anos foram muitas as pessoas que contribuiram para este trabalho e que o apoiaram direta ou indiretamente. Como tal, tenho a agradecer a muito boa gente!

Um grande obrigado ao Prof. Doutor João Veloso, por me ter recebido no seu grupo de investigação, dando-me assim oportunidade de fazer parte de uma verdadeira *dream team*. A sua experiência e conhecimento científico traduziram-se em valiosas dicas no acompanhar dos trabalhos, simplificando o que por vezes parecia complicado!

Agradeço também ao Prof. Doutor Joaquim Santos, por ter aceitado co-orientar este trabalho e pela disponibilidade demonstrada sempre que necessário.

Ao Doutor António Soares, não só por ser a principal pessoa por detrás da ideia e do trabalho que serviu de ponto de partida para esta tese, mas também por sempre ter sido uma fonte de motivação, apoiando e guiando o trabalho no melhor caminho.

A todos os membros da equipa DRIM, incluindo o "grande chefe", não posso deixar de agradecer a amizade e o companheirismo. Obrigado pela ajuda sempre que foi precisa, por tudo o que aprendi com vocês e pelos momentos de partilha e boa disposição... à Ana Luísa, Arouca, Cacia, Lara, Moutinho, Carlos, Tiago, Pedro, Fábio... e também à Andrêa, Hugo e Daniel.

Pela execução de várias peças e serviços indispensáveis aos trabalhos experimentais, obrigado aos técnicos do departamento de Física: Ivo Mateus, Miguel Rocha, Júlio Gonçalves e Francisco Reis.

Obrigado ao Doutor Patrick Sousa por gentilmente ter cedido a fonte de ^{57}Co utilizada nos estudos e também ao Eng. Jorge Isidoro, do serviço de Medicina Nuclear dos Hospitais da Universidade de Coimbra, pelas amostras de ^{99m}Tc disponibilizadas. Por ter tornado possível o estudo imagiológico de um ratinho injetado com um radiofármaco baseado em ^{99m}Tc, agradeço especialmente à Prof. Doutora Cristina Santos pelo seu tempo e amabilidade.

O desenvolvimento de várias componentes eletrónicas do protótipo de maior dimensão foi feito em colaboração com o Prof. Ian Cullum de Inglaterra e a empresa ISA S.A., em Coimbra, pelo que devo um agradecimento e reconhecimento pelo trabalho de ambas as partes. Em particular, obrigado ao Ian pela preciosa ajuda na resolução de problemas e aos engenheiros Miguel Ferreira, Rodrigo Ferreira, Fernando Muchacho, Álvaro Combo e Micael Santos, pelo desenvolvimento das placas de alimentação dos SiPMs, assim como pela montagem de outras placas e apoio com o *software*.

Por todo o suporte e apoio que sempre me deram, o agradecimento mais especial vai para os meus pais, irmã mais velha e também à restante família. A todos os amigos que fiz durante estes anos em Aveiro e também aos de mais longa data, alguns distantes mas sempre queridos, obrigado. Por último, mas não menos importante, à Agnese... paldies mīļā!

Palavras Chave medicina nuclear, câmara gama, fibras ópticas, fotomultiplicadores de silício.

Resumo

O desenvolvimento de uma câmara gama compacta com alta resolução espacial é de grande interesse em Medicina Nuclear, como meio de aumentar a sensibilidade dos exames de cintigrafia e assim permitir a deteção precoce de pequenos tumores.

Na sequência da introdução da câmara gama com fibras óticas por Soares *et al.* e da evolução dos fotodiodos para fotomultiplicadores de silício (SiPMs) altamente sensíveis, esta tese explora o desenvolvimento de uma câmara gama com fibras óticas usando SiPMs para obter a informação da posição dos eventos de cintilação num cristal de CsI(Na) contínuo. O design é altamente flexível permitindo cobrir diferentes áreas e desenvolver câmaras compactas, com muito pouca área morta na periferia.

Após testes iniciais que confirmaram a viabilidade da aplicação dos SiPMs, um protótipo com 5×5 cm^2 foi montado e testado à temperatura ambiente, num campo de visão ativo de 10×10 mm^2. A calibração e caracterização de propriedades intrínsecas deste protótipo foram efetuadas utilizando ^{57}Co, enquanto que medições extrínsecas foram realizadas com um colimador de buracos paralelos de alta resolução e ^{99m}Tc. Adicionalmente, o protótipo desenvolvido foi usado para produzir a imagem de um ratinho injetado com um radiofármaco.

Os resultados confirmam o grande potencial dos SiPMs quando aplicados numa câmara gama com fibras óticas, atingindo uma performance em resolução espacial superior à da câmara Anger tradicional. Além disso, a performance pode ser melhorada por uma otimização das condições experimentais, no sentido de minimizar e controlar os efeitos indesejáveis do ruído térmico e da não-uniformidade de resposta de múltiplos SiPMs.

O desenvolvimento e caracterização parcial de uma câmara com 10×10 cm^2 para aplicação clínica são também apresentados.

Keywords nuclear medicine, gamma camera, wavelength-shifting fibres, silicon photomultipliers.

Abstract

The development of a compact gamma camera with high spatial resolution is of great interest in Nuclear Medicine as a means to increase the sensitivity of scintigraphy exams and thus allow the early detection of small tumours.

Following the introduction of the wavelength-shifting fibre (WSF) gamma camera by Soares *et al.* and evolution of photodiodes into highly sensitive silicon photomultipliers (SiPMs), this thesis explores the development of a WSF gamma camera using SiPMs to obtain the position information of scintillation events in a continuous CsI(Na) crystal. The design is highly flexible, allowing the coverage of different areas and the development of compact cameras, with very small dead areas at the edges.

After initial studies which confirmed the feasibility of applying SiPMs, a prototype with 5×5 cm^2 was assembled and tested at room temperature, in an active field-of-view of 10×10 mm^2. Calibration and characterisation of intrinsic properties of this prototype were done using ^{57}Co, while extrinsic measurements were performed using a high-resolution parallel-hole collimator and ^{99m}Tc. In addition, a small mouse injected with a radiopharmaceutical was imaged with the developed prototype.

Results confirm the great potential of SiPMs when applied in a WSF gamma camera, achieving spatial resolution performance superior to the traditional Anger camera. Furthermore, performance can be improved by an optimisation of experimental conditions, in order to minimise and control the undesirable effects of thermal noise and non-uniformity of response of multiple SiPMs.

The development and partial characterisation of a larger SiPM WSF gamma camera with 10×10 cm^2 for clinical application are also presented.

CONTRIBUTIONS

The work done under this doctoral program resulted in several contributions, through the publication of articles in scientific journals and presentations at international conferences and workshops.

Publications

Papers in international peer-reviewed journals

- **I. F. C. Castro**, A. J. D. Soares, L. M. Moutinho, M. A. Ferreira, R. Ferreira, A. Combo, F. Muchacho and J. F. C. A. Veloso, *"Characterization of a small CsI(Na)-WSF-SiPM gamma camera prototype using ^{99m}Tc",* Journal of Instrumentation, 8 C03008, 2013.
- **I. F. C. Castro**, A. J. D. Soares, L. M. Moutinho and J. F. C. A. Veloso, *"Development of a light readout based on silicon photomultipliers for a wavelength-shifting fibre gamma camera",* Nuclear Instruments and Methods in Physics Research Section A, vol. 695, pp. 298-302, 2012.
- **I. F. C. Castro**, A. J. D. Soares, L. M. Moutinho and J. F. C. A. Veloso, *"Small prototype gamma camera based on wavelength-shifting fibres",* Journal of Instrumentation, 7 C01043, 2012.

Papers in conference proceedings

- **I. F. C. Castro**, A. J. D. Soares and J. F. C. A. Veloso, *"Impact of dark counts in low-light level SiPM multi-readout applications",* IEEE Nuclear Science Symposium and

Medical Imaging Conference Record, pp. 1592-1596, Oct. 19-25, 2009.

- **I. F. C. Castro**, A. J. D. Soares, L.M. Moutinho and J. F. C. A. Veloso, *"Characterization of a SiPM-based Wavelength-Shifting Fibre Gamma Camera Using ^{99m}Tc",* Digest of the Riga Technical University 53rd International Scientific Conference dedicated to the 150th Anniversary and 1st Congress of World Engineers and Riga Polytechnical Institute / RTU Alumni, p. 681 , Oct. 11-12, 2012.

Communications

Oral Communications

- **I. F. C. Castro**, L. M. Moutinho, A. J. D. Soares and J. F. C. A. Veloso, *"Characterization of a small CsI(Na)-WSF-SiPM gamma camera prototype using ^{99m}Tc".* 14th iWoRID - International Workshop on Radiation Imaging Detectors, July 1-5 2012, Figueira da Foz, Portugal.
- **I. F. C. Castro**, L. M. Moutinho, A. J. D. Soares and J. F. C. A. Veloso, *"CsI(Na) wavelength-shifting fibre gamma camera using SiPMs".* IDPASC School on Digital Counting Photosensors for Extreme Low Light Levels, April 16-20 2012, Lisboa, Portugal.
- **I. F. C. Castro**, L. M. Moutinho, A. J. D. Soares and J. F. C. A. Veloso, *"Development of new design of high-resolution gamma camera for scintimammography".* PPHSS - Portuguese Physics for Health Summer School, July 26-28 2010, Covilhã, Portugal.

Poster Communications

- **I. F. C. Castro**, A. J. D. Soares, L. M. Moutinho, M.A. Ferreira, R. Ferreira, A. Combo, F. Muchacho, A. C. Santos and J. F. C. A. Veloso, *"Wavelength-shifting fibre gamma camera with SiPMs: first small animal tests".* Submission accepted for poster presentation at the IEEE Nuclear Science Symposium and Medical Imaging Conference, October 27-November 2 2013, Seoul, Korea.
- **I. F. C. Castro**, L. M. Moutinho, A. J. D. Soares and J. F. C. A. Veloso, *"Characterization of SiPM-based wavelength-shifting fibre gamma camera using ^{99m}Tc".* ISBEMP - International Symposium on Biomedical Engineering and Medical Physics, October 10-12 2012, Riga, Latvia.
- **I. F. C. Castro**, L. M. Moutinho, A. J. D. Soares and J. F. C. A. Veloso, *"Development of gamma camera prototype using wavelength-shifting fibres and SiPMs".* IEEE Nuclear Science Symposium and Medical Imaging Conference, October 23-29 2011, Valencia, Spain.

- **I. F. C. Castro**, L. M. Moutinho, A. J. D. Soares and J. F. C. A. Veloso, *"First steps toward small prototype gamma camera based on wavelength-shifting fibres"*. 13th iWoRID - International Workshop on Radiation Imaging Detectors, July 3-7 2011, Zürich, Switzerland.

- I. F. C. Castro, **L. M. Moutinho**, A. J. D. Soares and J. F. C. A. Veloso, *"Initial development of a wavelength-shifting fibre gamma camera using SiPMs"*. NDIP - 6th International Conference on New Developments in Photodetection, July 4-8 2011, Lyon, France.

- **I. F. C. Castro**, A. J. D. Soares and J. F. C. A. Veloso, *"Impact of dark counts in low-light level SiPM multi-readout applications"*. IEEE Nuclear Science Symposium and Medical Imaging Conference, October 25-31 2009, Orlando, Florida, USA.

CONTENTS

LIST OF ABBREVIATIONS AND SYMBOLS

ADC	analog-to-digital converter
APD	avalanche photodiode
ASIC	application-specific integrated circuit
BSGI	breast-specific gamma imaging
CCD	charge-coupled device
CMOS	complementary metal-oxide semiconductor
CT	computed tomography
CZT	cadmium zinc telluride
FOV	field-of-view
FPGA	field-programmable gate array
FWHM	full width at half maximum
G-APD	Geiger-mode avalanche photodiode
GUI	graphical user interface
HMDP	hydroxymethylene diphosphonate
IC	integrated circuit
LED	light-emitting diode
LEHR	low energy high resolution
LSO	lutetium oxyorthosilicate
LYSO	lutetium yttrium oxyorthosilicate
MaPMT	multi-anode photomultiplier tube
MCA	multi-channel analyser
MDP	methylene diphosphonate
MDR	mini delta ribbon
MPPC	multi-pixel photon counter
MRI	magnetic resonance imaging
MRS	metal-resistor-semiconductor

NIM nuclear instrumentation module

p.e. photon equivalent

PCB printed circuit board

PDE photon detection efficiency

PET positron emission tomography

PMMA poly(methyl methacrylate)

PMT photomultiplier tube

QE quantum efficiency

SiPM silicon photomultiplier

SCD source-to-collimator distance

SDD silicon drift detector

SNR signal-to-noise ratio

SPECT single photon emission computed tomography

SPI serial peripheral interface

SSPD solid-state photodetector

TTL transistor-transistor logic

UFOV useful field-of-view

USB universal serial bus

WSF wavelength-shifting fibre

LIST OF FIGURES

INTRODUCTION

Since the invention of the first nuclear medicine imaging devices in the mid-twentieth century, there has been a tremendous evolution in the field of nuclear medicine instrumentation, which allowed very important advances in the quality of the diagnostic information provided. Despite this, for single gamma photon imaging, the main device used remains the Anger camera, which has reached a very mature level of development and is found in every nuclear medicine department, due to its robustness and versatility, being able to perform many different types of studies including whole body imaging. The performance of the Anger camera has been improved throughout the years mainly due to technological advances of its components, rather than by changes in the overall design itself. However, new technologies and alternative designs have also been introduced and considerable research has been dedicated to the development of small field-of-view imagers for specific organs and applications, in order to overcome the limitations of large Anger-design scanners, particularly in the detection of breast cancer through scintimammography.

This thesis describes the work carried out at University of Aveiro to develop a small gamma camera prototype, based on wavelength-shifting fibre (WSF) readout of the position of interaction of gamma rays in a CsI(Na) scintillator crystal. The camera design is based on a concept previously introduced by Soares *et al.* around 2000, but applies a new type of photodetector, the silicon photomultiplier (SiPM), which changes the readout concept. The SiPM is the latest advance in the area of semiconductor photodetectors for low light levels, basically consisting of a combination of many individual avalanche photodiodes (APDs) operating in Geiger-mode. This results in a device with a very high gain and photodetection efficiency, capable of single photon counting. Due to these and other interesting properties such as compactness, low power consumption and insensitivity to magnetic fields, SiPMs are

currently replacing the traditional photomultiplier tubes (PMT)s and also APDs in many other Physics experiments and nuclear medicine applications, *e.g.* in positron emission tomography combined with magnetic resonance imaging (PET/MRI). In the case of the WSF gamma camera, the application of SiPMs aims primarily at improving the spatial resolution by increasing the efficiency of light detection from the WSFs, but it also allows building a more compact and less power consuming camera. Better scintimammography images obtained through higher spatial resolution and improved positioning of a compact and portable gamma camera around the breast would allow the earlier detection of sub-cm tumours, for which typical scintigraphy has poor sensitivity.

The document is divided in seven chapters and organised as follows.

The first chapter aims to introduce the physical concepts and principles associated with the gamma camera, its basic constituents and performance parameters, as well as its role in nuclear medicine and more particularly in breast cancer detection. The concept of WSF gamma camera is presented, together with a background of previous studies and facts which served as a motivation for this work.

Chapter 2 is dedicated to a review of current gamma camera technologies, placing the WSF gamma camera in context with other developments and latest advances in the field.

Chapter 3 presents SiPM technology, including experimental studies to determine dark noise characteristics of selected SiPM devices and simulations to evaluate the impact of this noise in low-level SiPM multi-readout applications such as the WSF gamma camera. Further experimental evaluation of the feasibility of applying SiPMs in a WSF gamma camera is made in Chapter 4, particularly considering the influence of readout electronics and temperature in the efficiency of CsI(Na) scintillation light readout. This chapter then focuses in the gradual experimental assembly of a small 10×10 mm^2 CsI(Na)-WSF-SiPM gamma camera prototype and its intrinsic characterisation with ^{57}Co.

Chapter 5 evaluates the imaging performance of the developed prototype using ^{99m}Tc and a parallel-hole collimator, which allowed performing extrinsic measurements and testing the camera in more realistic conditions. This included imaging a mouse injected with ^{99m}Tc-HMDP.

The development and assembly of a larger prototype with 10×10 cm^2 is reported in chapter 6, where issues related to the scaling up are addressed.

In conclusion, the final chapter discusses and summarises the overall achievements of this work, as well as the future work that can follow.

CHAPTER

1

BACKGROUND AND MOTIVATION

1.1 Principles of nuclear medicine imaging

Nuclear medicine imaging studies are based on the tracer principle: a small quantity of a compound labelled with a radioactive element, called radiopharmaceutical, is administered to the patient and its distribution within the body is ascertained by externally detecting the emitted gamma rays with a specialised camera. The γ-ray energies of interest for clinical studies are those above 80 keV, for which the photons can travel through several cm of human tissue without being attenuated. The radiopharmaceutical is normally injected in the patient, but can also be inhaled or ingested, and its biodistribution after some time will reflect the physiological behaviour of the compound, revealing blood flow, metabolism, receptor binding and other phenomena happening on a molecular and cellular level. As a result, this type of medical imaging is named molecular imaging. Its applications in diagnosis, therapy and research in medicine are numerous, such as heart, lung, kidney or brain perfusion studies and, most frequently, in oncology, for tumour localisation and identification of metastases.

Molecular imaging can be divided in planar (2D) and tomographic (3D) techniques. A gamma camera allows obtaining planar images of the radiopharmaceutical's distribution in the body, in a technique known as scintigraphy. When several images are acquired from different angles, a 3D image can be reconstructed. This is usually achieved using specialised SPECT scanners (single photon emission computed tomography), with one or more detection heads around the patient's body or organ, such as the one shown in Figure 1.1. More cameras mean higher sensitivity, which is needed to minimise both the acquisition time per projection and the radiation dose administered to the patient, while gathering sufficient image statistics.

Figure 1.1: Gamma camera with 3 detectors, used for neuroimaging studies.

1.1.1 Positron emission tomography

Another tomographic technique of expanding use in nuclear medicine is positron emission tomography (PET), conceptually different from single-photon imaging. In PET, the radiopharmaceuticals used are positron emitters, which usually have a much shorter half-life time, in the order of minutes/hours. Following emission, the positron travels a short distance in the body until it annihilates with an electron, generating two oppositely directed 511 keV gamma photons. Positron range is a physical limiting factor to the spatial resolution of PET images, varying with positron kinetic energy and propagation medium and usually being less than 2 mm. The most frequently used radionuclide in PET is ^{18}F, with a positron mean range of 0.64 mm in water [1] and a relatively long half-life time of 109.8 minutes. It is commonly used to label 2-deoxy-2-^{18}F-fluoro-β-D glucose (^{18}F-FDG), a glucose analogue used for tumour detection [2].

Since gamma emission is isotropic and the two 511 keV photons generated in each event need to be detected in coincidence, a complete ring of detectors is required in PET. Each coincidence defines a line of response and from the many lines detected, dedicated algorithms reconstruct a 3D map of the radiopharmaceutical's biodistribution. Coincidence imaging eliminates the need for the type of collimators used in single photon imaging and therefore PET has a much higher sensitivity.

PET detector modules have undergone a great development in the last decades, as a result of extensive research, with most efforts being focused on scintillator-based detectors. Initial modules were composed of segmented BGO (bismuth germanate) scintillator crystals coupled to PMTs, but faster and brighter crystals have been introduced, like LYSO (lutetium yttrium oxyorthosilicate) and $LaBr_3$ (lanthanum bromide). These allowed reducing the width of the coincidence timing window, further improving the accuracy and count-rate capability of PET scanners. Concurrently, intense developments in photodetectors, electronics and techniques to reduce positioning errors such as the measurement of the photons' time of flight [3] or the depth of interaction in the crystals [4], significantly contributed to the improvement of PET performance, superior to single photon emission imaging. The spatial resolution achieved by whole-body PET scanners is around 4 mm FWHM (full width at half maximum) in the reconstructed image, while smaller dedicated PET tomographs used for small animal imaging and research have reached a spatial resolution of about 1 mm FWHM [5, 6].

PET raises great interest in clinical research due to its capacity for imaging compounds labeled with biologically important atoms such as carbon, nitrogen and oxygen. However, the main disadvantage of PET technology is its high cost, proportional to the complexity of the detector system. Moreover, almost all of the positron emitting radionuclides used in PET scans are produced in a cyclotron. Consequently, because of their very short half-life, a cyclotron and a large support infrastructure are required nearby.

Functional vs. anatomic imaging

The results of molecular imaging scans are intrinsically functional images, as they provide information regarding body metabolism and organ function, with very little structural detail of the body's anatomic features. In contrast, X-ray computed tomography (CT) or magnetic resonance images provide very detailed anatomic information but generally do not relate to function, thus playing a complementary role (exceptions are in the use of special contrast agents). Combining these two different types of imaging, image fusion software has been developed to merge nuclear medicine images with CT or MRI images and hybrid scanners have been introduced (*e.g.* PET/CT). In this way, it is possible to visualise the precise anatomic localisation of functional abnormalities.

In addition, all of the above-mentioned nuclear medicine modalities can be used to perform dynamic studies, by acquiring a series of images in time. In many cases, dynamic imaging allows obtaining functional information that wouldn't be possible to get from a static image.

1.2 Breast cancer detection

1.2.1 Statistics

Breast cancer is the most prevalent type of neoplasm in the world, especially in women of more developed countries but also when considering both sexes and the global population, as illustrated in Figure 1.2. In 2008, 5.2 million cases were registered and one in six cancer survivors had been diagnosed with it within the previous 5 years [7].

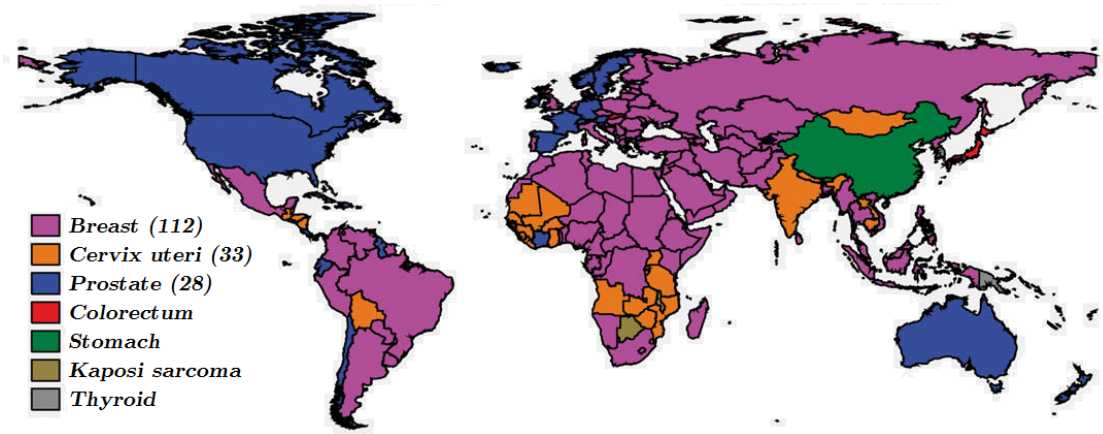

Figure 1.2: Most prevalent type of cancer in 2008, for both sexes in 184 countries (5-year prevalence) (from [7]).

According to estimates for the European Union in 2013 [8], breast cancer is still the first cause of cancer mortality in women (15%), but likely to be surpassed by lung cancer in 2015. In the United States, this has occurred already in 1987. In 2008, estimated rates of cancer-related deaths in U.S. women were 26% for lung and bronchus and 15% for breast [9].

1.2.2 Mammography and scintimammography

The main motivation for the development of new gamma cameras is the need to improve the small-tumour sensitivity of scintigraphy exams, particularly scintimammography exams. To realise this need, it is important to understand the technique and its shortcomings. It is also important to have a clear notion of the difference between sensitivity and specificity, when evaluating the result of a clinical test. While sensitivity measures the ability to correctly identify patients with a particular disease (percentage of true positives), specificity measures the ability to exclude patients without it (percentage of true negatives).

$$Sensitivity = \frac{true\,positives}{true\,positives + false\,negatives} \tag{1.1}$$

$$Specificity = \frac{true\,negatives}{true\,negatives + false\,positives} \tag{1.2}$$

Even though X-ray mammography has a very high sensitivity, which is why it is the standard screening method for breast cancer together with clinical breast examination, it produces a considerable amount of false positive results. The reason for this is because it cannot clearly distinguish between benign and malign masses, and its sensitivity decreases as the breast tissue density increases, a fact which is aggravated by the strong association demonstrated between breast density and the risk of developing breast cancer [10, 11]. Therefore, many suspicious mammograms are considered positive results when in fact they turn out to be benign masses, calcifications or even just naturally denser tissue, more frequent in younger women. These false positive results and their consequences constitute the biggest problem of X-ray mammography screening. For instance, a study based on 10,000 mammograms performed over 10 years estimates that among women who do not have breast cancer, 18.6% will undergo a biopsy after 10 mammograms [12]. Also, the study assesses the costs of evaluating false positive results to be about one third of the amount spent for the screening itself, in addition to being time consuming and distressful for the patients.

Scintigraphy exams are highly specific for malignant tumours and thus have a very low rate of false positives. However, despite not being affected by breast tissue density, implants or scars, scintimammography lacks sensitivity to detect small sub-cm tumours. This is due to intrinsic limitations of standard gamma cameras, namely their insufficient spatial resolution and their bulkiness which causes breast positioning issues, preventing the obtention of the best projection. The need to overcome these limitations is essential to allow the early detection of small tumours, a determinant factor for survival rates. Nevertheless, dedicated breast cameras have been developed and research is ongoing toward this goal, with scintimammography already being recommended as a complementary and adjunct modality to mammography in

breast cancer diagnosis, particularly for patients with dubious mammograms [13, 14]. Chapter 2 presents a review of the latest developments in this field, including commercially available breast-specific gamma cameras. The extent of the role of nuclear medicine in breast cancer imaging is dependent on further success in the development of these compact high-resolution dedicated cameras (as well as of breast-dedicated PET scanners).

1.3 Gamma cameras in nuclear medicine

The gamma camera has been one of the major developments in radionuclide imaging instrumentation and is today one of the primary imaging tools used in nuclear medicine, together with the PET scanner. It is considered the work-horse of practically every nuclear medicine department, performing all kinds of clinical studies. The fact that it remains such an important radiation detecting instrument, even though it was invented more than 50 years ago, demonstrates its robustness and versatility.

Despite many important advances of PET, single-photon imaging remains a very viable solution in nuclear medicine, as it is relatively less complex, less expensive and provides useful clinical information. Furthermore, improvements in the performance of gamma cameras are still expectable as research and development are ongoing, particularly in the field of small field-of-view (FOV) application-specific imagers, towards better spatial and energy resolutions, efficiency, uniformity and overall image quality, as well as hybrid solutions with additional anatomical information. As discussed above (1.2.2), one of the main target applications for new cameras has been scintimammography, where they can play an important role in breast cancer detection.

1.3.1 Radionuclides and radiopharmaceuticals for single photon imaging

Most gamma emitting radionuclides used in single photon emission imaging are originated from other radionuclides that decay through β emission or electron capture. These processes frequently leave the daughter isotope nucleus in an excited state, *i.e.* with an excess energy, which is then released in the form of a characteristic γ-photon, as schematised in Figure 1.3.

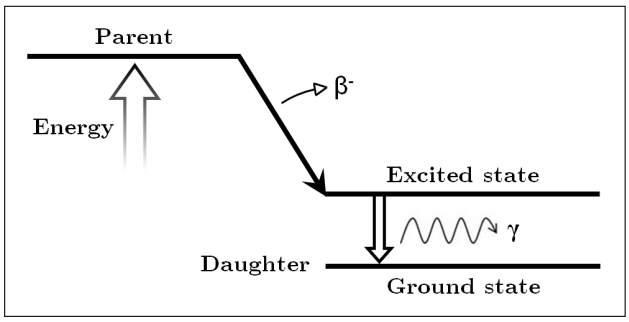

Figure 1.3: Emission of a γ-ray, following β^- decay.

Examples of these radionuclides are ^{123}I, ^{201}Tl or ^{133}Xe, but the most widely used is undoubtedly ^{99m}Tc, with around 30 million procedures performed each year [15]. It can be linked to many different pharmaceuticals and used as a tracer in a great variety of molecular imaging studies. Its parent radioisotope is ^{99}Mo, which decays mostly by β^- emission to ^{99m}Tc, with a half-life time of 65.95 hours [16] (equation 1.3). ^{99m}Tc then decays by isomeric transition to ^{99}Tc with a half-life time of 6.01 hours, emitting gamma photons with an energy of 140.51 keV (equation 1.4). These radiative properties make it particularly suitable for medical imaging: photons are energetic enough to escape the body without significant attenuation and to be detected efficiently and with good spatial resolution by conventional gamma cameras. Furthermore, ^{99m}Tc decay half-life time of 6 hours is long enough to complete diagnostic procedures with adequate concentrations remaining in the organ of interest but, at the same time, short enough to keep patient dose to a minimum.

$$^{99}_{42}\mathrm{Mo} \longrightarrow {}^{99m}_{43}\mathrm{Tc} + \beta^- + \overline{\nu} \tag{1.3}$$

$$^{99m}_{43}\mathrm{Tc} \longrightarrow {}^{99}_{43}\mathrm{Tc} + \gamma \tag{1.4}$$

^{99}Mo is traditionally produced in nuclear reactors by neutron activation of naturally occurring ^{98}Mo or as a product of uranium fission, the latter being preferred since it provides a much higher specific activity of ^{99}Mo (more than 500 times higher). After separation of ^{99}Mo from irradiated targets and purification, it is loaded into ^{99}Mo/^{99m}Tc generators, which are then delivered to nuclear medicine centres where they are used in clinical practice, usually lasting for about a week. The generator is composed of a plastic or glass column, filled with a material on which the parent radionuclide is adsorbed, alumina (Al_2O_3) in the case of ^{99}Mo. ^{99m}Tc is then eluted using a saline solution and obtained in the form of ($Na^{99m}TcO_4$). About 80% of the total ^{99m}Tc activity is eluted and after about 4 half-lives it returns to its maximum [17], which means the elution can be done efficiently on a daily basis.

^{99}Mo and ^{99m}Tc have been supplied to the medical community through these methods for many years now, inclusively coping with the growing demand from the market. However, in the last years, the ageing and shut-down (in some cases unanticipated) of nuclear reactors have caused supply shortages all over the world and lead to a re-thinking and exploration of alternative reliable methods of ^{99}Mo production, involving both nuclear reactors and accelerator techniques [15]. Even though the supply has been re-established, this is still a subject of ongoing debate and research, due to the fragile stability of the worldwide ^{99}Mo supply chain, which is dependent on only a few nuclear reactors.

The most used radiopharmaceuticals in breast-specific gamma imaging (BSGI) are ^{99m}Tc-sestamibi (^{99m}Tc-methoxyisobutylisonitrile) and ^{99m}Tc-tetrofosmin. Even though introduced as tracers for myocardial perfusion studies, they have shown high sensitivity and specificity in the detection of malignant breast tumours. Normally injected dose in scintimammography is 20-30 mCi (740-1110 MBq) [18, 19].

1.3.2 Typical components of a gamma camera

The conventional gamma camera is also known as scintillation camera, or Anger camera, in honour to Hal Anger, the American scientist who introduced it in 1958 [20]. Anger design still remains widely used today and is the basis of the majority of gamma cameras used, especially of large FOV imagers. Its major components are depicted in Figure 1.4.

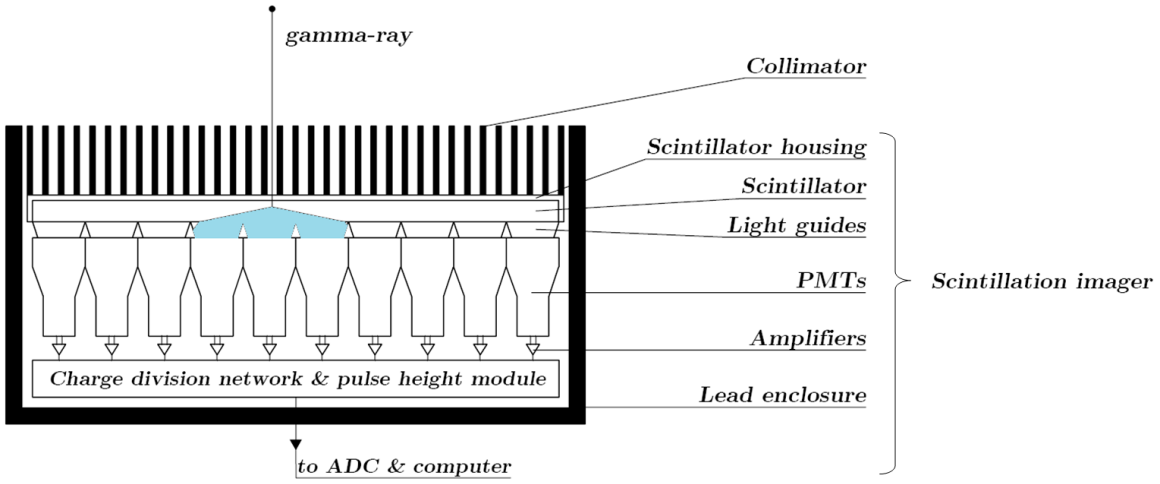

Figure 1.4: Schematic representation of the cross-sectional view of an Anger camera.

The detection medium consists of a large slab of a scintillator crystal (typically NaI(Tl)) with 25-50 cm diameter and about 1 cm thick. This thickness of NaI(Tl) provides an absorption efficiency of about 95% for 140 keV γ-rays. On one side of the crystal (the object's side), a collimator is placed, which is typically made of perforated lead, with holes arranged in a geometric pattern. The collimator is an indispensable part of every gamma camera since no meaningful image could be obtained without it. It defines the angle of incidence of the γ-rays, by accepting only the photons which are aligned with the holes and stopping the others, *i.e.*, it allows acquiring the desired projection of the object in the crystal. The other side of the scintillator crystal is coupled to an array of photomultiplier tubes (PMTs). The light generated by each γ-ray interaction in the crystal is distributed over several PMTs and the 2D position of each event is estimated from the relative size of their signals. The largest signal is usually from the PMT which is nearest to the position of interaction, with smaller pulses from PMTs at a larger distance. The centroid of the light distribution is then interpolated from all the signals using a charge division network (of resistors or capacitors) in which a part of each signal is coupled to X and Y output lines. The resulting X and Y position analogue signals are then connected to fast analog-to-digital converters (ADC) and to a computer, where signals are processed and used to produce an image. The sum of all PMT signals provides the energy signal, which is proportional to the energy of the incident γ-rays. This signal is passed through a pulse-height module, which consists of a single-channel analyser (SCA) that selectively accepts only those events whose energy falls within an en-

ergy window around the full gamma absorption energy. This allows eliminating lower energy events that result mostly from γ-rays that have scattered in the patient or elsewhere before reaching the crystal, and also higher energy spurious events that may result for instance from cosmic γ-rays interacting in the crystal. Both lower and higher energy events provide a false position indication, so this selection improves imaging performance. To minimise background radiation from other sources outside the FOV, the entire camera is enclosed on all sides by a lead shield, about 2-3 mm thick. As a result of the need for collimation and shielding, lead contributes significantly to the overall weight of a gamma camera.

In the following subsections, a more detailed description of the individual components of the Anger camera is presented.

Collimator

Gamma photons are too energetic to be focused like visible light and, because they are not charged particles, they cannot be deflected using electric or magnetic fields either. However, they can be attenuated and this is the principle of the collimator. In order to absorb γ-rays, a high-density material with a high atomic number is required. Lead (ρ=11.34 g.cm^{-3}, Z=82) is the usual choice, due to its cost and availability, but tungsten (ρ=19.25 g.cm^{-3}, Z=74) is also used. The collimator consists of holes perforated in the material, that define a narrow solid angle of acceptance through which γ-rays can pass without being attenuated or absorbed, thus producing a planar projection of the object being imaged. Depending on the geometrical characteristics of the collimator, the overall performance of the gamma camera will vary significantly, particularly in terms of spatial resolution, field-of-view and sensitivity, determining the quality of the images created and the time necessary to obtain them.

There are four basic types of collimators:

- **Parallel-hole** - holes are all aligned perpendicularly to the crystal plane and therefore, FOV size is not affected by the object-to-collimator distance.
- **Converging** - holes are closer together on the object side than on the crystal side, hence focused toward the organ. They produce a magnified image of a smaller FOV and thus are used to image small objects, providing higher efficiency and better resolution than parallel-hole collimators. Main applications are in pediatric and cardiac imaging.
- **Diverging** - reversed version of the converging collimator, *i.e.*, with holes farther apart on the object side. This produces a minified image of the object, which can be larger than the crystal size. Resolution and efficiency are lower than with parallel-collimator.
- **Pin-hole** - a small aperture in lead, which produces an inverted image with variable magnification depending on the source-to-collimator distance (SCD). The pin-hole collimator is used to image small organs such as the thyroid or the hip joint, providing better spatial resolution but lower efficiency.

Other types are slant-hole collimators, in which the holes are parallel but slanted with respect to the crystal plane, and fan-beam collimators, particularly used in SPECT.

The parallel-hole collimator is the most widely used type, inclusively in the gamma cameras developed in this work. For this reason, a parallel-hole collimator is assumed in all the following discussions, unless otherwise mentioned. The dimension of the holes, together with the thickness of the septa, determine the two most important characteristics of the collimator: resolution and efficiency. The spatial resolution R_c is defined as the full width at half maximum (FWHM) of the profile of radiation at the plane of the crystal, for γ-rays emitted by a point source in air that pass through the collimator into the crystal. This situation is sketched in Figure 1.5. From triangle similarity,

$$\frac{d}{L} = \frac{R_c}{L + x + c}, \tag{1.5}$$

where L, x and d are defined in the figure and c is the distance between the back face of the collimator and the mid-plane of the scintillator crystal. The effective length L_e of the holes corrects L for septal penetration that occurs near the ends of the septa, through

$$L_e = L - \frac{2}{\mu}, \tag{1.6}$$

where μ is the linear attenuation coefficient of the collimator's material for the given gamma energy. From equations 1.5 and 1.6, one obtains a good approximation for the resolution:

$$R_c \approx \frac{d(L_e + x + c)}{L_e}, \tag{1.7}$$

where a higher value of R_c means a worse spatial resolution.

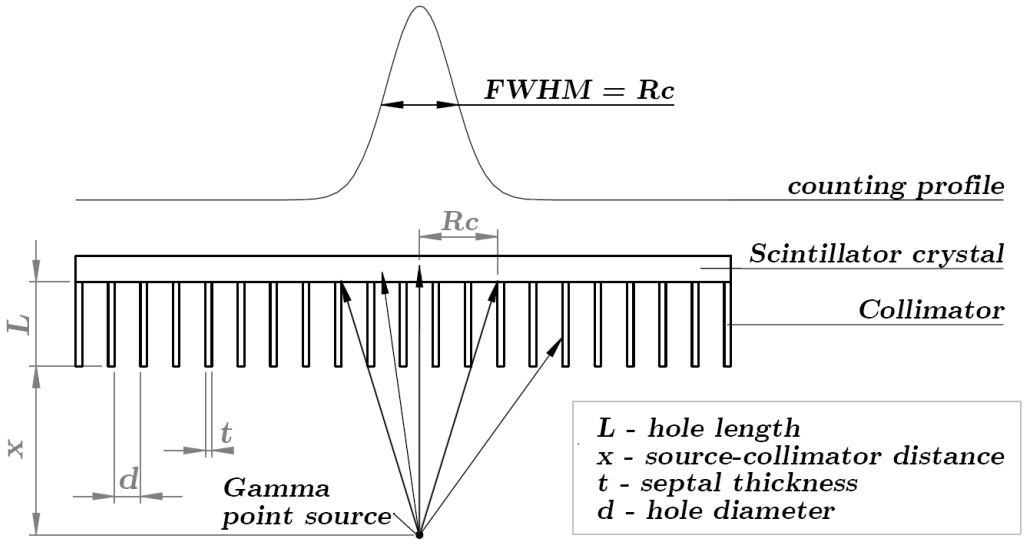

Figure 1.5: Parallel-hole collimator resolution geometry.

The geometric efficiency g is the fraction of the emitted gamma-rays that pass through the collimator and, assuming a point source and circular holes, it is approximated by [21]:

$$g \approx \left[\frac{Kd^2}{2L_e(d+t)}\right]^2, \tag{1.8}$$

where K is a correction factor for the hole shape, usually circular, hexagonal or square. The value for K and the exact equation differs for each specific shape. Typical g values for energies below 150 keV are between 0.02 and 0.06% (the majority of emitted photons is wasted).

Collimator's dimensions range from 1.5 to 3.5 mm for hole diameter (d), 1.5 to more than 3 cm for collimator length (L) and 0.15 to 1.5 mm for septal thickness (t). The choice is highly dependent on the γ-ray energy and on the requirements for resolution and efficiency. For this reason, most gamma cameras are provided with a selection of parallel-hole collimators, which are changed according to the radionuclide that is being imaged or to the desired resolution/efficiency levels. As can be inferred from equations 1.7 and 1.8, there is an inherent trade-off between spatial resolution and efficiency (sensitivity) of collimators, *e.g.* reducing the size of the holes or lengthening the collimator improves spatial resolution, but reduces efficiency.

The collimator resolution depends strongly on the source-collimator distance, deteriorating by about a factor of 2 for a distance of 4 to 5 cm, when comparing to a 0 cm distance. It is usual to quote the resolution of a parallel-hole collimator for a source 10 cm away, with typical values of 7.5 to 13 mm FWHM for energies below 150 keV. Therefore, to improve resolution and take full advantage of the performance of the camera as a whole, the source-to-collimator distance should clearly be minimised. A collimator resolution of less than 3.5 mm is attainable for distances under 3 cm, using high or ultra-high resolution parallel-hole collimators, obtaining a resolution of approximately the hole diameter for sources at the face of the collimator.

Scintillator crystal

The scintillator crystal is responsible for the conversion of γ-rays into visible light. Inorganic scintillator crystals are most often used in gamma cameras, because they have a high stopping power for γ-rays and high light yield, are relatively fast, have emission spectra well matched to the absorption spectra of PMTs and other photodetectors, and are relatively inexpensive to manufacture. The mechanism of light production in inorganic scintillation crystals is based on their electronic band structure, which dictates the allowed electron energy states in the lattice. When a γ-ray interacts in a pure inorganic crystal, electrons are transferred from the valence band into the conduction band and, after some time they recombine with holes, with the resulting excitation energy converted into light, emitted isotropically. For pure crystals, this process is rather inefficient and the light emitted is below the visible range,

Table 1.1: Properties of some inorganic scintillator crystals and their gamma response.

Crystal	λ_{max} (nm)	Density (g/cm^3)	Refract. index	Decay time (ns)	Light yield (ph/keV)	Comment
NaI(Tl)	415	3.67	1.85	230	38-45	Hygroscopic
CsI(Na)	420	4.51	1.84	630 [a]	38-49	Hygroscopic
CsI(Tl)	550	4.51	1.80	1000 [a]	54-65	Slightly hygrosc.
$LaBr_3$(Ce) [b]	358-380	5.1	1.9-2.4	16-35	61-76	Highly hygrosc.
YAP	350	5.35	1.93	30	16-22	
YSO	420	4.45	1.80	70	24	
BGO	480	7.13	2.15	300	8-9	Early use in PET
LSO	420	7.4	1.82	47	25-33	^{176}Lu activity
LYSO	420	7.1	1.81	40-41	27-34	^{176}Lu activity

[a] average decay time [b] properties vary with % of Ce^{3+} References: [24–29]

which is not useful for a standard PMT. However, by adding a small amount of a suitable activator impurity, electron energy levels are effectively produced in the previously forbidden bands, and the excitation energy is transferred to these levels, which then de-excite with emission of photons of a longer wavelength, within the visible range. Table 1.1 presents important properties of some of the most used inorganic scintillation crystals, including three with application in PET (at the bottom). Some scintillators such as NaI(Tl), the standard scintillator of the Anger camera, are highly hygroscopic, so they need encapsulation to prevent damage from moisture, usually inside an aluminium can with a transparent glass window.

Of the tiny fraction of emitted γ-rays that pass through the collimator holes and reach the crystal, some are absorbed in the crystal, some are scattered and some pass through it without interaction. The relative probabilities of these events depend on the photon energy and on the crystal thickness. A thicker crystal improves detection efficiency but, on the other hand, it worsens the intrinsic spatial resolution, R_i (resolution without the collimator). Considering that most studies are performed with ^{99m}Tc, a thickness of NaI(Tl) between 9 and 13 mm is common, absorbing over 90% of the 140 keV γ-rays [22, 23]. Since a thinner crystal provides a better R_i (further detailed in 1.3.3), in some cases 6 mm thick crystals are used, which is still considerate acceptable, with about 80% efficiency for 140 keV.

Photomultiplier tubes

Scintillation photons are detected in the Anger camera by an array of PMTs, which convert them to measurable electric signals, allowing the determination of both position and energy of the original γ-ray. Each PMT is a vacuum-sealed tube usually made of glass, with a photoemissive cathode, a system of several dynodes (6-14) which provide a gain mechanism

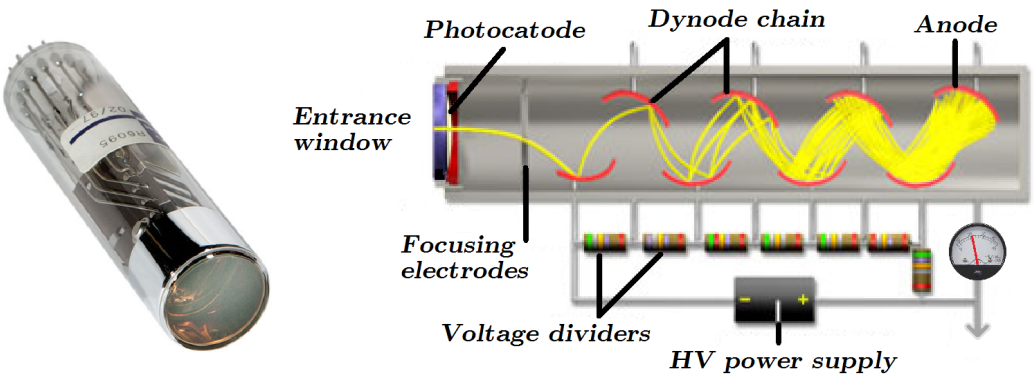

Figure 1.6: Photograph and schematics of a PMT (adapted from [30]).

by electron multiplication and a charge collecting anode which outputs the current signal (Figure 1.6). The photocathode is formed by deposition of a photosensitive material on the inner surface of the light entrance window, usually a compound semiconductor with a low work function. The properties of the photocathode determine its quantum efficiency (QE), defined as

$$QE = \frac{number\ of\ emitted\ photoelectrons}{number\ of\ incident\ photons}. \tag{1.9}$$

The QE of a photocathode varies strongly with the wavelength of the incident light and composition material. Photocatode materials which provide the best QE for the scintillation light of NaI(Tl) are based on K_2CsSb (bialkali), typically achieving a QE of about 25% at 415 nm, meaning that 1 in each 4 scintillation photons that hit the photocathode is converted into a primary photoelectron. Recent developments of the so-called super and ultra bialkali photocathodes report enhanced QEs of up to about 38% for the same wavelength [31].

After being ejected from the photocathode into the internal vacuum of the PMT, the low-energy electrons are accelerated by an appropriate electric field which focuses them toward the first dynode, held at a positive potential. The deposition of kinetic energy in the dynode causes the release of secondary electrons, which are again accelerated and multiplied in the following dynodes, held at increasingly higher potentials. A typical high voltage of 1000-1500V is applied in the PMTs of gamma cameras, with about 100-150V increments between dynodes. The resulting gain is in the order of 10^6-10^7.

Many PMTs are used in the Anger camera, packed closely together and coupled to a large monolithic scintillator. The light output from the scintillator spreads over several PMTs (as depicted in Figure 1.4) and the relative amounts of charge collected at each PMT anode provide the information needed to estimate the position of interaction of the γ-rays in the crystal. PMTs are available in a wide variety of sizes and forms, most commonly with circular or hexagonal entrance windows and a diameter around 3-7 cm. An Anger camera can have about 20 to 100 PMTs, for a typical field-of-view of 40×40 cm^2. The use of smaller diameter

PMTs improves the spatial resolution, but at the expense of a higher cost.

The scintillator crystal can be coupled through light guides to the active areas of the PMTs, in order to optimise light collection. Furthermore, all components are coupled together with optical grease, to minimise refractive index differences and therefore light losses at the interfaces.

Signal readout, processing and image reconstruction

The output signal of each PMT is connected to its own preamplifier, used mainly to match the tube impedance to that of the following electronics. In addition, and in conjunction with high voltage adjustments, preamplifiers allow tuning the PMT signals so that their amplitude is identical for the same amount of energy absorbed in corresponding regions of the camera.

As mentioned above (1.3.2), the electronics used for position estimation from all the PMT signals consist in most times of a charge division network of resistors or capacitors to which all the PMT signals are connected, known as Anger logic. The signal from each preamplifier is connected in parallel to several resistors or capacitors, with precise values that reflect the position of the corresponding PMT in the matrix. In this way, the network can provide an estimation for the position of each event with only 4 output signals, x^+, x^-, y^+ and y^-, each resulting from the sum of the weighted signals of all the PMTs. The simplified example of a resistor network for an array of 7 PMTs is illustrated in Figure 1.7.

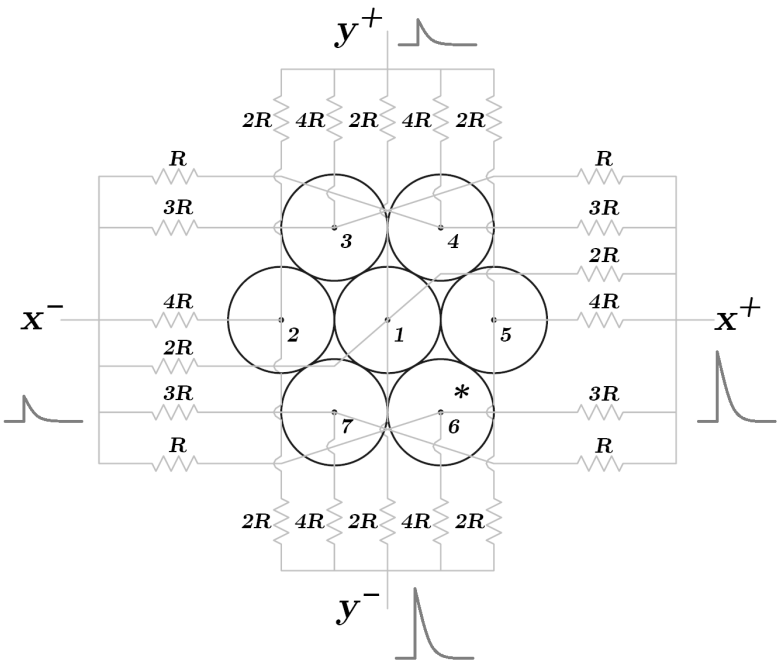

Figure 1.7: Anger's position-encoding resistor network: resistor values are weighted by a factor dependent on the position of the PMT. Output signals are exemplified for a γ-ray interaction occurring at a location ($*$) near tube 6.

The difference between the two values in each direction is proportional to the position:

$$X = \frac{k}{Z}(x^+ - x^-) \quad ; \quad Y = \frac{k}{Z}(y^+ - y^-), \tag{1.10}$$

where k is a constant and k/Z is the amplifier gain. Z is the energy signal of the event, given by the sum of all 4 signals:

$$Z = x^+ + x^- + y^+ + y^-, \tag{1.11}$$

which is proportional to the total energy deposited by the γ-photon.

This energy signal is then analysed in a pulse-height module, whose function is to ensure that only photons within a specific energy window (or windows) are included in the image. For instance, in a ^{99m}Tc imaging study, a 20% window (or $\pm$10%) around the 140 keV photopeak may be defined, which means that the range of accepted energies will be 126-154 keV and all the other events will be discarded. This allows rejecting γ-rays that reach the scintillation crystal after suffering Compton scattering inside the body or elsewhere, as well as any characteristic X-rays created within the detector or collimator material, that would otherwise add random noise to the image.

In earlier cameras, signals were obtained in analogue form, projected on cathode-ray tube monitors and recorded with magnetic tapes or laser disks. The development of electronics and analog-to-digital converters (ADCs) allowed the storage of data in digital format for later processing and, in modern cameras, the digitisation of each PMT output by an ADC even before pulse-height and positioning analyses take place.

In a typical gamma camera imaging study, data is acquired for a preset number of events or time duration (*e.g.* 500.000 events or 10 minutes). The image produced is represented on a grid of pixels, with the value assigned to each pixel being the number of events detected within that pixel's area. The image is therefore a 2D histogram of the spatial distribution of all valid events.

1.3.3 Performance parameters of a gamma camera

The quality of the images provided by a gamma camera is affected by several performance parameters of the system, such as spatial and energy resolution, sensitivity and uniformity, which are described in detail in the following subsections.

Spatial resolution

The spatial resolution R is a measure of the ability of a gamma camera to correctly reproduce the distribution of a non-uniform radioactive source. It can be empirically defined as the minimum distance between two point sources that can be distinguished in the image or, more formally, as the full width at half maximum (FWHM) of the distribution of centroids

for a point source of γ-rays in the air at a given distance of the collimator (usually quoted at 10 cm). Since the spatial resolution of the gamma camera is highly dependent on the collimator, it is expressed as the result of separate contributions from the collimator and the rest of the camera, also called the scintillation imager. This includes the scintillator, light guides, photodetectors and instrumentation for signal acquisition and processing (Figure 1.4). The system resolution (also called extrinsic resolution) can then be expressed as

$$R = \sqrt{R_c^2 + R_i^2}, \tag{1.12}$$

where R_c is the collimator resolution and R_i the intrinsic resolution of the scintillation imager. A lower numerical value of R means a better (higher) spatial resolution.

Being limited by R_c, R depends also strongly on the source-to-collimator distance (SCD). As mentioned above, R_c can be less than 3.5 mm FWHM for short distances under 3 cm, but for larger distances it increases significantly and so becomes the dominant factor, deteriorating the image resolution even if the value of R_i is very low. In modern Anger cameras, R_i is in the order of 3-4 mm FWHM [21, 32, 33]. Considering a short SCD, an improvement in R_i can then result in a significant improvement of R. This may be achieved by two ways:

- a brighter and thinner scintillator crystal - more photons are emitted per event and there is a lower spread of the light. In a thinner scintillator there is also less probability of Compton scattering followed by photoelectric absorption;
- a more efficient photodetector - more photoelectrons are generated.

Energy resolution

As the spatial resolution measures the ability of a gamma camera to distinguish closely located objects, energy resolution measures its ability to distinguish γ-rays with close energies. This is important for the pulse-height module to be able to correctly identify the full-absorption events resulting from unscattered γ-photons, which are relevant for radioisotope imaging, and reject the lower energy γ-rays which do not contain information about the original location of gamma emission. The energy resolution R_{en} is quantified as a percentage, by measuring the width of the photopeak relative to its energy E_γ:

$$R_{en} = \frac{FWHM}{E_\gamma} \times 100\ (\%). \tag{1.13}$$

The lower the percentage, the better the energy resolution and the narrower the window that can be defined around the photopeak.

Energy resolution is determined by the degree of fluctuation of the PMT outputs, which is mostly dependent on the statistical variations in the number of photoelectrons created at

the photocathode and multiplied at the dynodes during the avalanche development, and also on the statistical fluctuations of the light emission process in the scintillator. Higher energy γ-rays create more scintillation photons and thus more photoelectrons, so energy resolution is better for higher energies. Gamma cameras are designed for optimal detection of γ-ray energies in the 100-200 keV range. The energy resolution of NaI(Tl)-PMT array scintillation imagers in modern Anger cameras is about 9-10% FWHM for 140 keV.

Sensitivity

The sensitivity of a gamma camera is directly related to its detection efficiency and counting rate capability, being usually measured as counts per minute per μCi. The detection efficiency measures the ability to convert gamma emissions into useful signals. It is simply given by the ratio of detected events per emitted γ-rays, hence mostly determined by the collimator, which has an efficiency between 0.02 and 0.06%. As for the scintillation imager, its efficiency E depends mainly on the thickness (x) of the scintillator and on the energy of the γ-rays, according to the formula [21]

$$E \approx 1 - e^{\mu_l x}, \tag{1.14}$$

where μ_l is the linear attenuation coefficient for the crystal, at a given energy. A minimum value of 80% scintillator detection efficiency is commonly used in Anger cameras, but lower values may be acceptable to favour a higher spatial resolution. In clinical practice, different collimators are used and changed to deal with the inherent trade-off between sensitivity and spatial resolution of a gamma camera and its variation with radionuclide energy. A higher sensitivity results in a higher count rate and thus better image statistics in less acquisition time, which in practice may even result in images with better quality than those obtained with a collimator of very good resolution but poor efficiency. However, too high count rates ($>$ 150.000 cps) may result in a decreased sensitivity and degrade also other gamma camera parameters, due to dead time, pulse pileup and baseline shift issues. Fortunately, such high count rates are rarely occurring in single-photon nuclear medicine.

Until not a long time ago, gamma cameras could only process the signals from one gamma interaction at a time, due to finite scintillation rise and decay times and corresponding requirements of the detector electronics. It was not possible to detect interactions which resulted in an overlap of scintillation and signal processing. This effect produces a dead time typically in the order of μs and limits the counting rate capability. About a decade ago, manufacturers developed gamma cameras that can electronically segment the FOV, so that they are able to identify the few PMTs which receive most of the light and release the others for detection of new events while the signals from the first event are being processed. This advance has had some impact on single-photon emission imaging, but was developed mostly so that gamma cameras could be used to perform positron emission tomography [34, 35].

Uniformity

Uniformity is a measure of the camera's response to a uniform irradiation of the detector's surface. It is directly related to position linearity, which evaluates the camera's ability to accurately reproduce the spatial distribution of a radionuclide. Intrinsic uniformity (without the collimator) can be measured using a point source placed at a distance of 4 to 5 times the width of the crystal, while extrinsic measurements are usually performed with a flood source (an extremely uniform planar source).

Ideally, the response to a uniform irradiation would be a perfectly uniform image, but uniformity can be significantly degraded by position non-linearities. Because of the dead regions originated when coupling several PMTs, there is a systematic mispositioning of events that result from γ-interactions in regions corresponding to the edges or in between PMTs, shifting their positions toward the centre of the nearest PMT. This results in a non-uniform flood image and non-linearity of straight-line objects, as illustrated in Figure 1.8. Another important factor contributing to non-uniformity is the variation of the magnitude of the energy signal Z with the position of interaction in the scintillator crystal.

If no uniformity correction is applied, the difference between the count density in two points of an image acquired from a flood source can be as high as 30%. In purely analogue camera designs, uniformity correction is accomplished by a clever light-guide design and by tuning the PMT gains, but such designs are limited. The signal digitisation in modern gamma cameras allows not only digital image processing and storage, but also the incorporation of calibration data and software algorithms to correct for spatial non-linearities and pulse-height variations. Uniformity correction factors are determined for each pixel in the clinical image after acquisition of a very high-count flood image.

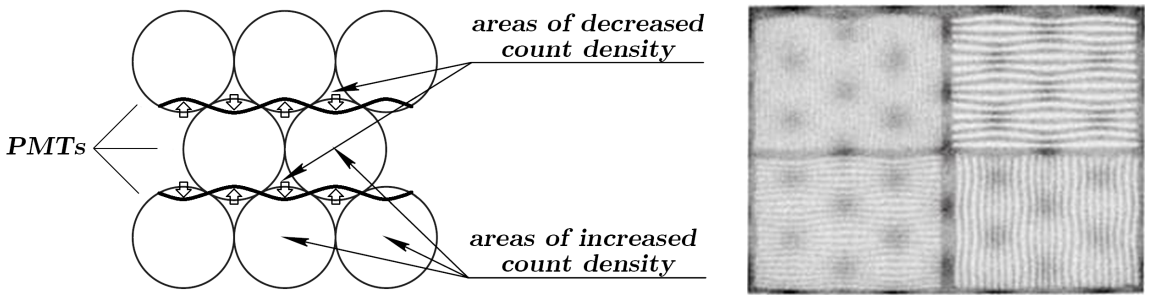

Figure 1.8: Non-uniformity in a gamma camera. Left: schematic representation of the natural shift of events due to non-uniform PMT response. Right: Image of a bar phantom without corrections for non-uniformity (adapted from [21]).

Field-of-view

The FOV of a gamma camera is the size of the imaged area on the object plane and it depends on the type of collimator used. For parallel-hole collimators, there is a 1:1 relationship between the camera effective detection area and the FOV, whereas other types of collimators may provide a larger or smaller FOV (*e.g.* converging collimators magnify the object, therefore the FOV is smaller than the camera's effective area).

The useful FOV is defined as the part of the geometrical FOV where there are no ambiguities on the position determination. Most Anger cameras have a FOV of about 40×40 cm^2 (or diameter of 40 cm), determined by the size of the scintillation crystal and array of PMTs. However, the useful FOV of a typical gamma camera is smaller than the actual detector size, because of the dead area around the edges. This dead area results from the need to mask an undesired outer ring of increased intensity that is generated in the image, a phenomenon known as *edge packing*. *Edge packing* is caused by internal reflection of scintillation photons in the crystal's lateral surface and border with the aluminium housing. The reflected photons are then detected by the outer-edge PMTs, resulting in an asymmetrical charge distribution and distortion in the centroid calculation, causing the brighter ring in the image. This effect is masked by using a lead ring around the edge of the collimator, or by electronically excluding the use of the outer PMTs for events occurring in the edges. Therefore, the dead area around the edges has the width of the lead ring (about 5 cm) or the size of one PMT diameter, normally between 3 and 7 cm.

1.3.4 Requirements of a gamma camera for scintimammography

Breast imaging using a conventional gamma camera has several limitations, mainly due to its bulkiness which makes it difficult to obtain the optimum projection. The best images can be obtained with the patient lying in prone position on an imaging table with cut-outs for the breasts, positioning the camera laterally and as close to the breast as possible, so as to avoid background emission from other organs with high ^{99m}Tc-sestamibi uptake, particularly the liver and myocardium. However, with this positioning, the camera face is still a few centimetres away from the breast tissue, resulting in a degradation of the spatial resolution and consequently in the inability to detect small tumours. Furthermore, the dead area around the edges in standard gamma cameras (mentioned in the previous section) results in the masking of several centimetres of breast tissue closest to the chest wall, when trying to acquire views equivalent to X-ray mammography with a standard gamma camera. Consequently, the detection of tumours deeper inside the breast is also impaired.

A dedicated small FOV gamma camera can have a thinner shielding and reduced dead regions around the edges, enabling the visualisation of a greater area of breast tissue. A FOV size of about 12×12 cm^2 is considered appropriate for breast imaging, with an ideal dead space

at the edges of less than 5 mm. Hence, a compact camera head makes it possible to put the detector face in direct contact with the breast tissue and acquire images in a similar format to that used in X-ray mammography, allowing for an easier comparison. More importantly, the reduction of the distance between the breast and the active area of detection improves the camera's spatial resolution, a crucial parameter to improve in scintimammography in order to detect small tumours under 1 cm diameter, for which the sensitivity with a standard gamma camera and prone positioning is low [36]. Breast-detector distance reduction can be further optimised by applying breast compression.

Since the size of the primary lesion is directly correlated with the likelihood of cancer spreading, it is of critical importance to detect small lesions at an early stage of disease. Screening X-ray mammography can routinely detect lesions with 5 mm or less, therefore scintimammography should ideally be able to find lesions of this size range. To accomplish this, not only the better positioning of the camera is required, but also the intrinsic spatial resolution of the scintillator imager (R_i) needs improvement. As previously mentioned, R_i of modern Anger cameras is 3-4 mm FWHM, hence the usual requirement for dedicated breast imagers is $R_i < 2$ mm FWHM.

Energy resolution R_{en} of a compact gamma camera based on scintillation detection should be able to match that of Anger cameras, *i.e.* 9-10% FWHM at 140 keV. Since a better positioning improves the rejection of Compton scattered photons from other organs, a compact gamma camera with the same R_{en} will provide better imaging results. However, as shown by Hruska *et al.* [37, 38], the inverse is not observed, *i.e.* for the same positioning conditions that guarantee a low scatter content of breast images, changes in R_{en} between 3-20% do not have a significant impact on tumour detectability. Therefore, even though a low value of R_{en} is desirable, values up to 20% may be acceptable.

As for detection efficiency, the same considerations made in 1.3.3 apply to a small FOV gamma camera for scintimammography.

1.4 The wavelength-shifting fibre gamma camera

The wavelength-shifting fibre (WSF) gamma camera is an alternative to the Anger camera and the basis for the work presented in this thesis. Its design was firstly developed by Soares *et al.* around 2000 [39], following the concept introduced by Worstell *et al.* for the development of a high-resolution PET detector [40]. It consists of two perpendicular ribbons of WSFs covering both faces of a scintillator crystal, such that the fibres positioned on one face provide the x coordinate and the ones on the other face the y coordinate of the gamma photon interaction point (Figure 1.9). The fibres absorb a great part of the scintillation light isotropically emitted from the crystal and re-emit it at a longer wavelength. One end of each WSF is then read out by a highly sensitive photodetector, with the resulting signals

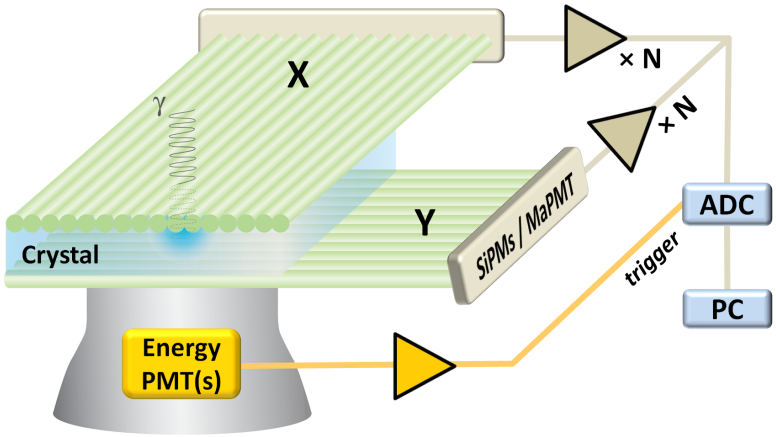

Figure 1.9: Schematics of the wavelength-shifting fibre gamma camera design.

being used to estimate the 2D position. The other end is mirrored to reflect as much as possible the light that was initially trapped in the opposite direction. The energy signal is provided by PMTs that cover the full detector area on one side. These are indispensable because most of the scintillation light is not trapped in the fibres and therefore the signals from the photodetectors reading out the fibres are not sufficient to provide an acceptable energy resolution. The signal from these PMTs, besides allowing the definition of an energy window for imaging, is also used to generate a trigger for signal digitisation by the ADC.

This concept has the advantage of using N+N instead of N×N photodetectors to cover an identical imaging area, and allows building a compact detection head with a flexible design, able to fulfil the requirements mentioned above for a breast-dedicated gamma camera. Another potential application is in small animal imaging.

1.4.1 Photon detection components

In this section, the individual components that make up the WSF gamma camera are described in more detail and considerations are made about their interdependent properties.

Wavelength-shifting fibres

WSFs are plastic optical fibres with a fluorescent organic additive embedded in the core material, which absorbs photons of a specific wavelength range and re-radiates the energy at a longer wavelength. A good separation between the optical absorption and emission spectra of the fluor is desirable, to minimise self-absorption. Most commonly, the fluor absorbs strongly in the blue region of the spectrum and re-emits in the green. Wavelength-shifters have since long been used in nuclear and high-energy physics experiments [41–43], for light collection from large scintillators or in complex geometries and experimental conditions where direct photodetection may not be appropriate. Furthermore, they have found application in

other nuclear medicine instrumentation concepts, particularly in PET [44, 45].

Like in any other optical fibre, the core of a WSF is surrounded by a thin layer of cladding material with a lower index of refraction, so that photons arriving at the core-cladding interface with an adequate angle of incidence are "piped" along the fibre by total internal reflection. A second cladding with an even lower index of refraction is often used to increase the amount of light retained and also protect the fibre from damage.

There are 3 essential parts to the light guiding function performed by a wavelength-shifting fibre: 1) absorption, 2) re-emission and 3) transmission along its length (Figure 1.10).

The percentage of absorbed photons depends mainly on the wavelength of the incident light but also on the geometry of the WSF. For the wavelength of maximum absorption, over 80% of the light is absorbed in a length of one diameter [46]. If the fibres are round, the optical path in each fibre will be shorter than a diameter for many scintillation photons (the ones that do not cross the fibre axis) and therefore, square fibres provide a more efficient absorption, as well as a better coupling to a flat scintillator crystal.

An important property related to re-emission is the quantum efficiency of the WSFs (QE_{WSF}), defined as the probability of emission of a wavelength-shifted photon per absorbed photon. QE_{WSF} depends of the fluor used and is usually 70-80% [47]. The re-emission of light by the WSF core material is isotropic and therefore bears no relation to the direction of the absorbed light. This is an advantage in the case of the WSF gamma camera, because it allows trapping scintillation photons in the fibres that otherwise would be lost because of an inadequate angle of incidence in the WSFs, whose cross-sections are perpendicular to the scintillator faces.

The efficient transmission of the re-emitted photons, from their point of origin until the fibre end, depends on the trapping efficiency of the fibres, *i.e.* the fraction of re-emitted photons that is trapped inside the WSFs, and on the light attenuation length, usually defined as the distance at which the light intensity in the fibre is reduced to $1/e$ of its initial value. Trapping efficiency is determined by the refractive indices of the fibre core and cladding ma-

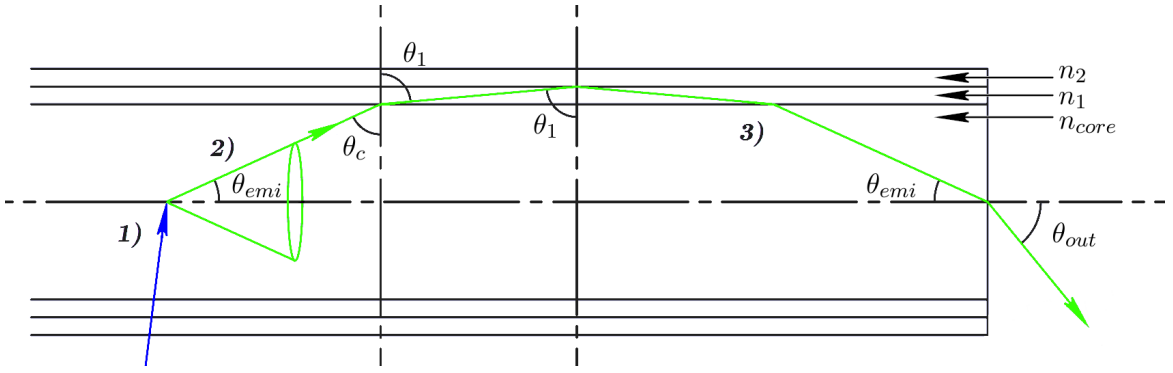

Figure 1.10: Optical path of a photon absorbed by a double-cladded WSF and re-emitted from the fibre axis with a maximum angle for total internal reflection θ_{emi}.

terials, since these define the maximum angle of emission below which total internal reflection occurs, according to Snell's law of refraction:

$$n \times \sin(\theta) = n' \times \sin(\theta'). \tag{1.15}$$

Applying it to a double-cladded fibre, one obtains for the two interfaces:

$$n_1 \times \sin(\theta_1) = n_2 \times \sin(90^\circ) \tag{1.16}$$

$$n_c \times \sin(\theta_c) = n_1 \times \sin(\theta_1) \tag{1.17}$$

The maximum angle of emission relatively to the fibre axis is then given by

$$\theta_{emi} = \arccos\left(\frac{n_2}{n_c}\right). \tag{1.18}$$

For the chosen WSF, Saint-Gobain Crystals BCF-91A, with a core of polystyrene and claddings of acrylic and fluor-acrylic ($n_c = 1.6$, $n_1 = 1.49$ and $n_2 = 1.42$), this angle is 27.4°, corresponding to a trapping efficiency of 5.6% per fibre end, for round fibres [48].

While $1/e$ attenuation length given by the manufacturer is > 3.5 m, independent measurements [49, 50] have reported values of about 2 m for this fibre. However, the assumption of a single attenuation length is not correct because attenuation is more significant for shorter distances (up to $0.5-1$ m) and therefore better described by a sum of two exponential decay components. For a fibre length of about 20 cm needed in a WSF gamma camera, a light loss of 15-20% is expectable. In this case, the total efficiency of the fibre, *i.e.* the percentage of incident photons which reach the fibre end, considering absorption, re-emission, trapping and attenuation, is of the order of 2-3% for CsI(Na) scintillation light.

Scintillator

In order to optimise the light absorption by the WSFs, the scintillator crystal must be chosen so that its emission spectrum matches the fibre's maximum absorption region. As mentioned in section 1.3.2, the best scintillator crystals for use in single photon gamma imaging, besides the traditional NaI(Tl), are CsI(Na), CsI(Tl) and, more recently, $LaBr_3$(Ce). Since most WSFs absorb in the blue region, CsI(Tl) is not an appropriate choice due to its long emission wavelength (in the green region). Similarly, $LaBr_3$(Ce), despite its very high light yield and excellent energy resolution [51], emits at shorter wavelengths, in the violet region of the spectrum. This crystal has a relatively high refractive index, which increases interface reflections and impairs the light transmission to the fibres. Furthermore, the very high hygroscopicity and low mechanical stability of $LaBr_3$(Ce) [52] compromise its durability and application in a WSF gamma camera. LSO or LYSO could be a good option but the

background radioactivity due to the presence of ^{176}Lu (γ emissions of 89, 202, 307 and 401 keV) makes them unsuitable for single photon imaging, where the typical count rate is about 10,000 cps. Intrinsic ^{176}Lu activity in LSO/LYSO crystals is approximately 240 cps/cm^3 [23].

Comparatively to NaI(Tl), CsI(Na) has very similar characteristics in terms of emission spectrum, light yield and refractive index, but has also properties that can be of advantage when used in a WSF gamma camera. Its higher density (4.51 compared to 3.67 g/cm^3) and effective atomic number (54.1 to 51) result in a higher conversion efficiency for γ-rays. This, in turn, allows obtaining the same detection efficiency with a thinner crystal, thus reducing the light spread over the fibres and therefore favouring a better spatial resolution. A 3 mm thickness of CsI(Na) absorbs about 70% of 140 keV γ-rays. In addition, CsI(Na) is less hygroscopic than NaI(Tl) and does not require special encapsulation. The main disadvantages are its relatively poorer energy resolution and slower decay time.

As can be seen in Figure 1.11, the light emission from CsI(Na) has a very good match to the fibre's absorption spectrum.

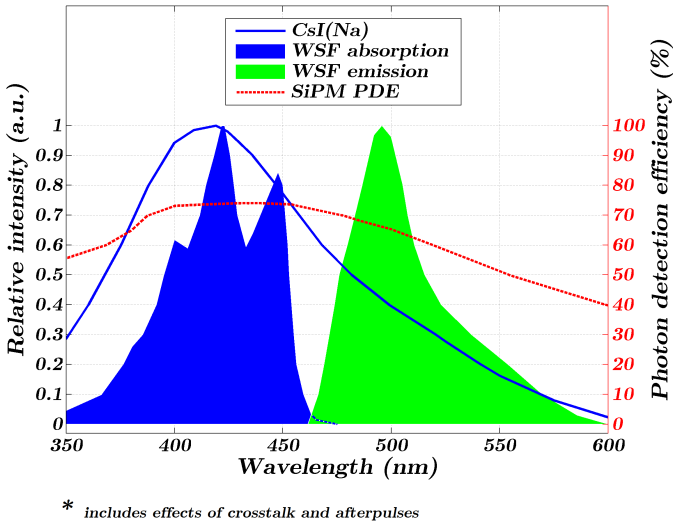

Figure 1.11: Optical spectra of CsI(Na) (emission) and BCF-91A wavelength-shifting fibre (absorption and re-emission), together with the plot of the PDE of a SiPM (Hamamatsu S10362-11-100U) as a function of wavelength, as given by manufacturers.

The choice between a continuous or a segmented scintillator crystal has an impact on the performance of a WSF gamma camera, particularly in terms of detection efficiency, spatial and energy resolution. As discussed above (in 1.3.2 and 1.3.3), the thickness of continuous crystals determines the trade-off between detection efficiency and spatial resolution. With segmented crystals, a higher thickness does not degrade spatial resolution, since the light is confined to one segment and transmitted only to the fibre(s) directly above and below that segment. Therefore, in principle, segmented crystals allow having a good spatial resolution while keeping a high detection efficiency. However, the thicker the crystal and the smaller

the cross-section of the segments, the higher is the number of internal reflections of the scintillation photons in the crystal's lateral boundaries and the lower is the number of photons that actually reach the ends of the crystal. This is a significant drawback because it can strongly degrade energy resolution, which is already diminished in the WSF gamma camera due to the presence of the fibres between the scintillator and energy PMTs. Therefore, a relatively thin continuous crystal is preferable in order to have good spatial and energy resolution, at the cost of a lower detection efficiency.

Photodetectors for fibre readout

For an efficient detection of the low light levels that reach the ends of the fibres in each scintillation event, highly sensitive photodetectors are required, with single photon detection capability. This is only achieved by devices with high internal gain and high signal-to-noise ratio (SNR). In addition, the photodetectors' quantum efficiency (QE) should be well matched to the fibres' emission spectrum, as high as possible at the wavelength of maximum emission (494 nm for BCF-91A), in order to maximise the number of photoelectrons created by the light pulses from the fibres and thus improve the spatial resolution of the WSF gamma camera. The devices that best fulfil these requirements and are most suited for individual readout of many fibres in a WSF gamma camera are multi-anode photomultiplier tubes (MaPMTs) and silicon photomultipliers (SiPMs), described in more detail in chapter 3.

1.4.2 Previous studies

Previous work has been done by Soares *et al.* in developing a WSF gamma camera, using a CsI(Na) scintillator, BCF-91A fibres and MaPMTs as photodetectors [39]. Solid angle calculations performed for a 3 mm thick crystal coupled with optical gel ($n = 1.5$) to 1 mm WSFs showed that the scintillation light spreads over a maximum of 5 fibres and that the majority of photons reaching the fibres hits the fibre directly above/below the gamma interaction point (about 60%) or the immediately next ones (30%). Even though the light level expected at the end of the fibres is very low, in the order of 10 to 15 photons for a 140 keV interaction (corresponding to about 2 to 3 photoelectrons produced in a photodetector with 20% QE at 494 nm), it has been shown that positioning is possible with an average of less than 1 photoelectron [53]. These studies used Hamamatsu R5900-M16 MaPMTs (with $\approx$ 12% QE at 500 nm), reporting an energy resolution of 23% FWHM at 122 keV and a spatial resolution of 3-4 mm FWHM, which is comparable to the intrinsic spatial resolution of the Anger camera. Moreover, Monte Carlo simulations predicted a significant improvement of this value by simply replacing the MaPMTs by higher QE devices, with a 4-fold increase in QE leading to a spatial resolution of less than 2.5 mm FWHM [46]. This fact, in conjunction with the introduction of the SiPMs, that became commercially available only in the last

decade, served as the main motivation for the work presented in this thesis, which explores the application of SiPMs in a WSF gamma camera.

SiPMs are compact and extremely sensitive solid-state photodetectors, with an effective photon detection efficiency of about 30-40% at 494 nm and therefore a great potential to improve the spatial resolution of the WSF gamma camera, at a comparable or even lower cost. Another advantage is their lower power consumption, comparatively to MaPMTs.

CHAPTER

2

STATE OF THE ART OF SMALL FIELD-OF-VIEW GAMMA CAMERAS

To overcome the limitations of conventional gamma cameras in nuclear medicine, particularly for imaging specific organs, different types of compact dedicated gamma cameras have been developed. Besides allowing a better positioning and mobility which may permit its use in other clinical environments such as surgery, the advantage of small FOV gamma cameras is that, because of their smaller detection area, they can be designed to have significantly better intrinsic spatial resolution than the conventional scintillation camera at a reasonable cost, *i.e.*, one can use a more extravagant high-performance detector technology that may not be cost-effective for a large FOV camera.

The most important research efforts towards small FOV imagers with higher spatial resolution have been carried out in the last two decades and ongoing developments continue in several groups, the majority of which aiming for application in BSGI. There are currently a few commercial breast-specific gamma cameras available in the market.

For most small FOV gamma camera applications, planar projection imaging is more typical than tomographic imaging, because very close proximity to the body is a primary motivation and, in the case of breast tumour detection, also because breast projection images similar to standard mammography views are desirable for a better comparison of clinical images. Furthermore, a small imager can be configured with a design compatible with standard mammography fixtures for breast compression and immobilisation, allowing the co-registration of anatomic and functional images, an additional aid in the diagnosis.

As mentioned in the first chapter (1.2.2), the clinical benefits of using a small FOV gamma camera with higher intrinsic spatial resolution and in close proximity to the organ of interest are very significant, having been clearly demonstrated by several studies. Scopinaro *et al.* [54] showed how the use of a breast-specific gamma camera with high intrinsic spatial resolution and breast compression, increased sensitivity for sub-cm tumours from 50 to 81% comparatively to Anger camera prone scintimammography, maintaining a specificity of 86%. Recently, Sun *et al.* [55] published a review and meta-analysis of 19 studies performed in the last decade on the effectiveness of BSGI, demonstrating its excellent performance as an adjunct modality to mammography. Despite different protocols used in these studies (*e.g.* different cameras or administered doses), pooled sensitivities for detecting sub-cm breast cancer and ductal carcinoma in situ (DCIS) were 84 and 88%, respectively, which is even higher than mammography in the latter case. Moreover, BSGI is advantageous in the identification of invasive lobular carcinoma, another type of breast cancer for which the sensitivity of mammography is inferior (79 versus 93%), according to Brem *et al.* [56].

All in all, high performance small FOV gamma imagers developed as a result of intense research efforts have lead to the creation and growth of a new clinical modality for breast imaging, BSGI, which has proved its usefulness as an adjunct to standard screening mammography in the detection of small non-palpable breast tumours, particularly in some types of cancer or in denser breasts, where mammography has lower sensitivity. BSGI can therefore

reduce the number of breast biopsies performed after a suspicious mammogram that reveal a benign tissue, which without further imaging is the majority of cases, amounting to as much as two-thirds of all biopsies [57]. Due to these proven benefits and other advantages relatively to alternative diagnostic methods such as MRI or ultrasound [56, 58], an increasing use of BSGI is expected in the future.

Early small FOV gamma cameras were basically miniaturised versions of the Anger design. A pioneer example is the camera developed by Milster *et al.* [59] in the University of Arizona, which divides a large FOV into small modules based on a 10×10 cm^2 NaI(Tl) crystal, a light guide and four square PMTs, improving the performance in terms of sensitivity, energy and spatial resolution, comparatively to the larger Anger camera.

The technologies that have been used as alternatives to this traditional NaI(Tl)-PMT technology can be divided in three main groups:

1. Scintillators coupled to multi-anode photomultiplier tubes (MaPMTs);
2. Scintillators coupled to arrays of solid-state photodetectors (*e.g.* SDDs, SiPMs);
3. Semiconductor detectors (*e.g.* CZT).

Although the coupling to the scintillator is indirect, the WSF gamma camera can be included in the first or second group, depending on the photodetectors used.

This chapter presents a review of the designs, components and performances of small FOV gamma cameras developed using these technologies.

2.1 Scintillators coupled to MaPMTs

2.1.1 MaPMTs

Also named position sensitive PMTs (PSPMTs), MaPMTs are basically PMTs where the amplified charge is distributed over several anodes, in a way that is sensitive to the position of arrival of photons on the photocathode. In order to produce electron clouds with spatial distributions that retain the position information of the incident photons, different dynode structures have been developed, the most efficient of which are proximity mesh dynodes [60] and metal channel dynodes [61], which confine electron clouds to narrow spots with low cross-talk between channels. Different anode readout schemes are also available, either by dividing the anode into separate pixels with individual readout for each channel or, alternatively, by crossing two layers of multiple parallel anode wires to produce x and y position encoding, in a charge sharing scheme similar to the Anger logic. Although "crossed-wire" readout is a simpler and less expensive method, requiring only four preamplifiers, it provides a lower count rate capability than individual anode readout, in which an event can be processed at an anode while the other anodes are available for detecting new events. The development of

microelectronics has lowered the complexity and cost of multiple channel readout, hence there has been an increasing use of ASICs to utilise the advantages of individual anode readout.

2.1.2 MaPMT-based gamma cameras

Many small FOV gamma imagers based on MaPMTs have been developed. A MaPMT design is better than using small PMTs because of the smaller anode pitch (the smallest PMT has about 1 cm diameter while the MaPMT anode pitch is in the order of a few mm), which allows better intrinsic spatial resolution results. The disadvantages of MaPMT gamma camera designs are typically related to photocathode non-uniformities which cause gain and sensitivity variations over the FOV, as well as to the dead areas near the edges of MaPMTs, which reduce the camera's sensitivity in these areas.

Pani *et al.* [62, 63] developed a breast-dedicated gamma camera based on a single 5 in (12.7 cm) diameter MaPMT (Hamamatsu R3292) with 28×28 crossed-wire anode readout, coupled to a segmented CsI(Tl) crystal of 11 cm diameter, with 2×2×3 mm^3 pixels separated by 0.25 mm of white epoxy. A general purpose collimator was used, with 2.5 cm long hexagonal holes and 0.25 mm septa. The camera was also equipped with a plastic paddle for mild breast compression, to reduce SCD. Clinical studies reported 80% sensitivity for lesions under 1 cm diameter, with mild breast compression, successfully demonstrating that the camera was able to detect sub-cm malignant tumours which could not be observed by prone scintimammography with a typical Anger camera. Using a ^{99m}Tc point source, the authors reported an intrinsic spatial resolution of 1.7 mm FWHM and extrinsic spatial resolution of 2.7 mm and 4 mm FWHM at a SCD of 0 and 2-3 mm, respectively. The measured energy resolution was 17% FWHM at 122 keV, detection efficiency of 25% without collimator and sensitivity of 592 cpm/μCi for the collimated system. The main drawbacks of this camera are related to the limited size and circular shape of the MaPMT which is not the most

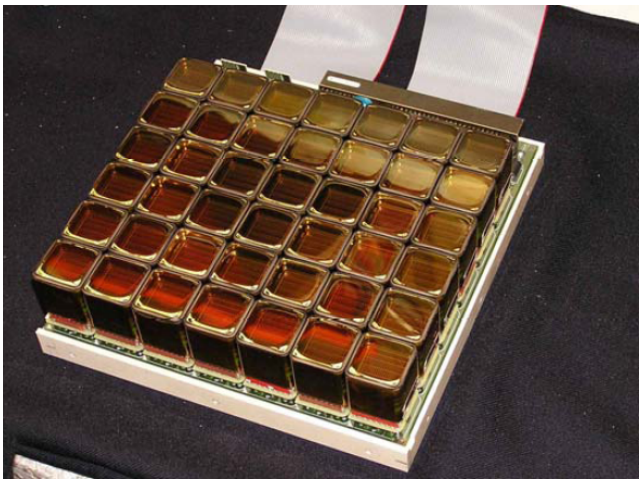

Figure 2.1: Array of 7×6 MaPMTs used in a 7×6 in^2 FOV camera built by Pani *et al.* [65].

appropriate for breast imaging, its dead area of 15 mm around the edges which limits the detection of tumours closer to the chest wall and the large thickness of the photocathode glass window which limits the spatial resolution and the FOV. For these reasons, the same authors have proposed new camera designs based on several square MaPMTs packed together and coupled to segmented NaI(Tl) [64, 65] or, more recently, using a continuous $LaBr_3$(Ce) crystal [66, 67]. The latter, due to its superior light yield, allowed achieving a very good energy resolution of 8-9% at 140 keV and sub-mm intrinsic spatial resolution, when coupled to a single MaPMT of 5×5 cm^2.

Nowadays, practically all of the MaPMT-based gamma cameras produced, except for small animal or surgical gamma imagers, are composed of several metal-packaged square MaPMTs grouped together for position sensitivity over a larger area, as exemplified in Figure 2.1. The concept is similar to the Anger design except that each device is position sensitive and its dimensions are small, allowing the assembly of compact camera heads.

A group from University of Virginia and Jefferson National Laboratory (USA) has also started the development of breast dedicated gamma cameras using a single MaPMT, R3292, but coupled to segmented CsI(Na) with 2×2×6 mm^3 pixels [68], which absorb approximately 70% of the 140 keV γ-rays transmitted by the collimator, taking into account the 79% fill factor. Energy resolution at 140 keV was poorer (26% FWHM) but uniformity was comparable and spatial resolution outperformed that of conventional Anger cameras: values of 2.6 and below 4 mm FWHM are reported for intrinsic and extrinsic spatial resolution at a 2 cm SCD, respectively, using a high resolution collimator (L=36 mm, d=1.22 mm, t=0.15 mm). Furthermore, the camera is mounted on a modified digital mammography unit, thereby allowing concurrent X- and γ-ray imaging under fixed compression, with subsequent image fusion (dual modality). This facilitates the accurate localisation of breast lesions, which isn't always clear from scintimammography images. The group's research evolved to prototypes based on multiple MaPMTs coupled to segmented NaI(Tl), in different configurations according to the application (planar scintigraphy, dual modality or SPECT). For planar scintimammography, a 20×15 cm^2 FOV camera was developed [69] using 8×6 Hamamatsu R7600-00-C8 MaPMTs coupled to a NaI(Tl) crystal array of the same size, with pixels of 2.9×2.9×6 mm^3 separated by 0.3 mm white epoxy and encapsulated with a 5 mm glass window. A circuit was built to combine the individual anode signals from all MaPMTs into 18×14 outputs, then read out by two 16-channel ADCs. Average energy resolution was 17.5% FWHM at 140 keV and a system spatial resolution of about 5 mm FWHM at 3-4 cm SCD was obtained using a high sensitivity lead collimator (328 cpm/μCi in a 10% energy window). Improved performance was achieved replacing the MaPMTs with the meanwhile available flat panel Hamamatsu H8500 models (also used by Pani *et al.*), which have a larger detection area and smaller dead spaces in the edges, resulting in a more compact and sensitive array [70]. Figure 2.2 shows the contrast between the first generation MaPMTs used in the early single-MaPMT

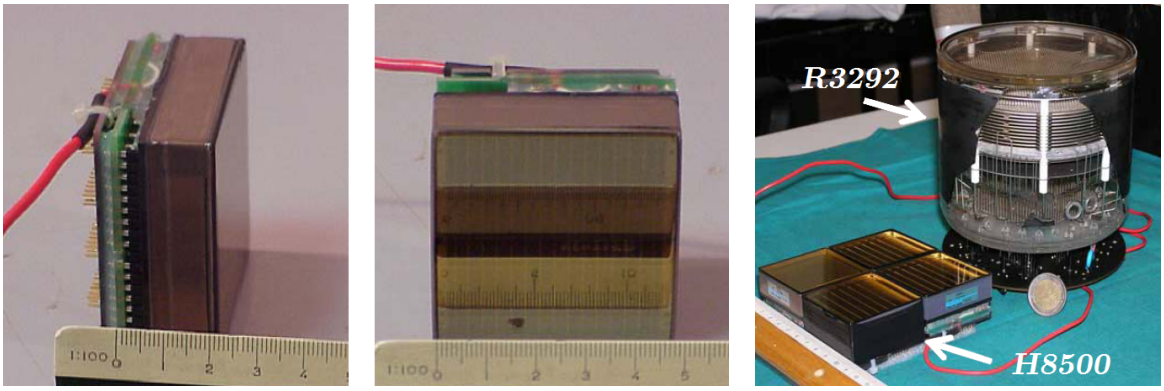

Figure 2.2: Compact flat panel H8500 MaPMT from Hamamatsu. A 2×2 array is shown in the right image, next to a first generation R3292 MaPMT (adapted from [72]).

cameras and this latest generation ones. With these devices, a camera with the same 20×15 cm^2 FOV was developed using half the number of MaPMTs (4×3) [71], reporting an average energy resolution of 13.7% FWHM at 140 keV, sensitivity of 155-384 cpm/μCi depending on the collimator used, intrinsic uniformity of 3.6% in the useful FOV and spatial resolution of 3.37 mm FWHM for a 3.2 mm crystal pitch. Even though a smaller crystal pitch results in better intrinsic spatial resolution (2.36 and 1.58 mm FWHM for 2.2 and 1.4 mm pitch, respectively), the performance of the 3.2 mm pitch camera was better, particularly in terms of contrast, which reflects in a better detection of small, low-contrast breast lesions. As a spin-off company from the radiation detector and imaging group of the Jefferson Lab, Dilon Diagnostics built a commercial gamma camera based on this technology, Dilon 6800®.

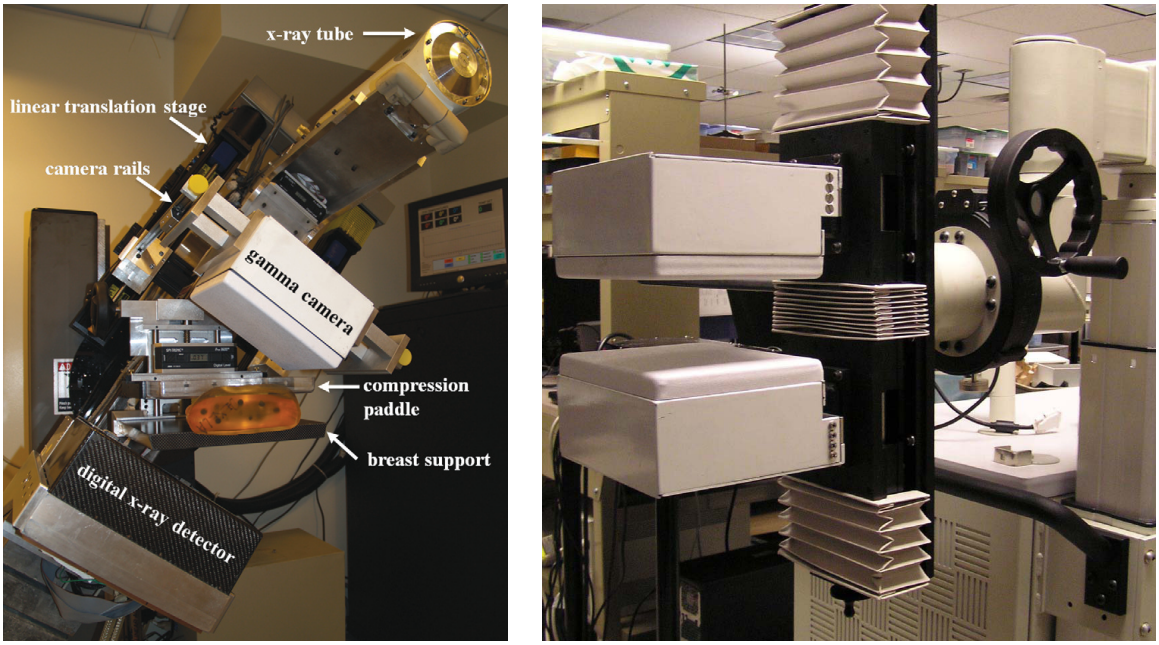

Figure 2.3: Dual modality breast tomosynthesis system [74] and dual head gamma camera [76] developed at University of Virginia and Jefferson Lab.

Other relevant developments from this group include a dual-modality breast tomosynthesis system [73, 74], as well as a dual-head camera based on two of the detector heads described above positioned on opposite sides of the compressed breast [75, 76], both shown in Figure 2.3. The increased sensitivity when using two detector heads resulted in a notable increase of the contrast and SNR in the joined image, but more importantly, it allowed detecting asymmetrically located small lesions that wouldn't be possible to identify with a single head. For these reasons, authors believe that the addition of the second camera head is well worth the extra cost and that the dual-head system should become the new standard for BSGI.

A dual detector system was also proposed by Garibaldi *et al.* [77], in which one camera is designed for high sensitivity and the other for high resolution. The first one, over which the breast is positioned, has a 15×20 cm^2 FOV of segmented NaI(Tl) (1.5 mm pitch) coupled to H8500 MaPMTs and uses a high sensitivity collimator. The second detector is based on a continuous $LaBr_3$(Ce) crystal coupled to a high QE H8500 and uses a 2 mm pin-hole collimator, providing a magnification of 2 and a FOV of about 2.5×2.5 cm^2. Besides allowing breast compression, the second camera can rotate and thus scan the breast for small tumours which may be located at a deep position where the first camera cannot reach (Figure 2.4).

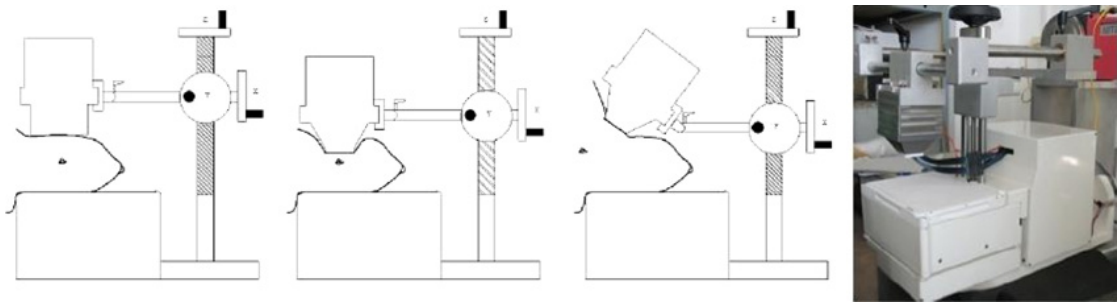

Figure 2.4: Dual head high-resolution and high-sensitivity gamma camera [77].

Fully portable MaPMT gamma cameras based on continuous CsI(Na) crystals were developed by Sánchez *et al.* [78, 79] (Valencia, Spain), integrating all components and electronics in a single case, requiring only a USB cable connection to a PC, for both data transmission and power supply to the camera. A first prototype was assembled using a single Hamamatsu R2486 MaPMT coupled to a 51×51×4 mm^3 CsI(Na) crystal with a white entrance face and black edges, which showed the best compromise between image compression and energy/spatial resolution. The camera showed an intrinsic spatial resolution of 2.1 mm and energy resolution of 13% FWHM at 140 keV within the useful FOV of 46 mm diameter, providing thyroid images with comparable quality to those obtained by a general purpose Anger camera. Performance was further improved by replacing R2486 with a H8500 MaPMT and using a slightly thicker crystal (4.6 mm), obtaining an even more compact and lighter camera, with a higher sensitivity and better intrinsic spatial resolution of 1.6 mm FWHM (Figure 2.5 left), aimed for intrasurgical imaging. Using an array of 4×4 H8500s to read out a crystal

Figure 2.5: Fully portable small FOV gamma cameras developed by Sánchez *et al.* [79].

of 104×104×4 mm^3, the useful FOV was enlarged to 95×95 mm^2, thus obtaining a portable multi-MaPMT gamma camera with potential application in scintimammography (Figure 2.5 right). Measured performance of this camera was 13-15% energy resolution at 140 keV, 2-2.3 mm FWHM intrinsic spatial resolution and sensitivity of 228 cpm/μCi at 4 cm SCD using a 3 mm pin-hole collimator with focal distance of 42 mm.

An example of a commercial single-MaPMT gamma imager intended for operating room imaging is NodeView^{TM}, a wireless hand-held camera developed by Intramedical Imaging, LLC (USA) [80], based on a segmented NaI(Tl) crystal of 1.5×1.5×6 mm^3 pixels coupled to a Hamamatsu 8500, with 49×49 mm^2 effective detection area. The camera head weights about 1.5 to 2 kg, depending on the collimator used (includes 3 mm of surrounding lead shield) and it is battery-operated. The spatial resolution achieved with a high-resolution collimator (L=2 cm, d=1.3 mm, t=0.2 mm) is around 2 mm FWHM at a 1-2 cm distance, with a sensitivity of 300 cpm/μCi and average energy resolution of 12% at 140 keV. Clinical applications are in radio-guided surgeries such as occult lesion localisation, sentinel lymph node biopsy or parathyroidectomy.

Similarly to Pani *et al.*, also Yamamoto *et al.* (Japan) [81] took advantage of the high light output of $LaBr_3$(Ce), approximately 1.7 larger than NaI(Tl), to develop a high-resolution 5×5 cm^2 FOV gamma camera, by coupling a 2 mm thick $LaBr_3$(Ce) crystal (about 40% detection efficiency for 140 keV) to a Hamamatsu H8500 (Figure 2.6). Measurements performed with ^{57}Co showed an energy resolution of 8.9% at 122 keV and intrinsic spatial resolution of 0.75 mm FWHM. The sensitivity of this camera

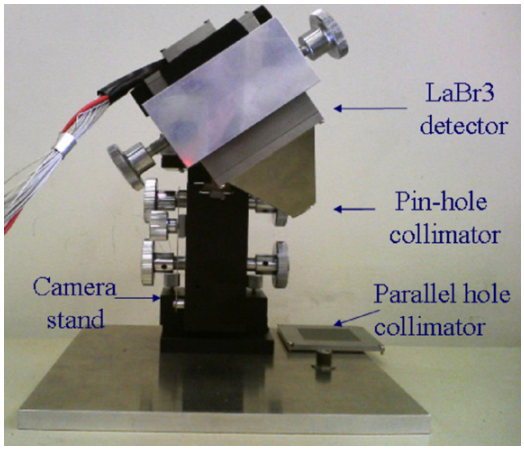

Figure 2.6: $LaBr_3$(Ce) gamma camera [81].

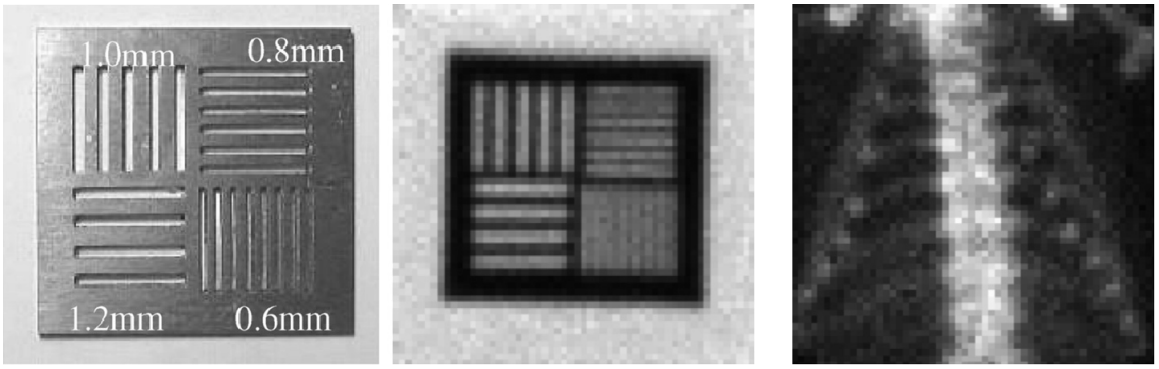

Figure 2.7: Photo/image of bar pattern phantom used to evaluate spatial resolution (left); image of mouse injected with 540 μCi of ^{99m}Tc-HMDP, 7 h acquisition time (right) [81].

using a pin-hole collimator (d=0.5 mm) at 20 mm distance was 0.0017%, which allowed obtaining the ^{99m}Tc-HMDP image of a mouse shown in Figure 2.7 (right) only after an acquisition time of 420 minutes, nevertheless with an impressive detail. Despite the very good γ-imaging performances observed, the main problem with $LaBr_3$(Ce) is its high fragility and hygroscopicity, which prevent the reliable production of segmented crystals and lead to an early degradation of continuous crystals. Only two years after the production of the crystal, authors observed that more than half of the camera's FOV produced no signals.

2.2 Scintillators coupled to solid-state photodetector arrays

Solid-state photodetectors represent a very attractive alternative to MaPMTs for the readout of scintillation light in small FOV gamma cameras, due to several reasons:

- smaller size and weight which allow the development of very compact gamma cameras;
- higher quantum efficiency in the visible spectrum;
- lower bias voltage and power consumption;
- lower cost;
- in the case of SiPMs, very high gain (comparable to PMTs) and single photon detection capability.

Small photodiodes with a few mm^2 active area can then be individually coupled to scintillator pixels of similar cross-section, producing high-performance gamma imagers. Furthermore, because of their very good timing resolution and insensitivity to magnetic fields, semiconductor photodetectors have found applications in PET and PET/MRI scanners [82–84], as well as in other fields such as high-energy physics and astronomy [85–88].

Silicon is the preferred semiconductor material to make photodiodes. It has a bandgap of 1.12 eV, which means that only photons with sufficient energy to excite electrons across this bandgap will produce significant photocurrents. This makes Si photodiodes sensitive in the range of 250 to 1100 nm, thus covering well the emission spectra of almost all scintillators and Cherenkov radiators used in particle physics, radiation detection and medical imaging. Besides that, comparatively to Germanium, Si photodiodes generate less noise due to the higher bandgap (Ge bandgap is 0.67 eV). Other important features that make Si the best material for photodiodes (as of today) are the high purity of Si samples that can be achieved and the fact that the Si allows the easy formation of a top layer passivation by SiO_2 (top protective layer), one of the best insulators with excellent transmission of light, which adheres well to the underlying Si. Gallium Arsenide (GaAs), with a bandgap of 1.4 eV, would be even more advantageous for low noise photodiodes, but it lacks this important property [89].

The main drawback of photodiodes, especially of those without internal charge amplification, has to do with electronic noise due to leakage currents. Since they are primarily caused by the thermal generation of charge carriers in the bulk material, leakage currents increase with temperature and also with the volume of the photodiode. In devices with no internal gain, noise is further increased in the pre-amplification electronics, resulting in a limited capacity to detect scintillation light. In practice, this degrades energy resolution and often imposes a minimum energy for the γ-rays which can be detected by a photodiode coupled to a scintillator. Devices with internal gain such as APDs and SiPMs have a much higher SNR and light sensitivity, but require highly controlled environment conditions for a stable operation because of the temperature and bias voltage dependencies.

2.2.1 Solid-state photodetectors (SSPDs)

A brief review of the working principle of different SSPDs is presented, followed by a survey of existing small FOV gamma cameras based on scintillators coupled to SSPDs.

Si PiN photodiodes

The principle of the Si PIN photodiode is basically the same as the standard photodiode, but with an added layer of intrinsic (undoped) Si between the p and n layers (Figure 2.8). This intrinsic layer of about 300 μm reduces capacitance (inversely proportional to the distance) and leakage current, thus reducing electronic noise. Because Si PIN diodes have no internal charge amplification, they require a charge sensitive preamplifier and a low bandwidth filter amplifier for the detection of low light levels, which slow the signal. On the other hand, the absence of internal gain has the advantage of great signal stability. Position sensitive arrays of a large number of PIN photodiodes are easy to produce, cheap and reliable. Although PIN diodes with areas of 10 cm^2 or more are now available, their capacitance (and consequently,

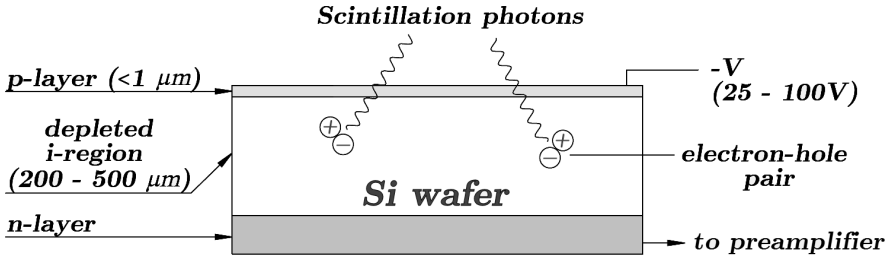

Figure 2.8: Basic layout of a conventional PIN photodiode (adapted from [47]).

their noise) increases proportionally to the area. State of the art PIN photodiodes are able to detect minimal signals of 200-300 photoelectrons, with a bandwidth of a few hundred kHz.

Silicon drift detectors

SDDs are photodiodes with a particular anode configuration in which a very small circular anode is surrounded by a series of annular electrodes, biased so as to create an electric field that guides the photoelectrons towards the central anode. A significant reduction of the electronic noise is achieved due to the small area of the anode, which keeps the capacitance very small. Moreover, since the active volume of the diode can be enlarged by adding more electrodes while keeping the same anode area, capacitance does not increase with the detector's area. To take advantage of the low output capacitance (in the order of 100 fF) and further optimise the noise reduction, part of the front-end preamplifier can be integrated on the detector chip, close to the anode, thus minimising leakage current.

Avalanche photodiodes

APDs are photodiodes with an internal gain mechanism due to the high electric field created at the p-n junction by operating at a higher reverse bias voltage. Photoelectrons accelerated by this electric field acquire enough energy to create electron-hole pairs by impact ionisation. Both initial and additional electrons may then undergo high acceleration again and create further electron-hole pairs, thus initiating an avalanche. The threshold value for the electric field above which there is enough kinetic energy to generate electron-hole pairs, called impact ionisation threshold, is 1.75×10^5 V/cm for electrons. The multiplication gain of APDs is usually moderate, between 50 and 200, but allows an important reduction of noise levels at higher bandwidths, *i.e.* it results in a better SNR. Higher gains of up to 10^4 are possible but require highly controlled temperature and bias voltage conditions because the APD has to be operated extremely close to the breakdown voltage. Despite having a higher sensitivity, APDs have not yet achieved single photon response. The smallest light signals detectable by a state of the art APD need to be some tens of photons and the bandwidths can reach hundreds of MHz. The largest commercially available APDs have an area of about 2.5 cm^2.

Silicon photomultipliers

The SiPM consists of an array of APDs operated in Geiger mode (G-APDs), *i.e.* at a reverse bias voltage higher than the breakdown voltage. At such overvoltage, the electric field becomes so strong that avalanches are not only initiated by electrons as in linear mode APDs, but may also be started by holes (for which the impact ionisation threshold is 2.5×10^5 V/cm) and therefore, the avalanche process develops in two directions. Furthermore, the avalanche becomes self-sustaining, needing to be quenched by a high-ohmic serial resistor or by an active quenching circuit. A gain of up to 10^6-10^7 is achievable, which allows detecting single photons. However, when operating in Geiger mode, a single APD has the same output amplitude regardless of the number of incident photons or their energy, therefore being of little interest for scintillation light readout. SiPMs overcome this limitation by connecting in parallel many units of these devices, each with its individual quenching resistor, such that the output of the array is given by the sum of the outputs of individual cells. In this way, if the number of incident photons is less than the total number of cells, the output charge of the SiPM is proportional to the number of incident photons. Due to their high gain and photon detection efficiency, SiPMs are then able to detect single photons at room temperature. Current dimensions of SiPMs are limited to less than 5×5 mm^2, because of the random noise introduced by thermally generated electrons in the silicon, which scales with the area.

Since they are used as photodetectors in the WSF gamma camera presented in this work, SiPMs are explored in more detail in chapter 3.

2.2.2 SSPD-based gamma cameras

There have been many efforts with good results in the application of SSPDs for scintillation light readout in small FOV gamma cameras.

Choong *et al.* [90, 91] developed a compact 16-module camera based on 8×8-pixel modules of segmented CsI(Tl) with pixel size of $3\times3\times5$ mm^3, coupled to low noise Si PIN photodiodes (with QE of 80% at 540 nm), using a custom integrated circuit capable of reading out the 64 channels of each module and determining the position of the pixel with maximum output from all modules. Each module had an active area of $2.4\times2.4\times1.4$ cm^3, resulting in a very compact assembly with a maximum FOV of 9.6×9.6 cm^2, essentially without dead areas between modules. Performance was characterised using 2×2 modules, demonstrating an average energy resolution of 13.4% FWHM for 140 keV at room temperature, intrinsic spatial resolution of 3.3 mm and system resolution of 8.7 mm FWHM at 10 cm SCD using a high-resolution collimator. Disadvantages of this camera are the significant number of dead or inactivated pixels due to noise, which account for 10-20% of all pixels, and the minimum dead time per event of 10 μs, which nevertheless remains adequate for single photon imaging.

Digirad Corporation (USA) developed a 21.2×21.2 cm^2 FOV commercial camera based on Si PIN diodes coupled to 3×3×6 mm^3 CsI(Tl) pixels (2020tc Imager®). This camera produced better quality images than those of a typical Anger camera [93], mainly due to better intrinsic spatial and energy resolution, as well as a closer proximity to the patient and smaller dead space around the edges (12 mm against common 75 mm in Anger camera). Even though it is not particularly lightweight (135 kg), the camera (Figure 2.9) can be easily transported to a patient's bedside or to surgery and perform a wide variety of procedures, including scintimammography.

Figure 2.9: Digirad's 2020tc® Imager[92].

Several prototypes of gamma cameras based on silicon drift detectors have been assembled by Fiorini *et al.* (Italy/Germany), consisting of arrays of closely packed SDDs coupled to a continuous CsI(Tl) crystal and using Anger positioning logic. Initial prototypes were composed of several SDDs with only a few mm^2 each, reaching total active areas of up to 6.7 cm^2 [94–96], with 100% fill factor. These small prototypes demonstrated an energy resolution of about 14% FWHM at 122 keV and intrinsic spatial resolution between 200 and 400 μm, at -10°C, which allowed resolving fine structures with good linearity, as shown in Figure 2.10. The advantage of this SDD-based camera comparatively to pixelated detectors is that a very good intrinsic spatial resolution is achievable with a pixel size about an order of magnitude larger than the target resolution, resulting in a reduction of the number of electronic readout

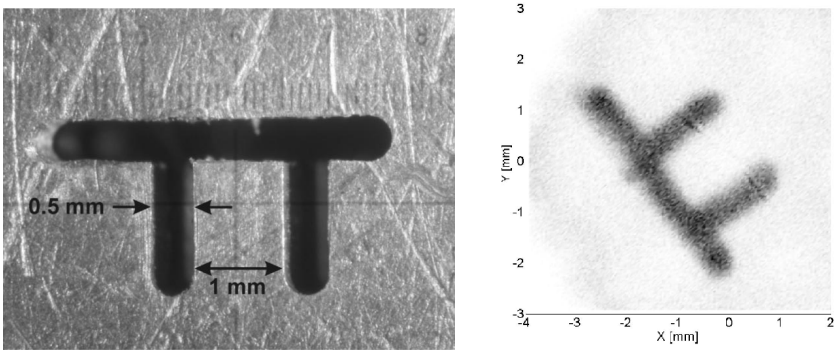

Figure 2.10: High-resolution lead mask and corresponding image obtained with the SDD camera developed by Fiorini *et al.* [96].

channels.

In the context of the HICAM project, supported by the European Commission, larger prototypes based on this technology were built, using new SDDs with 1 cm^2 active area and a very low leakage current of 100 to 200 pA/cm^2 at room temperature [97]. These allowed assembling a camera with a UFOV of 10.8×8.7 cm^2 by putting together 20 linear monolithic arrays of 5 SDDs each (Figure 2.11), read out by custom-designed ASICs. Using moderate cooling (-5°C), authors report an intrinsic spatial resolution of 0.8 mm and energy resolution of 20% FWHM at 140 keV [98]. Clinical trials demonstrated a higher performance of this compact imager in comparison to a commercial camera (Siemens E.CAM®), allowing the identification of lymph nodules undistinguishable with the commercial camera (Figure 2.12).

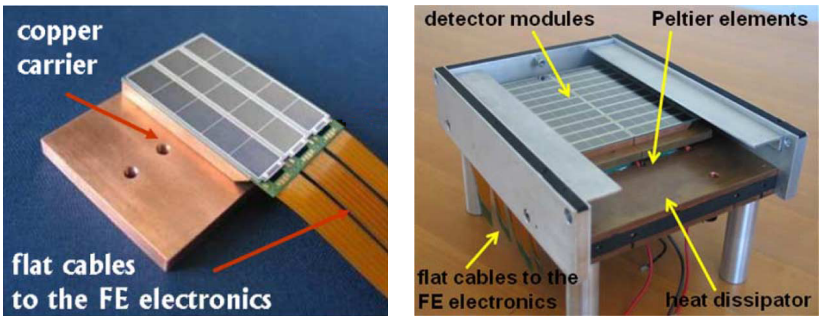

Figure 2.11: HICAM camera, based on SDD modules [98].

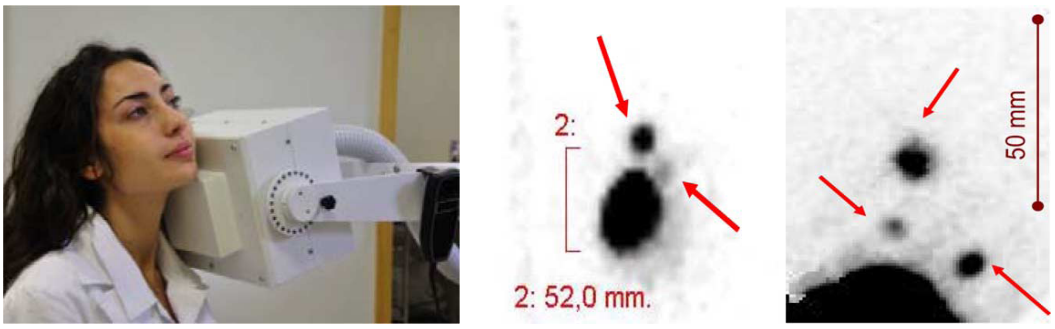

Figure 2.12: HICAM camera positioned close to patient (left); lymphoscintigraphy images with Anger camera (middle) and HICAM (right). Arrows indicate visible nodules [98].

Menard *et al.* [99] (France) developed a hand-held gamma camera for radio-guided surgery in cancer treatment, named POCI (per-operative compact imager). The final prototype [100] consists of a head module composed of an interchangeable collimator and a 3 mm thick continuous CsI(Na) crystal optically coupled to an intensified position-sensitive diode (IPSD). The IPSD is composed of a 40 mm diameter proximity focusing, double micro-channel plate image intensifier tube (Hamamatsu V5182U) coupled to a custom made 42×42 mm^2 duo-lateral position sensitive diode. The camera has a 40 mm diameter FOV, an outer diameter of 9.5 cm, length of 9 cm and weights 1.2 kg. The extrinsic spatial resolution when imaging a 0.5 mm diameter plastic tube filled with ^{99m}Tc in the face of a high-sensitivity tungsten

collimator (L=13 mm, d=1 mm, t=0.3 mm) was 3.2 mm FWHM, with a corresponding sensitivity of 621 cpm/μCi. Energy resolution was 32% at 140 keV. The camera has been successfully evaluated as an aid to the surgical treatment of cancer, confirming its value in the identification of sentinel lymph nodes [101]. Aiming for the same application, this group has recently developed a hand-held camera based on a 5 mm thick $LaBr_3$(Ce) crystal coupled to a Hamamatsu H9500 MaPMT, for which it could be included in section 2.1.2. Preliminary tests of this camera [102] showed a better energy resolution of 17.4% at 122 keV and an intrinsic spatial resolution of 0.65 mm FWHM.

There have been several efforts to develop high spatial resolution gamma imagers using columnar CsI(Tl) and CCD or CMOS sensors to read out the scintillation light [103–106]. In order to minimise the dark current effect and increase SNR, these systems use CCD cooling and electron-multiplying CCDs, which amplify the charge signal during readout, or image intensifiers, which amplify the scintillation light before detection. These photon-counting cameras can achieve an excellent spatial resolution in the order of tens of μm; however, they have low energy resolution and sensitivity, worsened by optical tapers, lenses or pin-hole collimators, which are used to enlarge the FOV, limited by the small size of the sensors. Further developments towards better energy resolution, faster readout and larger sensitive areas are required for a more effective application of these technologies in the clinical field.

Regarding the use of APDs and SiPMs in scintillation imagers, the main application has been in PET, *e.g.* [45, 82, 83, 107], due to the higher light output of crystals for the 512 keV and thus higher SNR of the photodetectors. However, these photodetectors have also been used to develop small FOV single-photon imagers. Després [108] and Kim *et al.* [109] have shown how the use of a position-sensitive APD with 8×8 mm^2 coupled to a match-sized CsI(Tl) crystal, can reach sub-mm intrinsic spatial resolution and 16% FWHM energy resolution at 140 keV. Position sensitivity is obtained through an Anger-like charge sharing scheme using a resistive layer at the back face of the APD, with 4 readout electrodes, one at each corner. However, this positioning method results in pincushion spatial distortions which degrade uniformity and reduce the UFOV, requiring correction. Furthermore, the above mentioned results were achieved using nitrogen cooling (-41°C) to reduce leakage current. For these constraints, as well as the stability of temperature and bias voltage necessary for a good performance, it remains challenging to build a gamma camera based on arrays of APDs.

Due to their higher sensitivity and stability, SiPMs can be applied in a gamma camera operating at room temperature or with only moderate cooling. This has recently been accomplished in a small prototype by Yamamoto *et al.* [110], who coupled a Hamamatsu S11064-050P (composed of 3×3 mm^3 SiPMs) to a segmented 12×12×6 mm^3 YSO crystal (Figure 2.13), with a 2 mm thick light guide. YSO was chosen because it has a good light output, no natural radioactivity and it is not hygroscopic, allowing the inexpensive produc-

tion of very small pixels (0.7 mm pitch) and not requiring hermetic sealing. Using a source of ^{57}Co, an intrinsic spatial resolution of 0.8 mm was measured at room temperature (20°C), with a corresponding average energy resolution of 24.4% FWHM at 122 keV. In addition, the system showed an extrinsic spatial resolution of 1.25 mm FWHM at a SCD of 1.5 mm and detection efficiency of 0.0051%, using a parallel-hole collimator made of tungsten plastic (L=5 mm, d=0.5 mm, t=0.1 mm), with each hole positioned over a corresponding YSO pixel. A small mouse injected with approximately 1 mCi of ^{99m}Tc-HMDP was also imaged, with results shown in Figure 2.14.

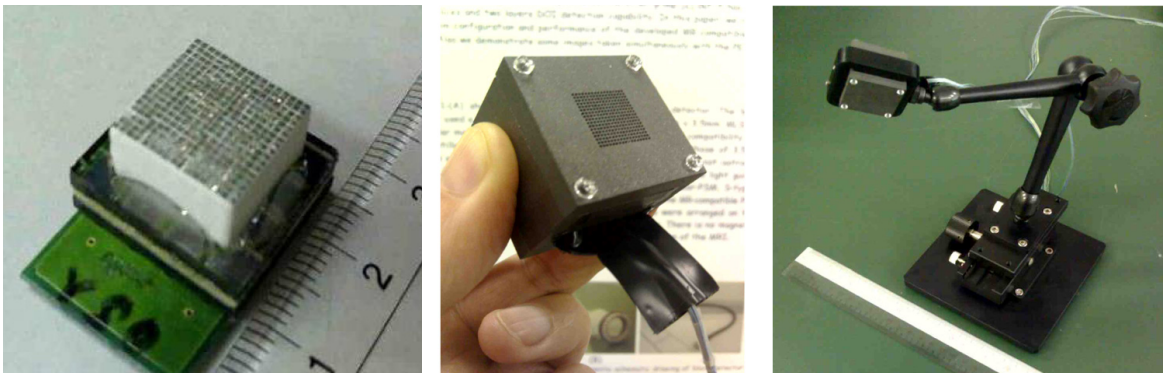

Figure 2.13: Small SiPM-based gamma camera system using segmented YSO [110].

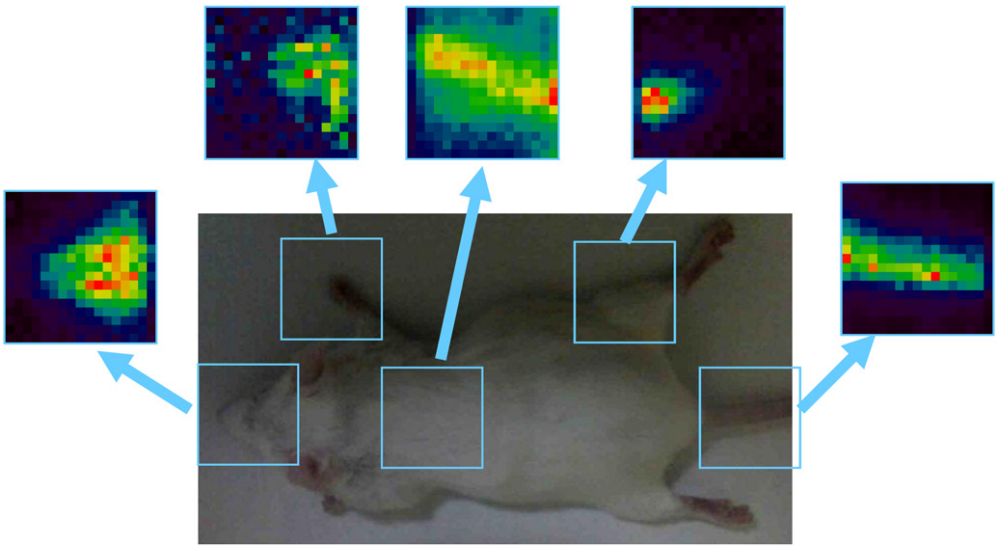

Figure 2.14: Different parts of a mouse imaged with 12×12 mm^2 SiPM-based gamma camera, after injection with 1 mCi of ^{99m}Tc-HMDP (10 minutes aquisition time) [110].

2.3 Semiconductor detectors

2.3.1 Cadmium telluride and CZT

Cadmium telluride (CdTe) and cadmium zinc telluride (CdZnTe, or CZT) are compound semiconductors that have been extensively investigated for nuclear medicine. Some important properties of these materials are listed in Table 2.1. Comparatively to Si or Ge, CdTe and CZT have a wider bandgap and higher resistivity, hence they can operate at near room temperature without generating excessive electronic noise.

Table 2.1: Properties of semiconductor materials used in single-photon gamma imaging.

Material	Z	Density (g/cm^3) [a]	ρ (Ωcm) [b]	Bandgap (eV) [b]	Pair creation energy (eV) [b]	$\mu_e\tau_e$ (cm^2/V) [b]	$\mu_h\tau_h$
CdTe	48,52	5.85	10^9	1.44	4.43	10^{-3}	10^{-4}
CZT	48,30,52	5.82	10^{10}	1.57	4.6	10^{-2}-10^{-3}	10^{-5}
Si	14	2.33	10^4	1.12	3.62	>1	~1
Ge	32	5.32	50	0.67	2.96	>1	>1

[a] From Henkin *et al.*[111] [b] From Del Sordo *et al.*[112].

Furthermore, these materials have higher density and effective atomic number and their photoelectric absorption for typical γ-ray energies is about 100 times higher than in Si. The appeal of this family of detectors for nuclear medicine is based on several factors, which combine the potential for great performance, both in energy and spatial resolution:

- Direct conversion of γ-rays into a measurable electric signal, eliminating intermediate scintillation stage and the need for photodetectors (advantage in terms of compactness, weight and portability, particularly in relation to traditional NaI-PMT technology).

- Relatively large number of electron-hole pairs per keV of γ-photon energy deposited, combined with a low Fano factor (ratio of the variance of a random variable to its mean), thereby producing a low statistical variation in signal response to mono-energetic photon irradiation, *i.e.*, a very good energy resolution (about 3% FWHM at 140 keV). A better energy resolution significantly improves the scatter rejection and may allow multiple isotope imaging.

- Small charge cloud created by γ-rays, which defines a limit for the intrinsic spatial resolution of less than 250 μm, for crystal sizes and γ-ray energies in the medically useful range. In practice, the intrinsic spatial resolution of CdTe/CZT detectors is equal to the electrode (pixel) size, thus a high resolution comes with the price of thousands of individual electronic channels required for a ~10×10 cm^2 detection area. Improvements

in crystal growth methods, packaging, microelectronic circuitry and computer power, allowed the production of CdTe/CZT cameras with suitable sizes for medical imaging.

About 7 mm of CZT are required to achieve the same detection efficiency as in a typical NaI(Tl) gamma camera [35]. However, the thicker the substrate, the harder it is to produce detectors with smaller pixels. In fact, detectors with sub-mm pixels have only been realised on thin substrates, 1-2 mm thick or less. Moreover, in a CZT crystal, the collection time for holes is much longer than for electrons (because of their lower mobility), a phenomenon which becomes even more pronounced in thicker crystals. This affects the time response of CdTe/CZT, so their application is currently limited to single-photon imaging. Because the production yield of uniform crystals with sensitive areas of several cm^2 is low (due to the high level of defects and charge traps which deteriorate the signal and reduce the charge collection efficiency), large detector areas are achieved by assembling many modules, each composed of a few small-area pixelated detectors. The production of CdTe and CZT detectors is relatively expensive, so they are being more used in specialised, small FOV applications such as radio-guided surgery ($\sim 5\times5$ cm^2) or breast imaging (up to 24×16 cm^2).

2.3.2 CdTe/CZT-based gamma cameras

CdTe and CZT gamma cameras have been developed by several companies and research institutes, achieving comparable or superior imaging performances than scintillator-based cameras, despite the lower sensitivity. For instance, Blevis *et al.*[113, 114] (GE Healthcare) reported the development of a CZT gamma camera prototype with a 20×20 cm^2 FOV for application in scintimammography. The camera consists of 25 detector modules, each with 4×4 cm^2 and 256 pixels of $2.5\times2.5\times5$ mm^3, and has collimators with square holes matched to the detector's geometry. In this way, the system resolution is determined only by the collimator, because the collimator hole + pixel can be considered as an independent detector, as opposed to scintillation cameras where collimator and crystal contribute independently to the spatial resolution and therefore need to be considered separately. Despite a 24% sensitivity loss in comparison to an Anger camera, this prototype showed a superior performance in terms of energy resolution (6.5% vs. 8.7% FWHM at 140 keV) and a gain of about 1 mm in system spatial resolution for SCDs of 0 to 6 cm. Phantom tests and clinical trials confirmed the better imaging performance of the CZT camera and its ability to reliably detect 5 to 10 mm breast tumours. GE Healthcare currently commercialises a breast-dedicated dual-head gamma camera based on this technology, Discovery® NM750b.

Another big player in the industry of CZT-based cameras for molecular breast imaging is Gamma Medica, Inc. (USA), with LumaGEM®, a dual-head imager with a FOV of 16×20 cm^2 and 8 mm dead space at the edges. According to the manufacturer [115], this camera has an intrinsic spatial resolution of 1.6 mm and energy resolution of 4.5% FWHM. Images are acquired with light breast compression between the two camera heads, in standard mammography views for easier comparison and interpretation of results. Clinical trials demonstrated the good performance and usefulness of this camera, which allows reducing the duration of the exam and the administered dose from 20 mCi to 8 mCi [116].

Figure 2.15: LumaGEM® system [115].

Eisen *et al.* [117], at Soreq Nuclear Research Centre (Israel), realised the third generation of a solid-state gamma camera, NUCAM3, based on 528 CZT detectors of 16 pixels each produced by eV Products, corresponding to a total active area of 18.5×20.1 cm^2. Using a very low-noise 64-channel readout ASIC and a square parallel-hole collimator matched to the pixel pitch (2.1 mm), the camera shows an excellent energy resolution (4.5% FWHM at 140 keV and 9.5% at 59.6 keV), a spatial resolution of 7.5 mm at 10 cm and photopeak sensitivity of 190 cpm/μCi, outperforming an Anger camera in the production of small detail images.

A small CdTe gamma camera was developed by Tsuchimochi *et al.* [118], aimed for radio-guided surgery of metastatic lesions and other imaging applications amenable to its 4.5×4.5 cm^2 FOV. The detector area is obtained by stacking 32 modules from Acrorad (Japan), each consisting of a row of 32 pixels with 1.2×1.2×5 mm^3, in a total of 1024 pixels, read out by eight 128-channel ASICs. The CdTe array was assembled in block with a tungsten collimator matched to the detector pixels (L=10 mm, t=0.2 mm) and the whole camera assembly with lead housing had outer dimensions of 15.2×16.6×6.5 cm^3, weighting 2.7 kg. At 140 keV, the energy resolution of a single pixel at the centre of the FOV was 4.2% FWHM and the mean resolution of the camera about 7.8%. The spatial resolution had a mean value of 1.56 mm FWHM at the face of the collimator, 6.3 and 11.2 mm at 5 and 10 cm SCD, respectively.

Smaller semiconductor hybrid detectors have been developed, where the back side of a CdTe/CZT crystal is attached pixel-by-pixel via bump bonding to a pixelated readout ASIC. This is the case of MediPROBE, a CdTe camera developed at University and INFN Napoli (Italy), where a ∼14×14×1 mm^3 crystal from Acrorad is coupled to a photon-counting Medipix2 chip, developed in the framework of an European collaboration [119]. The back side of the crystal is pixelated in a matrix of 256×256 square pixels of 45 μm side and 10 μm inter-

pixel gap, corresponding to the 55 μm pitch of the Medipix2 cells. For such a small pixel size, the total charge originated from a 140 keV photon interaction spreads over several adjacent pixels, degrading photon-counting capability and making it necessary to apply off-line cluster analysis to the sequence of image frames. Since a pixel hit is counted for any deposited energy above a given threshold (20 keV) and charge is spread, spectroscopic information is lost and energy windowing becomes impracticable. Nonetheless, and despite the low absorption of 1 mm thick CdTe (34% for 140 keV), the intrinsic imaging performance of this camera is good, particularly for applications involving small volumes such as lymphoscintigraphy. Authors [120, 121] report a best measured intrinsic spatial resolution of 0.16 mm and a system resolution of 5.6 mm FWHM at 5 cm SCD with a sensitivity of 73 cpm/μCi, using a pin-hole collimator (0.94 mm effective aperture), indispensable to increase the imaging FOV.

Another example of hybrid detector is the SemiSPECT system assembled at University of Arizona [122] (Figure 2.16), composed of a ring of eight CZT detectors ($\sim$27×27×2 mm^3) with the bottom electrode patterned into a matrix of 64×64 pixels of 380 μm pitch, each welded onto a corresponding cell of a custom readout ASIC via indium bump bonding. Each cell integrates the current induced in the pixel electrode and transfers it as voltage to external electronics by multiplexer circuitry, with the entire array being read out at a frequency of about 1 kHz. A pixel pitch of 380 μm results in a better charge collection, with a much lower spread than in the MediPROBE system described above. Furthermore, because signals from 3×3 pixels are recorded for each valid γ-ray event, an energy resolution of $\sim$10% is possible with this system. At a temperature of 5°C, maintained by thermoelectric coolers and coolant circulation through an external chiller, and using a hollow cylinder with 0.5 mm pin-holes matched to the detectors, the average linear spatial resolution computed over the FOV was about 1.45 mm along each axis. The overall detection efficiency of the system was about 0.5×10^{-4} using a 20% energy window.

Figure 2.18 shows the bone image of a mouse injected with 6.8 mCi of ^{99m}Tc-MDP and

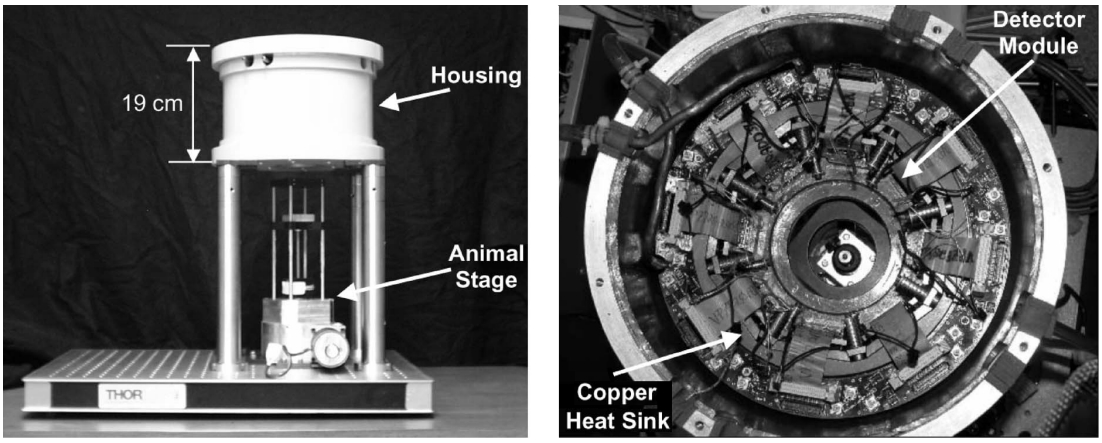

Figure 2.16: Photos of outside (left) and inside (right) views of SemiSPECT system [122].

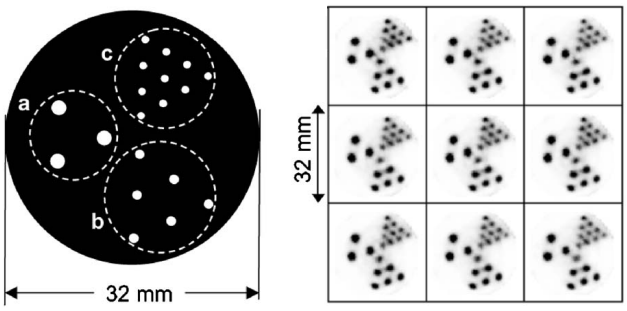

Figure 2.17: Diagram of phantom with holes of 2, 1.5 and 1 mm diameter filled with ^{99m}Tc (left) and SPECT image slices with 0.5 mm separation (right) [122].

imaged nearly 2 hours later, after euthanasia. Since the mouse was 11 cm long, it was scanned over four adjacent longitudinal positions, 2 minutes in each.

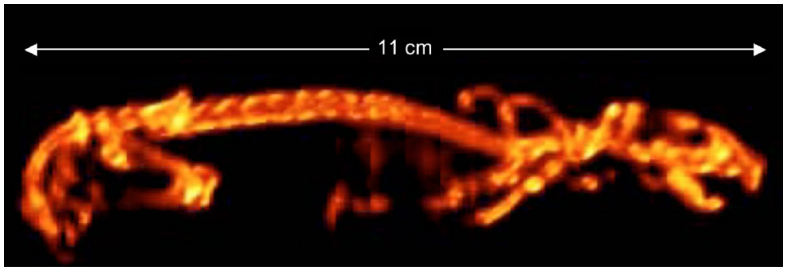

Figure 2.18: Volume-rendered image of a mouse injected with ^{99m}Tc-MDP, obtained with SemiSPECT system [122].

It is foreseeable that CdTe and CZT will continue to play a major role in the development of high-resolution gamma cameras, since they have allowed some of the best performances obtained so far and given that there's still room for improvement. Some challenges remain to overcome, such as the production of uniform large volumes with fewer defects, improvement of timing performance and further reduction of the spectral tail on the low energy side of the photopeak, as well as the development of nearly 100% active detector volume and collimation schemes worthy of the fine detection performance that CZT can potentially achieve.

2.4 Overview

A comparative summary of the most relevant small FOV gamma camera systems presented in this chapter is provided in Table 2.2.

Table 2.2: Overview of small FOV gamma camera systems described in the literature.

1. Scintillators coupled to MaPMTs

Year	Crystal		MaPMT	Detector FOV (cm^2)	Energy resolution @ 140 keV	Intrinsic spatial res. (mm)	Breast compress.	Extrinsic measurements [1]			Observations	Ref.
	type	size (mm)						SCD (cm)	Spatial res. (mm)	Sensitivity (cpm/µCi)		
2000	segm. CsI(Na)	2 × 2 × 6	R3292	10.6 cm ø	26 %	2.6	yes	3	4.1	36	used in dual modality	[68]
1997	segm. CsI(Tl)	2 × 2 × 3	R3292	11 cm ø	17 % (122 keV)	1.7	yes	2-3	4	592	15 kg	[62]
2006	segm. NaI(Tl)	2 × 2 × 6	7 × 6 H8520	15.2 × 17.8	16.5 %	2	yes	2.5	4	200-300	IMI project	[65]
2007	segm. NaI(Tl)	1.5 × 1.5 × 6	H8500	5 × 5	12.1 %	1.8	- [3]	1	2	300	NodeView™	[80]
2006	contin. CsI(Na)	100 × 100 × 4	2 × 2 H8500	9.5 × 9.5	13-15 %	2-2.3	no	4	5	228	3 kg with collimator	[79]
2006	segm. NaI(Tl)	3.2 × 3.2 × 6	4 × 3 H8500	20 × 15	13.5 %	3.37	yes	2.7	4	155	used in Dilon 6800®	[71]
2010	cont. $LaBr_3$(Ce)	50.8 × 50.8 × 2	H8500	5 × 5	8.9 %	0.75	- [3]	- [2]			40% effic. @140 keV	[81]

2. Scintillators coupled to solid-state photodetector arrays

Year	Crystal		SSPD	Detector FOV (cm^2)	Energy resolution @ 140 keV	Intrinsic spatial res. (mm)	Breast compress.	Extrinsic measurements [1]			Observations	Ref.
	type	size (mm)						SCD (cm)	Spatial res. (mm)	Sensitivity (cpm/µCi)		
2002	segm. CsI(Tl)	3 × 3 × 5	Si PIN (3×3 mm^2)	4.8 × 4.8	13.4 %	3.3	- [3]	10	8.7	492	10-20% dead pixels	[90]
2000	segm. CsI(Tl)	3 × 3 × 6	Si PIN (3×3 mm^2)	21 × 21	12.8 %	- [2]	no	10	7	121	Digirad 2020tc®	[92]
2011	segm. CsI(Tl)	3 × 3 × 6	Si PIN (3×3 mm^2)	25 × 20	7.9 %	3.3	yes	10	7.4	132	Dilon 6800 Acella®	[92] [4]
2010	contin. CsI(Tl)	120 × 96 × 10	SDDs (1 cm^2)	12 × 10	20 %	0.8	no	4	2.67	73	HICAM, at -5°C	[98]
2002	contin. CsI(Tl)	40 ø × 3	Intensified PS diode	4 cm ø	32 %	2.3	- [3]	1	3.9	621	POCI, 1.2 kg	[100]
2011	segm. YSO	0.6 × 0.6 × 6	SiPMs: S11064-050P	1.2 × 1.2	24 % (122 keV)	0.8	- [3]	0.9	1.8	- [2]	at room temperature	[110]

3. Semiconductor detectors

Year	Crystal			Detector FOV (cm^2)	Energy resolution @ 140 keV	Intrinsic spatial res. (mm)	Breast compress.	Extrinsic measurements [1]			Observations	Ref.
	type	pixel size (mm)	total					SCD (cm)	Spatial res. (mm)	Sensitivity (cpm/µCi)		
2003	CZT	2.5 × 2.5 × 5	6400	20 × 20	6.5 %	2.5	yes	4	4	113	GE Healthcare prototype	[113]
2011	CZT	1.6 × 1.6 × 5	1250	16 × 20	4.5 %	1.6	yes	- [2]			LumaGEM®, dual-head	[115]
2002	CZT	2.1 × 2.1 × 5	8448	18.5 × 20.1	4.5 %	2.1	- [3]	10	7.5	190	NUCAM3	[117]
2003	CdTe	1.2 × 1.2 × 5	1024	4.48 × 4.48	7.8 %	1.56	- [3]	5	6.31	666	SSGC, 2.7 kg	[118]
2009	CdTe	0.055 × 0.055 × 1	65536	1.4 × 1.4	- [3]	0.16	- [3]	5	5.6	73	MediPROBE (Medipix2), 3.2 kg	[121]
2006	CZT	0.33 × 0.33 × 2	4096 (×8)	2.7 × 2.7 (×8)	10 %	- [2]	- [3]	- [2]	1.4	- [2]	SemiSPECT, at 5°C	[122]

[1] see text or ref. for collimator specifications; [2] not specified; [3] not applicable; [4] same detector of Digirad ergo®

CHAPTER

3

SILICON PHOTOMULTIPLIERS

More than seventy years after the discovery of the p-n junction, SiPMs are the latest advance of solid-state photodetectors, particularly for low light level detection, being able to detect single photons at room temperature with count rates of several hundred MHz. This is possible due to their high gain and photon detection efficiency, controllable noise levels and excellent timing properties. Other interesting features are the insensitivity to magnetic fields, low bias voltage and power consumption and small size. For these reasons, and despite not having yet achieved a fully mature development, these devices are already replacing the traditional PMTs in many low light level detection applications.

3.1 Working principle

The basic working principle of SiPMs has been briefly introduced in section 2.2.1, in the context of silicon photodetectors used for scintillation light readout in small FOV gamma cameras. Each SiPM is essentially an array of hundreds or thousands of identical G-APDs connected in parallel, which are the pixels of the SiPM. The schematics and photograph of a SiPM and its constituent pixel are shown in Figure 3.1.

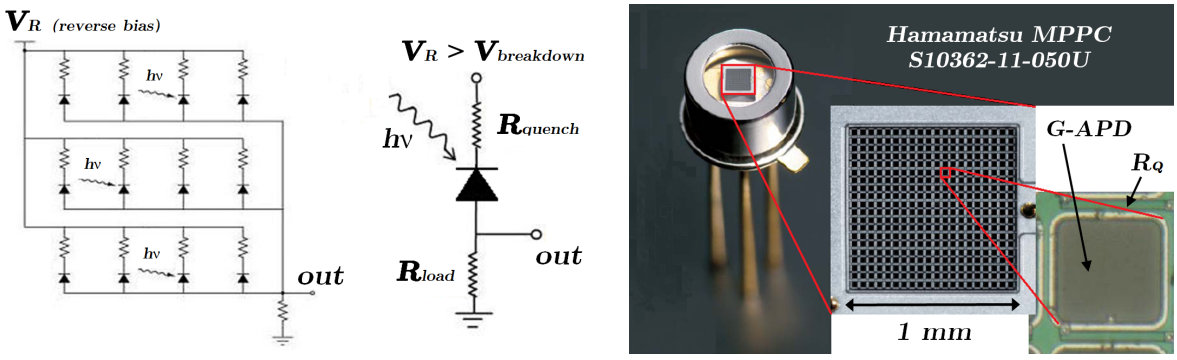

Figure 3.1: Equivalent circuit (left) and photo (right) of a Hamamatsu SiPM and its basic pixel: a G-APD with quenching resistor (adapted from [30]).

A photon absorbed in the pixel volume generates an electron-hole pair, and the generated charge carriers drift to the avalanche region where they can trigger a Geiger avalanche. Since G-APDs are biased above the breakdown voltage, the electric field at the p-n junction becomes so high that the avalanche process started by an accelerated charge carrier extends over the whole depletion layer and becomes self-sustainable, needing to be quenched, usually by a high-ohmic serial resistor (passive quenching) or by an active quenching

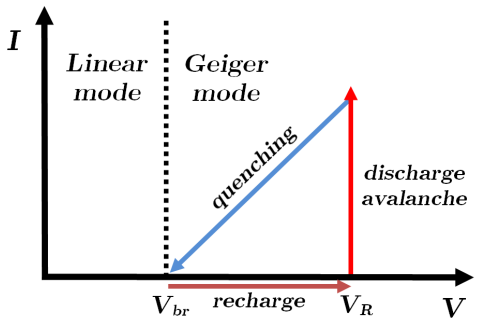

Figure 3.2: Schematics of G-APD operation.

circuit. The process is schematised in Figure 3.2. Before an avalanche, G-APDs are biased at V_R, a few V above the breakdown voltage (V_{br}). When a charge carrier (photon-generated or not) triggers an avalanche, current increases very rapidly by charge multiplication, but by flowing through the quenching resistor, it brings down the voltage back to V_{br} thus stopping the avalanche. The pixel then recovers to the initial state and is ready for a new avalanche. It is the possibility of maintaining the diode in supercritical state for sufficient times between avalanches, *i.e.*, to bias small p-n junction volumes above the breakdown voltage faster than on average a free electron is generated, that makes photon counting with SiPMs feasible.

An array of G-APDs overcomes the limitation of the single device, which is the fact that it is a binary device: it is either on or off. Each pixel cannot distinguish between a single photon and multiple photons arriving simultaneously, since the avalanche process results in a final pulse with constant amplitude. One knows there was at least one electron/hole initiating the avalanche, but not how many. Having an array of G-APDs connected in parallel provides an output signal which is the sum of the outputs of individual pixels. In this way, the output of the SiPM is proportional to the number of incident photons, given that the latter is lower than the total number of pixels. The output charge of the SiPM is given by

$$Q_{out} = C \times (V_R - V_{br}) \times N_{fired}, \tag{3.1}$$

where C is the pixel capacitance, which multiplied by the overvoltage gives the pixel charge. An example of a SiPM output signal as seen in an oscilloscope and corresponding pulse-height distribution obtained with a multi-channel analyser (MCA) or ADC, is shown in Figure 3.3. For this example, it can be inferred that the detected light is composed mainly of a few photons, resulting in a signal of mostly 1, 2 or 3 photon equivalent (p.e.) peaks. The first peak in the histogram corresponds to the electronic noise pedestal, which by coincidence is evenly spaced with respect to the other peaks.

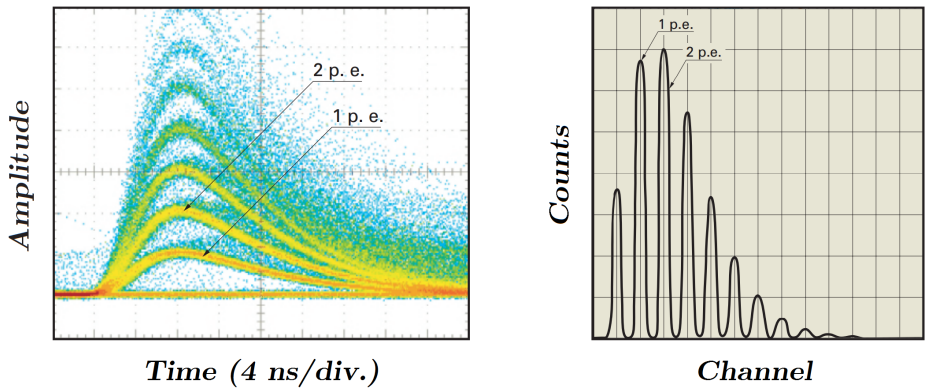

Figure 3.3: Example of a SiPM output signal (left) and corresponding pulse-height distribution (right) (adapted from [30]).

Historical development

The invention of the SiPM was precipitated by another invention which occurred in the 90's in Russia: the metal-resistor-semiconductor (MRS) APD [123], whose structure is represented in Figure 3.4. The MRS-APD has a very thin metal layer (Ti or Ni, 100-200 nm) and a high-resistivity layer of SiC or S_XO_Y, which quenches the Geiger avalanche by a local reduction of the electric field. The next step was logical and lead to the birth of the SiPM: the MRS structure was subdivided into many pixels and all of them were connected in parallel via an individual quenching resistor. The main scientists responsible for these developments were V. Golovin and Z. Sadygov [124, 125].

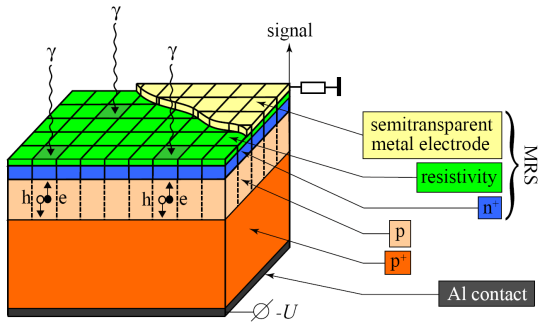

Figure 3.4: Structure of a MRS G-APD, the precursor of the SiPM [126].

3.2 Structure

The basic structure of a SiPM can be explained by a simplified description of its production. Firstly, a thin (2-4 μm) epitaxial layer is grown on a low resistivity Si wafer, usually with 300 μm. The next step is the diffusion of heavily doped Si into the epitaxial layer (with the same type of Si). The p-n junction is then formed about 0.5 μm below the surface by a shallow diffusion or ion implantation of the opposite dopant. Finally, an extremely thin but heavily

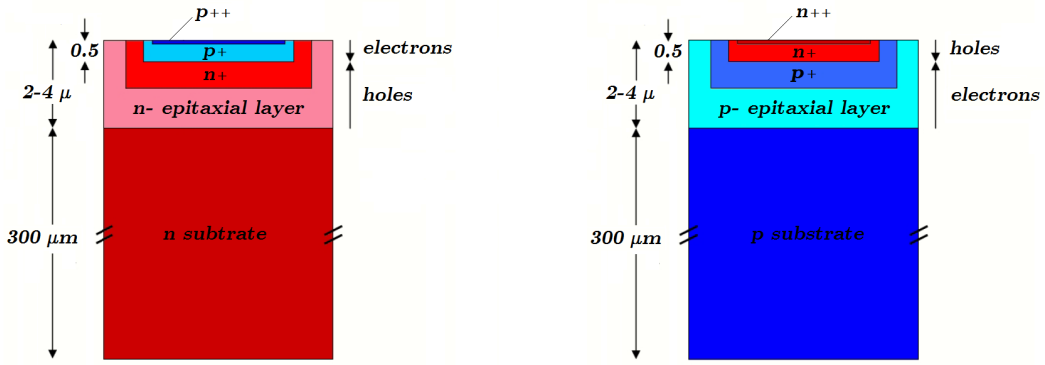

Figure 3.5: Schematic view of a SiPM pixel structure, predominantly blue-sensitive p-on-n (left) or red-sensitive n-on-p (right) [89].

doped layer (p++ or n++) is created on the surface, to enable a uniform distribution of the potential over the entire area of the photodiode [89]. The final structure is shown in Figure 3.5. Other production steps and details such as passivation of the surface with SiO_2 (for efficient light transmission to Si), creation of quenching resistors and metallic electrodes for charge collection, were omitted.

Depending on the types of Si used, two structures with different sensitivities can be created: p-on-n structure (type p on top of type n Si) and n-on-p structure (the opposite). The p-on-n structure will be preferentially sensitive to blue light, while the n-on-p will be more sensitive to red light. To understand why, one must consider the following:

- shorter wavelength photons are absorbed in a shorter Si distance than longer wavelength photons;
- electrons drift from the p to the n layer and holes from the n to the p layer;
- electrons have a lower impact ionisation threshold than holes: 1.75×10^5 V/cm versus 2.5×10^5 V/cm, which means they trigger avalanches with higher probability than holes.

It is therefore easy to conclude that, when the p layer is in the first fraction of μm (p-on-n structure), blue photons will have a higher photon detection efficiency (PDE) and, in the opposite situation (n-on-p structure), the peak PDE will be shifted to longer wavelengths.

3.2.1 Types of structures

Different SiPM configurations and structures are possible and new developments are intensively ongoing.

The first advanced design was published in 1998 [125] and is the structure of many commercial SiPMs available today, including Hamamatsu MPPC® used in this work. This design contains a matrix of independent p-n junctions (μ-cells) with individual surface resistors, separated from the Si wafer by a layer of SiO_2 (Figure 3.6 a)). The resistors are responsible for the quenching of the avalanche, discharging each cell in a common metallic grid. They

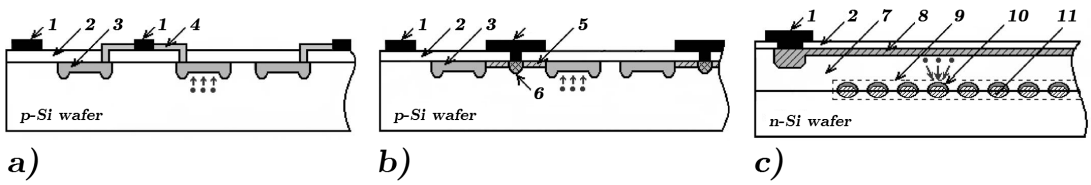

Figure 3.6: Schematics of different structures of SiPMs: a) with individual surface resistors; b) with surface drift channels; c) with deep micro-wells. Legend: 1–common metal electrode, 2–SiO_2 layer, 3–p-n junctions/μ-cells, 4–individual surface resistors, 5–individual surface channels, 6–drain region, 7–p-type Si epitaxial layer, 8–highly-doped p-type Si layer, 9–region with micro-wells, 10–local avalanche regions, 11–individual micro-wells (from [127]).

provide enough space between each μ-cell and the metal electrode to avoid short circuit, which was a problem in initial MRS SiPM designs, due to their thin resistive layer (100-200 nm). The individual polysilicon quenching resistor is not on top of the sensitive area but placed on the side (as can be seen in Figure 3.1), which increases the sensitivity to lower wavelength photons relatively to the MRS structure but, on the other hand, represents a loss of active area. Consequently, despite providing a high gain (10^6) and very good single photoelectron resolution, this structure has limited fill factor and dynamic range. The use of optical trenches or grooves between neighbouring pixels reduces the optical crosstalk, allowing a closer distance between pixels, therefore increasing the fill factor up to about 60-70% and maximum pixel density to $\sim$2000/mm^2.

Because the production of SiPMs with surface resistors requires special steps, not being compatible with modern CMOS technologies, structures without resistors have been developed, such as the SiPM with surface drift channels (Figure 3.6 b)). In this structure, instead of quenching resistors, there are surface channels through which charge carriers are transferred, along the Si substrate. These channels result from the formation of a very thin ($\sim$10 nm) n-type Si layer with a high resistance, in the space between the p-n junctions and the drain region, when a sufficient bias voltage is applied and avalanches are generated. This design also provides a high gain and very good single photoelectron resolution and has the advantage of being based on standard CMOS technology. The limitations are again related to the limited fill factor and dynamic range.

Although CMOS cannot create deep trenches between neighbouring pixels, it allows producing auxiliary circuits (*e.g.* for active quenching), which can reduce crosstalk effect, at the cost of a lower fill factor. Using the same standard CMOS production technology, readout circuitry can be placed right beside the p-n junctions, allowing the development of new configurations of SiPMs such as the digital SiPM introduced by Philips [128].

Another type of structure [129], shown in Figure 3.6 c), has the peculiarity of allowing an active area of 100% and high dynamic ranges of up to 40.000/mm^2. This design consists of a common p-n junction and a clear sensitive surface. The pixel individualisation is made not at the surface, but in depth, by the creation of micro-wells, placing vertical p-n-p-n structures inside of the Si substrate. These structures result in the development and subsequent self-quenching of the avalanche processes in independent micro-channels, due to opposite electric fields created by free charges collected in these channels. This design has the unique properties of allowing a very high pixel density and a very high linearity of response, with a geometrical transparency of 100%. The limitations are related to an inferior gain which is limited to about 7×10^4 and the more sophisticated production technology required.

Back illuminated SiPM structures are also being investigated [130, 131], in order to provide a higher sensitive area and thus, a higher PDE.

3.3 Properties

The main features of the SiPM can be summarised in the following points:

- High internal gain, up to 10^6-10^7;
- Low bias voltage (typically between 30-90 V) and power consumption (less than 50 μW/mm^2);
- High photon detection efficiency (percentage of incident photons that are detected), which can reach effective values up to almost 40%;
- Individual SiPM active areas between 1-25 mm^2;
- Ability to detect single photons at room temperature (despite better performance at lower temperatures);
- Noise in the form of dark counts, optical crosstalk between pixels and delayed pulses (afterpulsing);
- Fast response and recovery times (few ns);
- Insensitivity to magnetic fields;
- Small size and compactness.

3.3.1 Gain

The gain of a SiPM is defined as the number of charge carriers produced per photon absorbed. It is given theoretically by equation 3.2, *i.e.*, by dividing the output charge of a single pixel avalanche by the electron charge q:

$$G = \frac{C \times (V_R - V_{br})}{q}. \tag{3.2}$$

Larger pixel areas have a higher capacitance, therefore SiPMs of the same structure but with a lower number of pixels per mm^2 (*i.e.*, larger pixel area) will have a higher gain.

For a fixed temperature, the gain increases linearly with the overvoltage but, as the temperature rises, the gain for a fixed voltage decreases. This happens because the breakdown voltage of a Si photodiode increases with the temperature, due to the interactions of the carriers with phonons. To obtain a stable output, it is essential to keep the device at a constant temperature or, preferably, to adjust the reverse voltage according to the temperature (usually, a regulation of around 50 mV/°C is needed).

3.3.2 Photon detection efficiency

The PDE is defined as the percentage of incident photons which is really detected by the SiPM and it is the product of the geometric fill factor, the quantum efficiency of the sensitive area and the avalanche probability:

$$PDE = Fill\ factor \times QE(\lambda) \times Avalanche\ Probability. \tag{3.3}$$

This may be understood by the following sequence of events:

1. An incident photon either may or may not fall in the sensitive surface of the SiPM (a non-photosensitive surface area may exist, such as that occupied by quenching resistors or optical grooves around each pixel). The probability of a photon falling in the sensitive area is given by the ratio of sensitive to total area, denominated fill factor.

2. A photon falling in the sensitive area may or may not generate a charge carrier that reaches the high-field region, the probability of which is given by the quantum efficiency of the Si. This can be 80-90%, depending on the wavelength of the photon.

3. A photon-generated carrier traversing the high-field may or may not trigger an avalanche breakdown (there is a non-zero probability of not generating an avalanche).

In standard SiPMs, the fill factor has a trade-off relation with the pixel density. For the same sensitive area, a smaller number of larger pixels results in a higher fill factor, because there is less dead space due to individual quenching resistors and optical insulators. Therefore, the PDE increases for larger pixel sizes, *i.e.*, for lower pixel densities. This behaviour is visible in Figure 3.7, a graphic of the PDE variation with the wavelength of incident photons, for Hamamatsu MPPC® models with different pixel densities (100, 400 and 1600/mm^2).

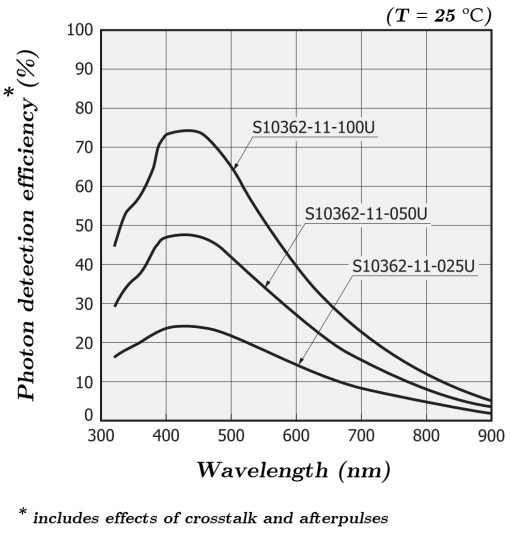

Figure 3.7: PDE of Hamamatsu MPPCs® [30].

The peak PDE is observed for a wavelength around 440 nm and, for the larger pixel device (10×10 pixels with 100 μm pitch), the reference value quoted by Hamamatsu is 65%. However, as specified in the figure's footnote, this manufacturer data includes effects of crosstalk and afterpulses (explained in section 3.3.4), which together account for about 35% of the output of this larger pixel model [132], therefore the real PDE is largely overestimated. Tadday *et al.* [133] determined a real peak PDE of about 37%, 32% and 19% for the three MPPC® models. This means that the measured absolute values are smaller than the peak PDE values given by the manufacturer by 43%, 36% and 24%, respectively.

3.3.3 Dynamic range and linearity

The dynamic range of a SiPM is determined by the total number of pixels: N pixels can detect a maximum of N simultaneous photons. Since each pixel can only detect if one or more photons hit it, the photon detection linearity decreases with the increase of the number of photons in relation to the total number of available pixels, because two or more photons start to hit the same pixel simultaneously. Therefore, the SiPM output signal is proportional to the number of incident photons, $N_{photons}$, as long as the number of photons in a pulse times the PDE is significantly smaller than the total number of pixels (N_{pixels}) [134]. Equation 3.4 describes this behaviour very well and Figure 3.8 shows the theoretical values for a SiPM with 100 pixels, considering two different PDE values. When the number of simultaneously incident photons times the PDE exceeds 50% of the total number of available pixels, the deviation from linearity is more than 20%.

$$N_{excited\,pixels} = N_{pixels} \times (1 - e^{-\frac{Nphotons \times PDE}{N_{total}}}) \tag{3.4}$$

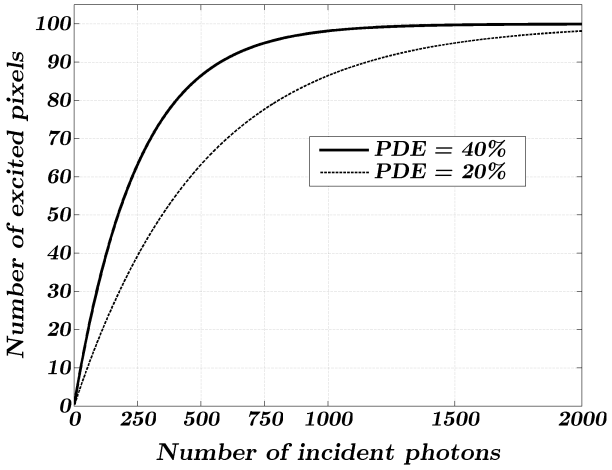

Figure 3.8: Theoretical values for the number of excited pixels as a function of the number of incident photons, in a 100-pixel SiPM with a PDE of 20 and 40%.

3.3.4 Noise

There are three contributing sources of noise in the SiPMs:

- Primary dark counts;
- Optical crosstalk;
- Afterpulsing.

Dark counts consist of spurious current pulses triggered by non photo-generated carriers. The main source is thermal excitation, but also the field-assisted generation of free electrons (electron tunnelling), in a smaller scale. Dark counts are defined as the number of dark pulses with a threshold at half of one photon amplitude (0.5 p.e.) and are usually expressed as a rate. Typical SiPM dark rates vary between 100 kHz and several MHz per mm^2 at 25°C. A random pixel dark pulse is equivalent to a single photon pulse, so it cannot be discriminated from an original photon detection signal. Moreover, dark counts can have amplitudes twice or several times higher than the amplitude of a single pixel breakdown, complicating the detection of low light levels. The effects of dark counts can be reduced by setting an appropriate threshold, below which signals are discarded. If the light levels to be measured are above the higher noise amplitudes, dark counts can be virtually eliminated with this method. If the time at which the light enters the SiPM is known, the effects of dark counts can be further reduced by setting a gate time for acquisition. The dark count rate is highly dependent on bias voltage and temperature, increasing with both.

Optical crosstalk is the excitation of neighbour pixels due to photon emission during an avalanche discharge in a given pixel. There are on average 3 photons emitted per 10^5 charge carriers produced in an avalanche, with energies above the Si bandgap, which means that each of these photons can trigger another avalanche in a neighbour pixel, like any other external photon. Crosstalk increases with the bias voltage and is higher for larger pixel sizes. This is explained by the higher gain of the larger pixel model, *i.e.*, for the same overvoltage, there are more charge carriers produced in a avalanche, so there is a corresponding increase in the number of photons produced. Operation at relatively low gain is advantageous to reduce crosstalk, but has the disadvantage of reducing the PDE. As mentioned in section 3.2.1, the design method to suppress or reduce crosstalk is to insert narrow grooves between cells and fill them with an optical absorber.

Afterpulses consist of secondary current pulses caused by carrier trapping and delayed release (several hundred ns after the primary event), due to traps formed in the breakdown volume of the Si (crystal defects). Similarly to optical crosstalk, afterpulsing adds fake counts to the optical signal measurement and, if not taken into account, leads to an overestimation of the PDE. Afterpulsing probability is a function of the trapping centre de-excitation time,

which depends mainly on the temperature. At lower temperatures [135], this time increases, so the trapped carrier is released with a longer delay, resulting in a higher probability of afterpulsing. At room temperature, de-excitation time is shorter, so afterpulsing probability is lower because most trapped carriers are emitted while the diode is still recovering from the primary avalanche and therefore their contribution is less significant.

3.4 Experimental measurements

Since only about 10-15 photons are expected at the fibre ends of the WSF gamma camera, the larger pixel SiPM model was chosen, which has the highest PDE and gain, favouring fill factor over dynamic range and thus being the most appropriate for the detection of a very low number of photons.

However, for such low light level detection applications, the intrinsic dark count rate may be a critical performance drawback of SiPMs. Depending on the charge integration time required, and on the dark pulse rate of the SiPM, the dark pulse signal may be equivalent to multiple photo-electron pulses and, for gated applications, this may severely impact the usability of this device in low light level detection.

Experimental measurements were performed in order to evaluate the dark noise characteristics of the chosen SiPM and its variation with bias voltage and temperature, for different noise-suppressing threshold values. In this work, dark counts refer to the overall contribution from the three sources of dark noise mentioned above.

3.4.1 Setup

Photon-counting spectra of SiPM devices have been obtained using Hamamatsu MPPC® S10362-11-100U and characterised in terms of their background noise. The dark rates and their variation with temperature and bias voltage were measured in a dark chamber specially built for this purpose, as schematised in Figure 3.9. An Ortec 710 power supply was used to bias the SiPM. The SiPM output was initially amplified with a linear amplifier (Canberra

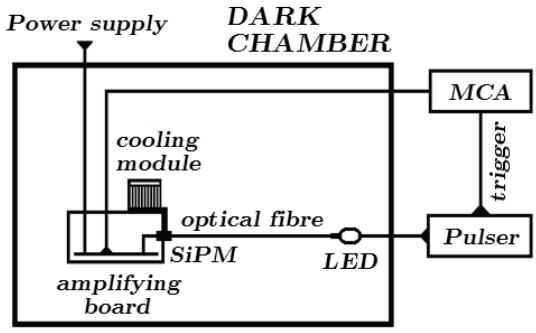

Figure 3.9: Simplified schematics of the experimental setup.

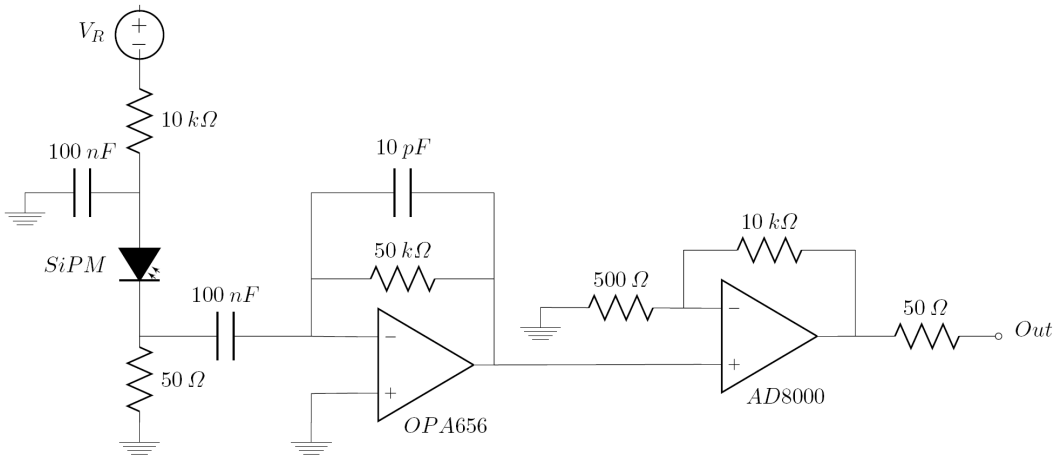

Figure 3.10: Front-end electronic circuit developed for SiPM readout.

2111) with no shaping and fed into a peak sensing ADC (Amptek MCA8000A). This was later replaced by a custom amplifying circuit (Figure 3.10) which was developed and included inside the dark chamber, providing similar results. Because this circuit inverts the signal, the polarity of SiPM bias voltage was inverted, in order to obtain a positive output signal. To study the variation of the dark rate with temperature, a cooling module was set up, consisting of a thermoelectric Peltier module with a heat-sink and extracting fan, controlled with a thermocouple.

Measurements were also taken with low light levels. A high resolution pulse generator (BNC PB-5) was used to illuminate a 470 nm LED and also to trigger the ADC gate for signal acquisition from the SiPM. A BCF-91A wavelength shifting optical fibre was used between the LED and the SiPM.

3.4.2 Results

The following experimental results were obtained using the initial amplifying scheme. The dark rates for different bias voltage values were measured at room temperature and are shown in Figure 3.12, where it is clearly visible the dependence with bias voltage and with detection threshold, as expected.

Results of the dark rate variation with temperature, for different threshold values, are also presented, where no light source was used. It is seen that the dark rate (at a threshold of 0.5 p.e.) becomes approximately half at every 8-9°C. The photoelectron pulse-height spectrum for one of the test conditions is shown in Figure 3.11.

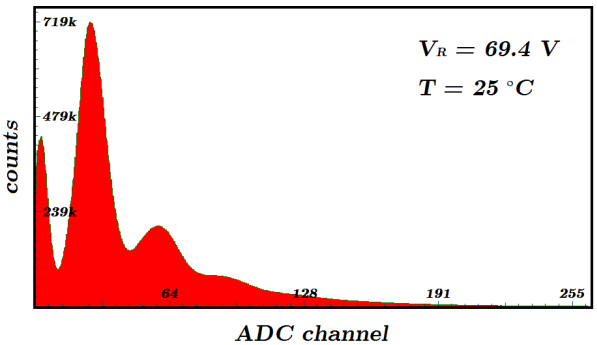

Figure 3.11: SiPM dark pulses spectrum.

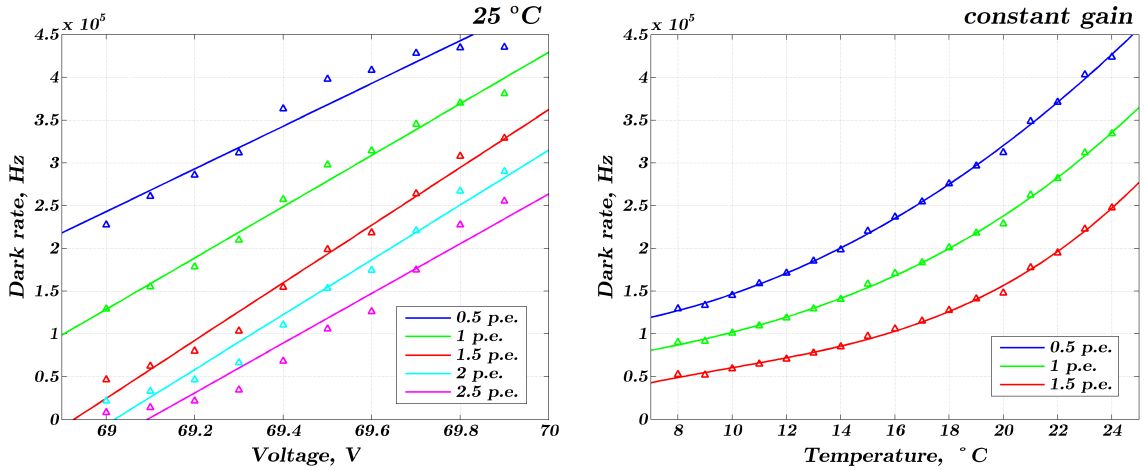

Figure 3.12: SiPM dark rate as a function of bias voltage (left) and temperature (right).

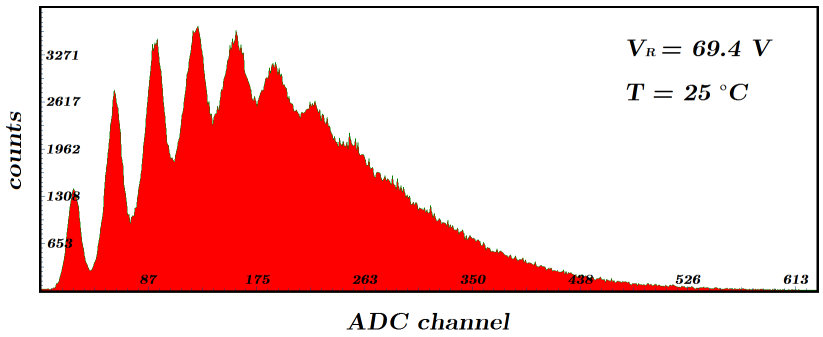

Figure 3.13: SiPM low light response spectrum.

The single electron peak is clearly visible (highest peak), and so are the 2^{nd} and even 3^{rd} electron peaks, corresponding to multiple simultaneous dark pulses within the device.

The ADC spectrum of the time gated signal obtained with the pulsed LED coupled to an optical fibre is shown in Figure 3.13. The high photoelectron resolution of the SiPM allows a clear separation of several electron peaks. It can be seen that for very low light levels, the single electron peak coincides with the dark pulse shown above.

3.5 Simulation of the impact of dark counts in low-light level SiPM multi-readout applications

The SiPM charge signal from primary photoelectrons follows an approximate Poisson distribution:

$$p(x,\lambda) = \frac{e^{-\lambda} \times \lambda^x}{x!}, \quad x \in \mathbb{N}_0, \tag{3.5}$$

where λ represents the average number of photoelectrons per event, in a given time interval.

However, due to variations in the charge amplification process and other events such as small differences between pixels or photon interactions in recharging pixels, Gaussian spreads are introduced in the signals collected [136]. Therefore, the expected SiPM charge spectrum is a Poisson distribution convoluted with Gaussian distributions, *i.e.*, the number of photoelectrons in each event is given by a Gaussian function

$$g(x) = \frac{1}{\sigma\sqrt{2\pi}} e^{-\frac{(x-\mu)^2}{2\sigma^2}}, \tag{3.6}$$

with mean (μ) given by Poisson function $p(x, \lambda)$ (equation 3.5) and standard deviation σ.

A MatLab® application was developed to simulate SiPM charge signals, for a given Poisson mean λ and Gaussian standard deviation σ, ignoring counts below a given threshold value. The values of λ and σ were taken from experimental data of the 100-pixel SiPM dark counts, for different conditions of temperature, bias voltage and charge integration time. The value of λ was found to vary approximately between 0.2 and 0.75 and σ between 0.25 and 0.3. As shown in Figure 3.14, the simulated spectrum shows a good agreement with the acquired one, considering that simulation ignores the electronic noise.

3.5.1 Simulated setup and conditions

To test a detection apparatus of 120 per 120 SiPMs triggered by a common gate, the application simulates 120 per 120 SiPM charge spectra acquired simultaneously, where 5 of the SiPMs in each direction have a low light signal, *i.e.*, have a higher Poisson mean than the average for dark noise. The configuration may consist of an inorganic scintillation crystal coupled to two orthogonal layers of 120 wavelength-shifting fibres, each of which read out by a SiPM, *i.e.*, the WSF gamma camera. For the purpose of this study, the light levels reaching the SiPM were considered to be 10 photons in the central fibre, 6 in the two neighbour fibres and 2 in the next surrounding ones, simulating the approximate light levels expected with

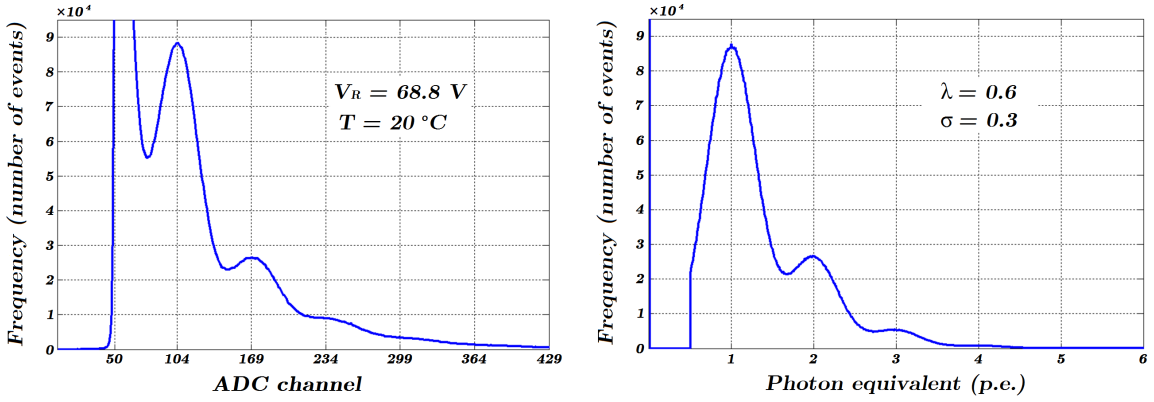

Figure 3.14: Acquired (left) and simulated (right) spectra of SiPM dark pulses.

the WSF gamma camera for a pencil beam of 140 keV γ-rays perpendicularly directed at the centre of one of the large surfaces of the crystal (according to previous studies mentioned in 1.4.2). The position of the central fibre was defined as (x=10, y=10), so as to evaluate the imaging performance in a non-central position. 5000 counts (events) were simulated. Table 3.1 summarises the parameters used in the simulation.

Table 3.1: Conditions used in the simulation of SiPM dark noise impact.

Parameter	**Simulated values**
Number of events	5000
λ	0.3, 0.5, 0.7
σ	0.25
Threshold	0.5, 1, 2, 3, 4
Position of the central fibre	(x=10, y=10)
Number of photons in the 5 fibres	10, 6, 2
Photon detection efficiency (PDE)	20, 30, 40, 50%

3.5.2 Positioning algorithms

Three position detection algorithms were used:

$$Centroid_A = \frac{\sum_{i=1}^{120}(i \times q_i)}{\sum_{i=1}^{120} q_i}, \tag{3.7}$$

where q_i is the charge signal of the ith SiPM (centre of mass algorithm).

$$Centroid_B = i, \tag{3.8}$$

where i is the SiPM with maximum charge signal.

$$Centroid_C = \frac{\sum_{i=1}^{3}(i \times q_i)}{\sum_{i=1}^{3} q_i}, \tag{3.9}$$

for the 3 neighbour signals which sum is maximum.

The centroids in x and y directions were used to generate 2D images, as exemplified in Figure 3.15. A figure of merit, "imaging efficiency" (I_{ef}), was created to evaluate the performance of positioning algorithms, being defined as the ratio between the number of 2D centroids within a certain set of image pixels and the total number of events:

$$I_{ef} = \frac{number\ of\ (x,y)\ centroids\ within\ a\ set\ of\ pixels}{total\ number\ of\ events}. \tag{3.10}$$

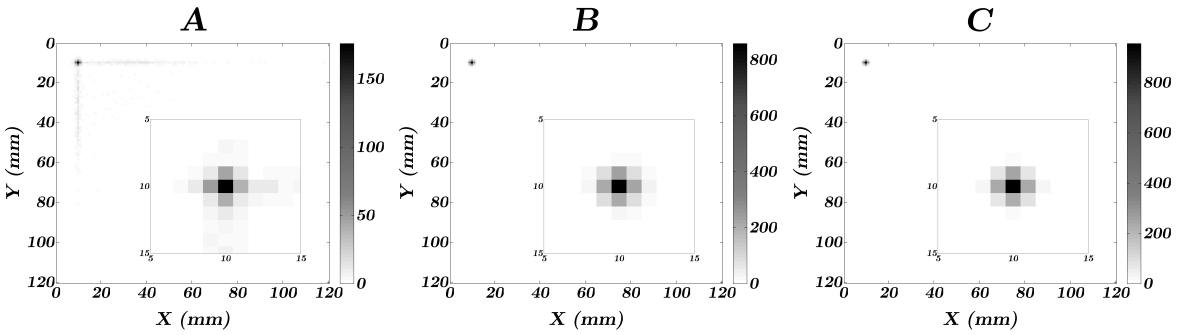

Figure 3.15: Example of 120×120 mm^2 simulation images obtained with 3 position algorithms, for PDE=30%, λ=0.5, σ=0.25, threshold=3 p.e., central fibre in $x = 10$, $y = 10$ (with 10×10 mm^2 zoomed area around this point).

Imaging efficiency was determined for different sets of image pixels, shown in Figure 3.16, considering different values of PDE, λ and threshold. Even though pixel size is limited to 1 mm^2 only by algorithm B (not by A or C), this pixel size was used for all images. Thresholds were defined to allow ignoring low signals from certain fibres.

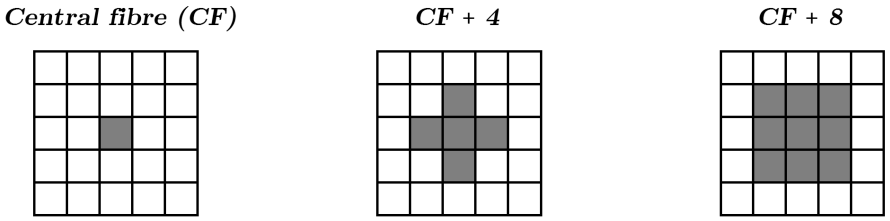

Figure 3.16: Sets of 1 mm^2 pixels used to calculate imaging efficiency (I_{ef}).

3.5.3 Results

The values of I_{ef} obtained for the three algorithms in the simulated conditions are presented in Figure 3.17.

The reverse analysis was carried out, calculating the radius around the central fibre within which 76% of events fall, as shown in Figure 3.18. This radius gives an idea of how accurately the point source is being imaged by the different algorithms, for the simulated conditions, with smaller radius meaning a higher positioning accuracy. The percentage level was chosen because it represents the theoretical percentage for 2.35σ of a Gaussian distribution, *i.e.*, its FWHM. Therefore, the radius provides an approximation to the spatial resolution, given that the image represents the position of the point source accurately.

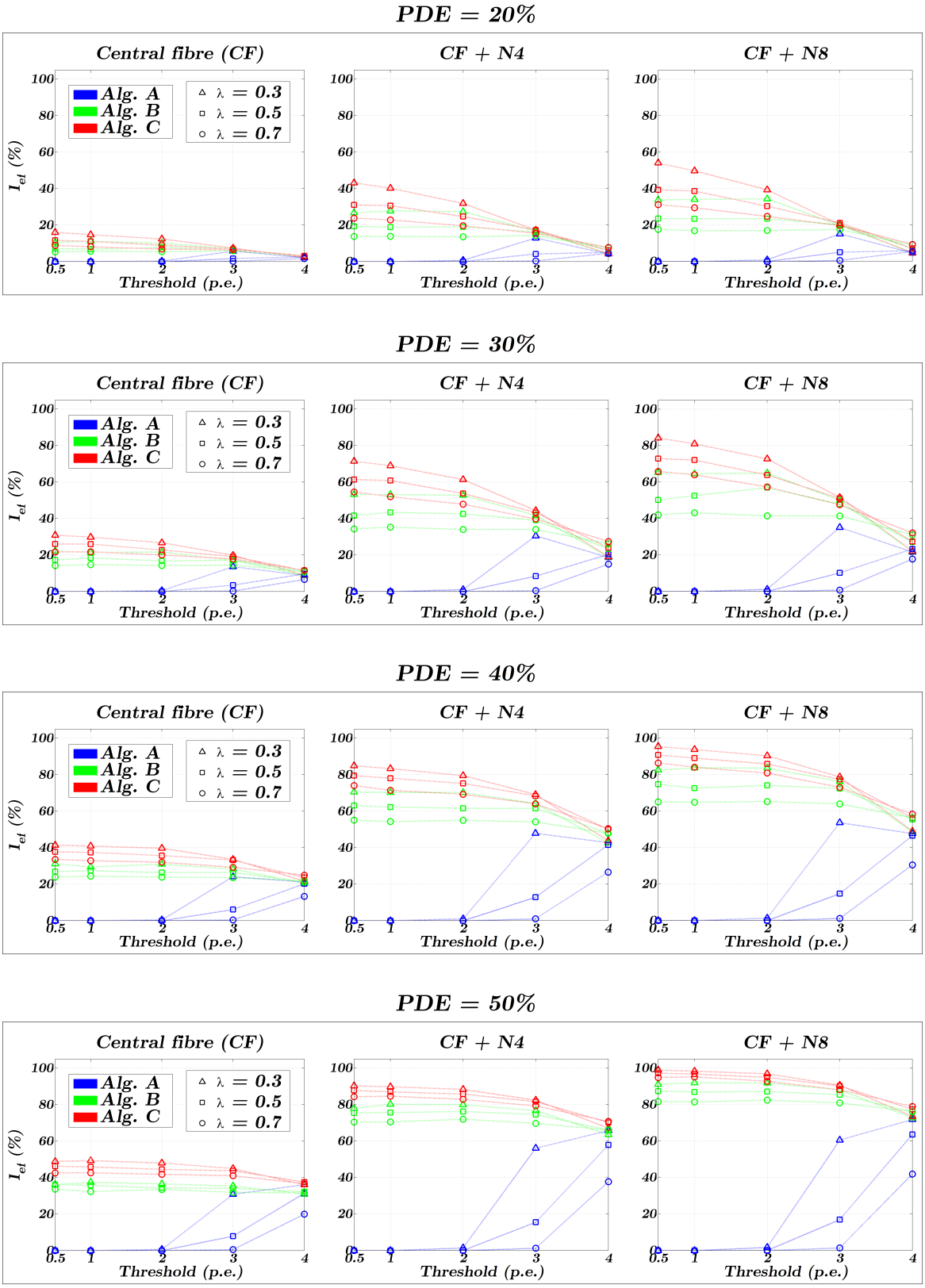

Figure 3.17: Imaging efficiency vs. threshold, for different SiPM noise levels and PDEs.

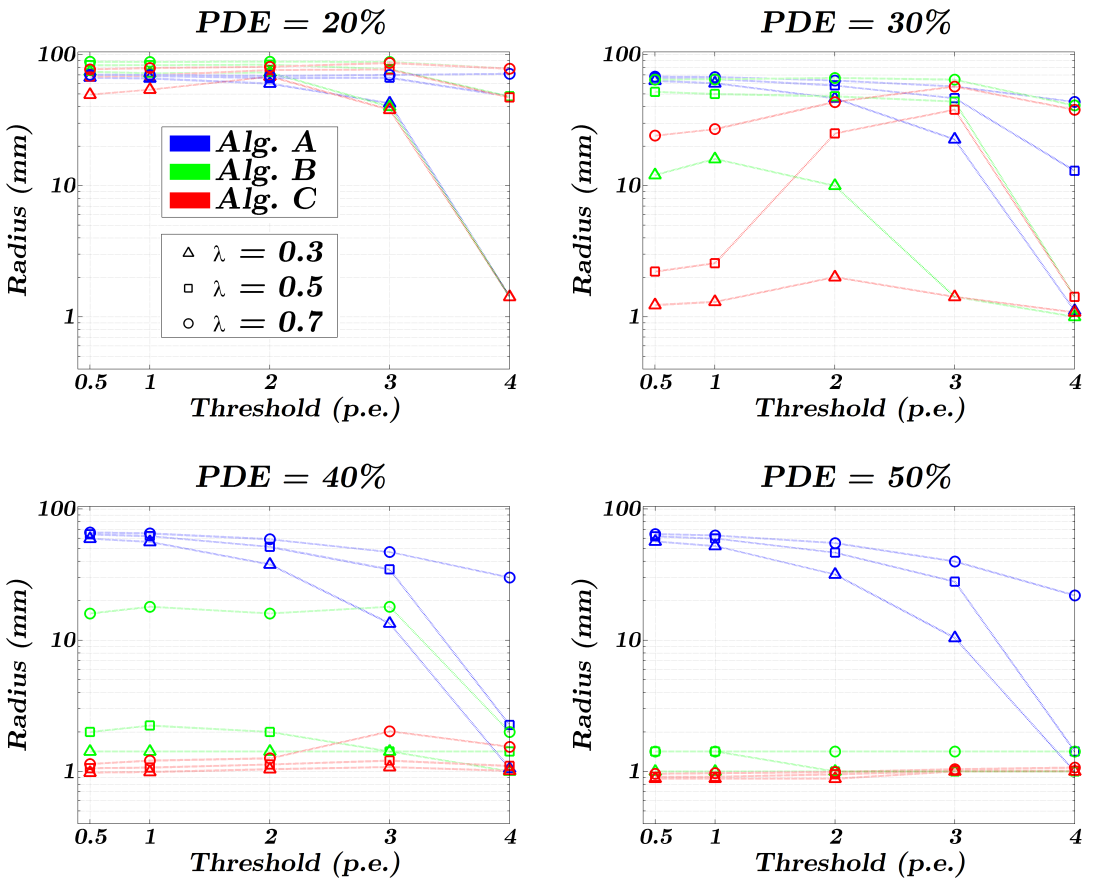

Figure 3.18: Radius around (x,y)=(10,10) where 76% of events above threshold fall inside.

3.6 Discussion and conclusions

The configuration of a WSF gamma camera was simulated, where 240 SiPMs are used to read out WSFs coupled to a scintillation crystal. In this kind of configuration, the light levels at the end of the fibres are expected to be in the order of only a few photons for γ-rays in the range of 80 to 200 keV, so the SiPM is a very interesting readout device due to its excellent photon counting capability. On the other hand, the SiPM has a high dark count rate of a few hundred kHz at room temperature, with amplitudes sometimes as high as 4 or 5 p.e. so it is of great importance to discriminate this random noise from the low light signals, in order to accurately position the light source. In applications such as the WSF gamma camera, where the pulse integration time is dependent on the decay time of a slow scintillation counter, the longer the signal integration the higher the probability of dark counts during the integration period, and this can be critical for detecting a very low number of photons in that period. For higher light levels, effects of dark counts can be reduced by setting an appropriate threshold.

The simple Monte Carlo simulation allowed evaluating the impact of the simultaneously acquired dark counts into position detection algorithms and results show that an image with good resolution can be obtained, despite the very low light levels. Of the three algorithms

tested, algorithm C shows the best results for low light level centroiding, indicating that a sub-millimetric spatial resolution is possible for a PDE of 40% or more, as suggested by the results in Figure 3.18. Considering the more realistic 30% PDE at 500 nm of the chosen SiPM (Hamamatsu MPPC® S10362-11-100U), results indicate that a spatial resolution around 1 mm FWHM is achievable, as long as the noise level is not high. From the results obtained, it is clear that algorithm A is not well suited for a low-light level application such as the WSF gamma camera, since it does not provide accurate positioning, particularly for events closer to the edges, where this algorithm tends to shift the centroid position towards the centre. This explains the much larger radius values observed in Figure 3.18. Only for thresholds above 3 does algorithm A produce more accurate images and leads to relatively high efficiencies, but even then it exhibits a higher vulnerability to changes in dark noise. On the contrary, algorithms B and C show good performance for lower threshold values, which favour imaging efficiency. This happens because these algorithms rely on maximum values. For this reason, they are also less sensitive to variations in the dark noise average, particularly for higher PDEs.

From the results of the experimental measurements (shown in Figure 3.12), it is evident that stability of bias voltage and temperature is crucial for good signal stability and dark rate control of each individual SiPM. Cooling the SiPM significantly reduces the dark counts approximately by half at every 8-9°C. Furthermore, decreasing the temperature at a constant bias voltage has also the effect of increasing gain and PDE, because it lowers the breakdown voltage. The bias voltage has a great influence in SiPM performance parameters, namely in gain, noise and PDE, all of which increase with it. It is therefore very important for signal stability that bias voltage and temperature are kept constant and, in order to reduce noise, that temperature is minimised and bias voltage is at a desirable level reachable through a compromise between maximisation of gain and PDE and minimisation of noise.

CHAPTER

4

THE SIPM WAVELENGTH-SHIFTING FIBRE GAMMA CAMERA

The main working principle and constituent parts of the WSF gamma camera have already been introduced and discussed in chapter 1, section 1.4. For the sake of clarity and readability, the schematics of the design is reproduced here, in Figure 4.1, for the specific case of using CsI(Na) as scintillator crystal and SiPMs as photodetectors reading out the WSFs.

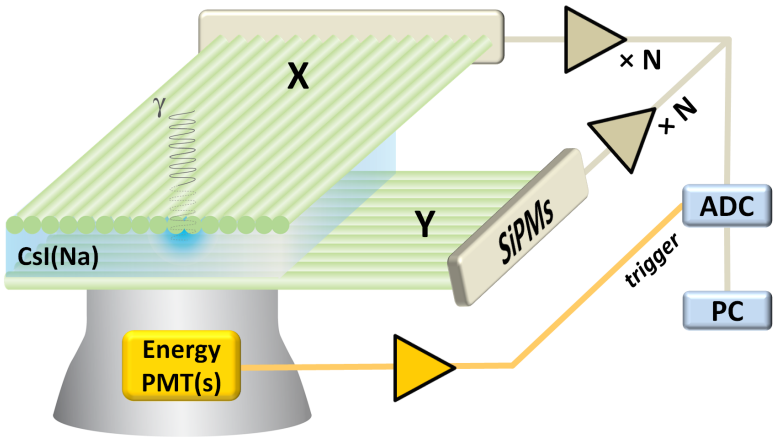

Figure 4.1: Schematics of the SiPM wavelength-shifting fibre gamma camera.

In this chapter, the development of a small SiPM WSF gamma camera is reported, including the assembly of the photon detection elements, development of customised readout electronics and software and final integration of all components in a prototype with a 50×50 mm^2 total area, but instrumented only in a 10×10 mm^2 imaging FOV. Imaging studies were performed with ^{57}Co for evaluation and characterisation of the intrinsic performance of the camera, initially using 10 SiPMs in one-dimensional scans and posteriorly with 10+10 channels in true 2D image acquisitions.

4.1 Assembly of photon detection components

In order to provide the best coupling of the WSFs to the scintillator, while preventing CsI(Na) degradation over time due to its slight hygroscopicity, a custom order was made to Hilger

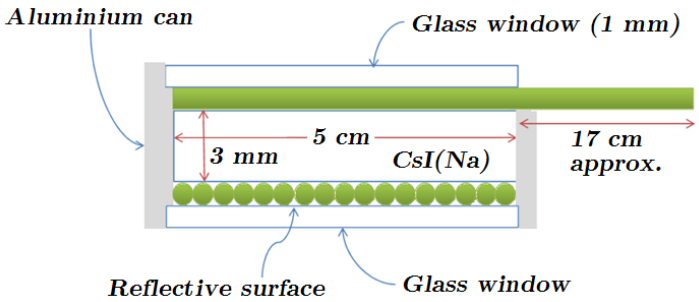

Figure 4.2: Schematics of the CsI(Na) crystal with embedded WSFs used in the small gamma camera prototype.

Crystals (UK) to assemble a 50×50×3 mm^3 crystal coupled to 50 orthogonally disposed WSFs on each side and then encapsulated in an aluminium can, with a glass window on both sides, as schematised in Figure 4.2. In this way, fibres are in direct contact with the scintillator surface and coupling conditions are kept constant. Even though a 3 mm thickness of CsI(Na) absorbs about 70% of 140 keV γ-rays (as mentioned in section 1.4.1), it provides a photoelectric absorption efficiency of 54% [53], *i.e.* 54% of the 140 keV photons deposit their full energy in the crystal. A white epoxy was applied to the inside surface of one of the glass windows, in order to reflect as much scintillation light as possible, to the fibres and to the energy PMT (Hamamatsu R2154-02), which was optically coupled to the other glass window using a silicone optical grease with n=1.465 (Saint-Gobain Crystals BC-630).

The fibres are blue-to-green WSFs (Saint Gobain Crystals BCF-91A), chosen for the good match between their absorption spectrum and the emission spectrum of the CsI(Na) crystal used, which has a peak emission at 420 nm, corresponding to the maximum absorption region of the WSFs (Figure 1.11, page 27). These multi-cladded round fibres have a minimum trapping efficiency of 5.6% for 420 nm and emission peak at 494 nm [48]. After being cut with a length of 22 cm, fibres were carefully polished on both ends and one end was aluminised by thermal evaporation. Aluminisation has been shown to slightly improve light ouput on the opposite fibre end [46]. The coupling of each 1 mm diameter fibre to a 1 mm^2 metal-packaged SiPM (Hamamatsu MPPC® S10362-11-100U) was done by simple contact with optical grease, using a custom designed plastic part whose function was to align the centre of each fibre with the centre of the active surface of the corresponding SiPM.

4.1.1 Readout electronics

A dedicated front-end electronics system was developed for the individual readout of SiPMs coupled to the WSFs, consisting of three stages (Figure 4.3). The first is a charge preamplifier stage using an OPA656 operational amplifier, followed by an amplifying stage with AD8000

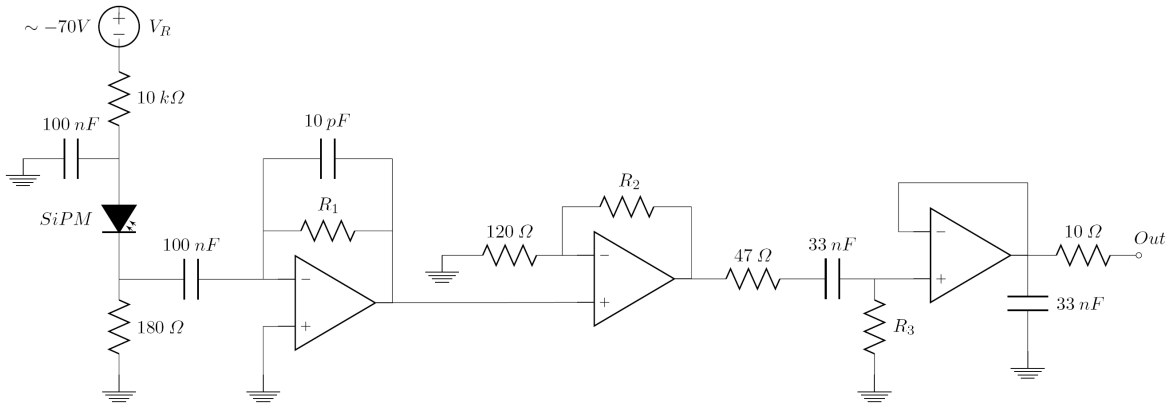

Figure 4.3: Readout circuit developed for the SiPMs in the CsI(Na) WSF gamma camera.

and a third final stage of CR-RC shaping, again using OPA656. This circuit is essentially the same used before for SiPM readout and dark rate characterisation (Figure 3.10), but further customised for the readout of CsI(Na) scintillation light transmitted by the WSFs. The energy PMT (E-PMT) signal is read out through a 2-stage charge preamplifier and amplifier circuit. After amplification, the signal is connected to a comparator circuit, to generate a NIM logic signal (trigger) required by a CAEN V785 peak-sensing ADC to start digitisation. In NIM logic, a voltage of 0 V corresponds to logic 0 and a current of -16 mA into a 50 Ω resistor (equivalent to ∼-800 mV) corresponds to logic 1. In order to have the SiPM pulse rise time within the time window used for ADC acquisition while keeping a pulse integration time long enough to include a large part of the relatively slow CsI(Na) scintillation decay, the SiPM signal was integrated and shaped, with a rise time of nearly 1 μs (Figure 4.4).

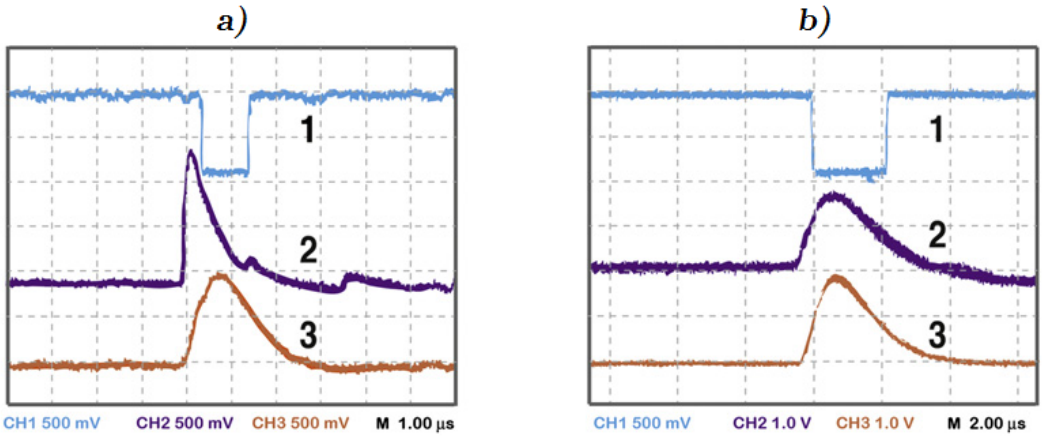

Figure 4.4: Oscilloscope snapshots when testing different SiPM readout circuits with a LED. Legend: 1-NIM logic signal required for ADC acquisition, 2-SiPM, 3-E-PMT; a) with initial RC=510 ns and no final shaping; b) with initial RC=100 μs and 4:1 CR-RC shaping.

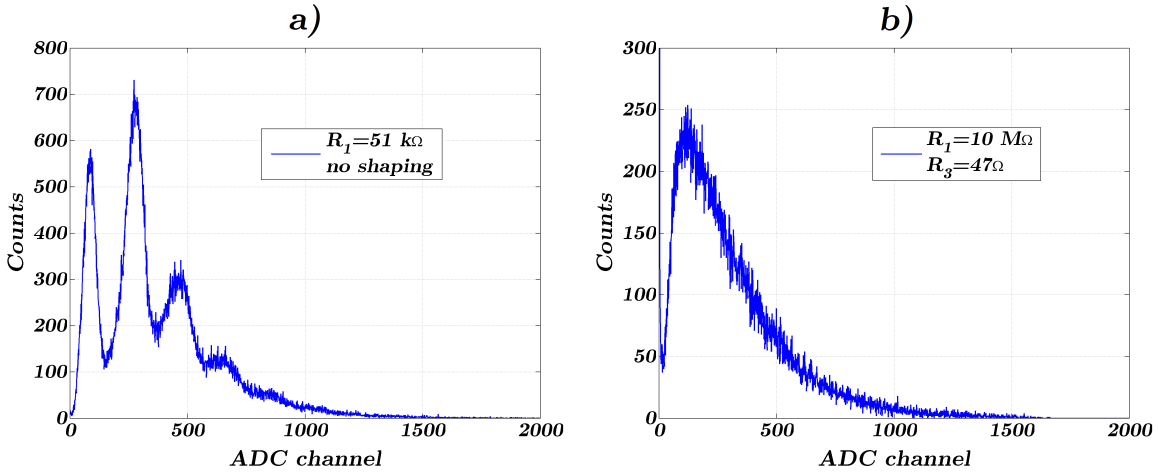

Figure 4.5: Influence of pulse shaping and integration time of SiPM signal on the resulting spectrum when reading out collimated ^{57}Co CsI(Na) scintillation light in a WSF; a) with initial RC=510 ns and no final shaping; b) with initial RC=100 μs and 4:1 CR-RC shaping.

Signal integration and shaping affect the resulting ADC spectrum, as depicted in Figure 4.5. For a SiPM signal readout using a small RC constant in the first pre-amplifying stage and without final stage of CR-RC shaping, the photon equivalent (p.e.) peaks can be observed in the spectrum, but integration time is too short and the signal reaches its peak before the leading edge of the digitisation gate created by the energy PMT signal. With a larger initial RC and a final CR-RC shaping, the signal becomes synchronised with the gate as it is required for proper digitisation, but the resulting spectrum acquires a different shape, where no p.e. peaks are visible. In this case, information of number of photons per event is lost and the pulse-height spectrum is no longer well approximated by a convolution of Poisson and Gaussian distributions (equation 3.6).

A final configuration was defined for application in the SiPM WSF gamma camera prototype, after testing different combinations of pulse processing circuits. This was done mainly by changing the values of R_1, R_2 and R_3 (in the circuit of Figure 4.3), and evaluating the impact of this change in the detection of light from a WSF aligned with a collimated source of ^{57}Co placed over the CsI(Na) crystal, while maintaining all the other experimental conditions.

The charge-sensitive preamplifier (first stage of the readout circuit) integrates the SiPM output charge Q on the feedback capacitor C_f, delivering an output voltage of

$$V_o \approxeq -\frac{Q}{C_f}. \tag{4.1}$$

Changing the feedback resistor R_1 of this first stage modifies the decay time constant τ of its output, which is given by

$$\tau = C_f \times R_1. \tag{4.2}$$

A large value of R_1 is necessary when the CR-RC shaping stage is used, because the latter requires an input pulse with a long tail (ideally a step function).

R_2 is the feedback resistor of the second stage non-inverting amplifier and modifying its value allows adjusting the amplification gain G, given by

$$G = 1 + \frac{R_2}{R}, \tag{4.3}$$

where R is the resistor between ground and the negative input of the operational amplifier.

Changing the differentiator resistor R_3 in the final shaping stage allowed testing different CR-RC time constants (τ_1 and τ_2, respectively), which influence the shape (amplitude, rise and fall times) of the final output pulse, as given by equation 4.4 for a step voltage input signal. Plots of this response for different combinations of τ_1 and τ_2 are shown in Figure 4.6.

$$A_{out} = \frac{A\tau_1}{\tau 1 - \tau 2}(e^{-\frac{t}{\tau 1}} - e^{-\frac{t}{\tau 2}}) \tag{4.4}$$

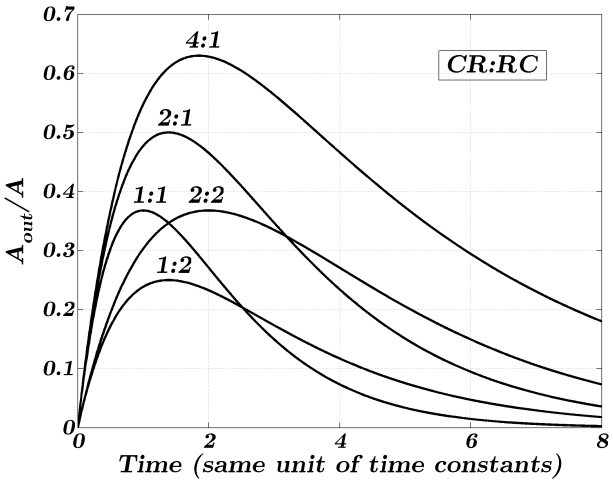

Figure 4.6: The response of a CR-RC shaping stage to a step voltage input of amplitude A, for five different pairs of differentiator:integrator time constants (adapted from [47]).

For each circuit tested, the difference between the SiPM spectrum when coupled to a WSF aligned with a collimated ^{57}Co source and the dark noise spectrum in the same conditions, was measured. Collimation was accomplished by a 6 mm Pb sheet with a 1 mm diameter hole, which was aligned with one of the top WSFs.

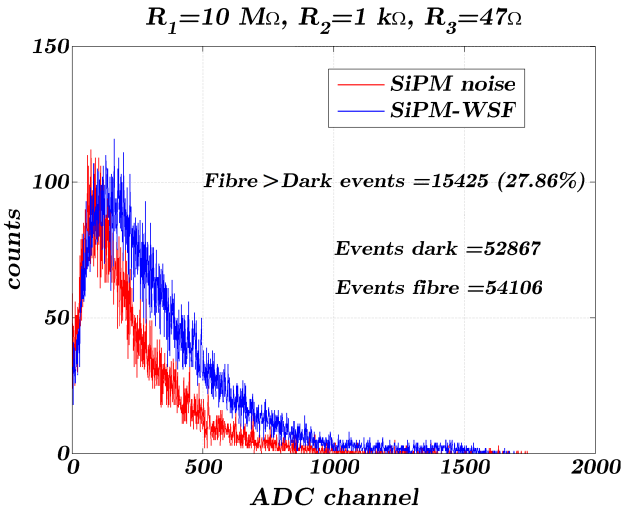

Figure 4.7: Spectra of dark and WSF signals within ±15% energy window, for a tested circuit.

Only events within a ±15% (30%) energy window around the 122 keV peak were considered. The percentage of events in the WSF-SiPM spectrum which were above the dark noise level obtained with the same circuit, is presented in Table 4.1 for several circuits tested and taking into account the slightly different number of events in the two spectra. Other resistor combinations were tested, but with unsatisfactory results (*e.g.* too short rise time, too much electronic noise, etc.), for which they are not presented. Measurements were performed at 22°C, with the SiPM biased at V_R=-70.4 V ($I_{supply} \sim 0.5$ μA). The same fibre and SiPM were used, so as to maintain coupling conditions. E-PMT was biased at -1000 V. Values are averaged from three acquisitions of 100.000 events for each circuit.

As can be seen from the results, the alteration of the resistors, particularly R_1 and R_3, has a significant impact on the discrimination of the signal of the scintillation light piped through

Table 4.1: Percentage of events in SiPM-WSF spectrum which are above SiPM dark noise, for different readout circuits tested.

$\mathbf{R_1}$ (Ω)	$\mathbf{R_3}$ (Ω)	**Percentage** (%)
10 k	180	14.67
51 k	22	13.77
51 k	47	17.28
51 k	100	24.65
500 k	100	22.42
500 k	180	14.67
1.5 M	47	24.19
10 M	47	26.59

the WSF from the intrinsic dark noise signal of the SiPM. Best results were observed for R_1=10 MΩ (τ=100 μs) and R_3=47 Ω (~4:1 CR-RC shaping), with the corresponding spectra shown in Figure 4.7. Even though the spectra do not show the p.e. peaks and thus differ from the SiPM spectra previously simulated (section 3.5), since this circuit was the one that produced the best experimental results in the camera's setup, it was used in the following tests and reproduced for all channels of the SiPM WSF gamma camera prototype.

4.1.2 Temperature influence

The effect of reducing the operating temperature of a SiPM reading out a WSF while using ^{57}Co was checked. The ambient temperature was controlled through an air conditioning system in a closed room. The gain was kept approximately constant for all measurements,

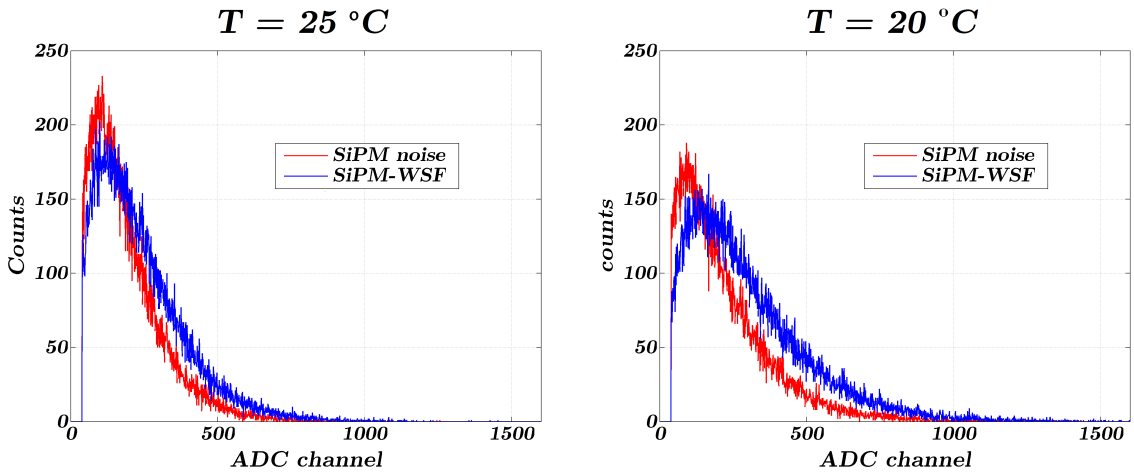

Figure 4.8: Influence of the SiPM operating temperature on the resulting spectrum and SNR when reading out collimated ^{57}Co CsI(Na) scintillation light in a WSF.

while the temperature was varied. The influence of the temperature on the resulting SiPM spectrum is clearly visible, even for a 5 °C difference (Figure 4.8). Decreasing the temperature increases the difference between the SiPM dark noise and its output when coupled to the WSF, thus allowing a better efficiency in the detection of the scintillation light retained in the fibre. For a reduction of 25 to 20 °C, the measured percentage improvement in the number of events above dark noise was more than 30%. A higher SNR in the detection of scintillation light from the fibres will have positive effects in the quality of the resulting image, namely a better contrast and spatial resolution, therefore a low operating temperature is desirable.

4.2 Imaging with ^{57}Co

A ^{57}Co source (E_γ=122.06 keV, $T_{1/2}$=271.79 d) was used for calibration and characterisation of the intrinsic performance of the SiPM WSF gamma camera prototype. The source is composed of a 5 mm diameter, 7 μm thick rhodium disk, with an estimated activity of a few hundred μCi at the time of the studies. Lead collimation was used for all acquisitions to produce a collimated beam, by drilling a 1 mm diameter hole in lead.

4.2.1 Energy resolution

Energy resolution at 122 keV was measured for the 3 mm thick CsI(Na) crystal encapsulated with embedded WSFs and for a CsI(Na) crystal of identical dimensions but encapsulated without fibres. This allowed evaluating not only the energy resolution of the system but also the impact of introducing WSFs between the crystal and the E-PMT. Tests were performed at different PMT supply voltages and the optimal voltage for Hamamatsu R2154-02 PMT was found to be around -1000−1100 V, using the readout circuit developed for the E-PMT. The 51 mm diameter tube was coupled with optical grease to the 50×50 mm^2 square crystal (plus 5 mm on each side with the encapsulation) using a plastic coupler designed to align the centres of both parts. The collimated ^{57}Co source was placed over the centre of the crystal. Results presented in Table 4.2 are average values from 3 acquisitions of 250.000 events each.

Table 4.2: Energy resolution with 3 mm thick CsI(Na) crystals in different configurations.

CsI(Na) crystal	E-PMT bias supply (V)	Energy resolution (% FWHM)
encapsulated with WSFs (white epoxy on top)	-1000	23.40
	-1100	23.19
encapsulated without WSFs (no reflector on top)	-1000	21.82
	-1100	21.79
encapsulated without WSFs + Al foil on top	-1000	19.42
	-1100	20.02

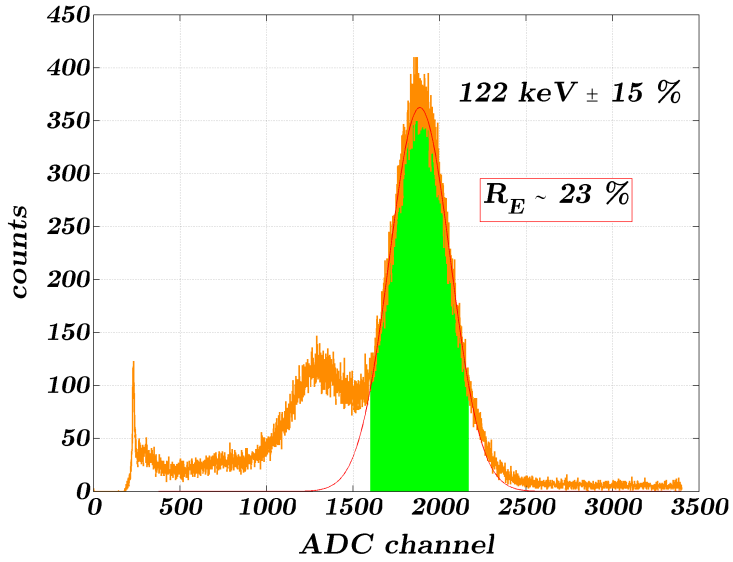

Figure 4.9: Energy spectrum for ^{57}Co, highlighting a ±15% energy window.

Figure 4.9 shows the energy spectrum for an acquisition using the crystal with embedded fibres applied in the SiPM WSF gamma camera. The energy resolution obtained in this configuration is near 23%, which represents a worsening of the performance by an absolute difference of almost 4% FWHM to the best energy resolution measured without the fibres.

The values obtained are in agreement with previous measurements performed by Soares *et al.* [46], who measured a 19% FWHM energy resolution at 122 keV for a similar CsI(Na) crystal directly coupled to Photonis X3392B E-PMTs and about 23% FWHM after coupling the fibres to the crystal. They are, however, relatively worse than the 13-15% FWHM at 140 keV reported by Sánchez *et al.* [79] for the MaPMT-based gamma camera presented in section 2.1.2, which uses Hamamatsu H8500 PMTs (24% QE at 420 nm) to read a continuous CsI(Na) crystal. Besides the higher number of photons created by the 140 keV relatively to the 122 keV of ^{57}Co, the better energy resolution performance may be due to the different PMTs and electronic readout system used.

4.2.2 SiPMs reading out 10 fibres

Initial positioning tests were done using 10 channels and scanning each direction separately. Ten SiPMs were individually coupled with optical grease to the clear end of the 10 central fibres and the setup was tested with ^{57}Co collimated by the 1 mm hole in a 6 mm Pb sheet. The collimated source was scanned in 1 mm steps along the 10 mm in each direction, performing 3 acquisitions for each position with a total of 100.000 events each.

SiPMs were all biased at the same voltage, at an ambient temperature of approximately 20°C. During acquisitions, a decrease in bias current was observed and manually adjusted in order to keep a constant supply current for the 10 SiPMs (*i.e.*, a constant gain, as much

as possible). This decrease was due to a temperature increase inside the dark box, further characterised in section 4.2.3. The adjustment meant an increase of SiPM bias voltage of about 0.1 V during acquisitions. Energy PMT was biased at -1000 V.

For every energy signal above a voltage threshold defined by the trigger generation circuit, signals from the 10 SiPM readout channels plus the energy signal were digitised by the 32 channel peak-sensing ADC (CAEN V785) and the values sent to a data acquisition PC. An energy window was defined digitally to image only γ-photons within a given range around the 122 keV photopeak (Figure 4.9).

4.2.2.1 Calibration

Before applying positioning algorithms, the system was calibrated to correct for electronic offset and gain variations between individual channels. An offset factor was subtracted to each channel's digitised value and the result was then multiplied by a gain correction factor. Gain calibration is absolutely necessary when biasing several SiPM units simultaneously, since each individual device has its particular breakdown voltage V_{br} and thus a different gain for a given overvoltage V_R. To minimise variations, the 10 SiPMs were chosen with similar gain and dark count rate, as tested by the manufacturer. The method used to obtain the gain calibration factors was the following. For each position, the three pulse-height spectra of the SiPM reading out the fibre aligned with the collimator hole were fit to a Gaussian curve and the average centroid position of the peak obtained. Positions obtained for the 10 channels were then compared with a reference value, considered as the average, and calibration factors were obtained by dividing each of the 10 values by the reference value.

4.2.2.2 Positioning algorithms

The signals from the SiPMs reading out the WSFs were used for positioning, applying two different algorithms based on maximum values, rather than the traditional Anger logic. It was observed that an Anger algorithm (equation 3.7) does not provide good imaging results for this application, not even at higher thresholds as had been predicted from simulation. The first algorithm used (A), simply considers the event position as that of the fibre coupled to the SiPM with maximum output (as algorithm B in simulation, section 3.5.2). The second algorithm (B) considers every two neighbouring fibres and calculates the centroid for the two corresponding SiPM output values whose sum is maximum. This is similar to algorithm C used in simulation (equation 3.9), but uses 2 instead of 3 neighbour signals, due to the reduced number of channels in this prototype. The centroids obtained in both directions with top and bottom WSFs were used to generate 2D images, from the 1D data acquired independently. Even though 2D position information was not obtained from the same scintillation event for both directions, this initial approach allowed an approximation to real 2D acquisition images.

4.2.2.3 Results

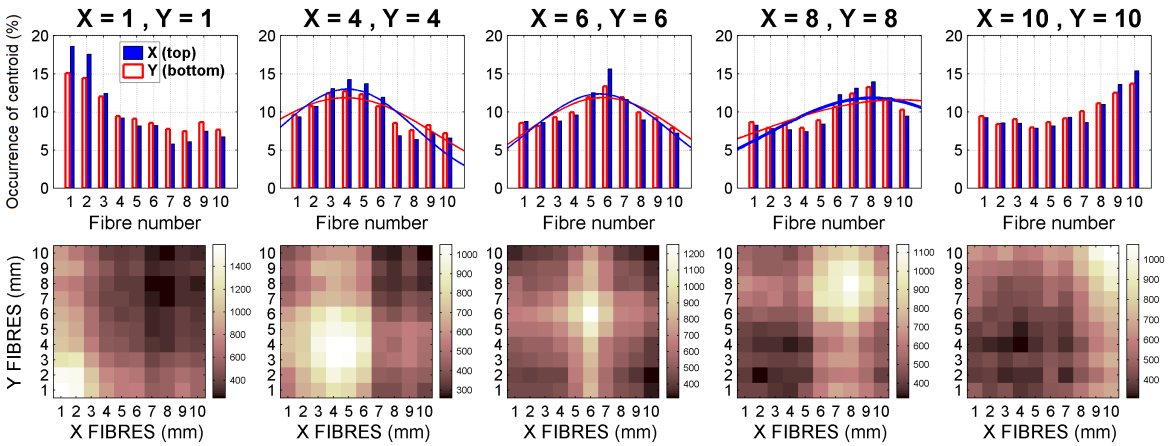

Figure 4.10: Results obtained with algorithm A (fibre with maximum output).

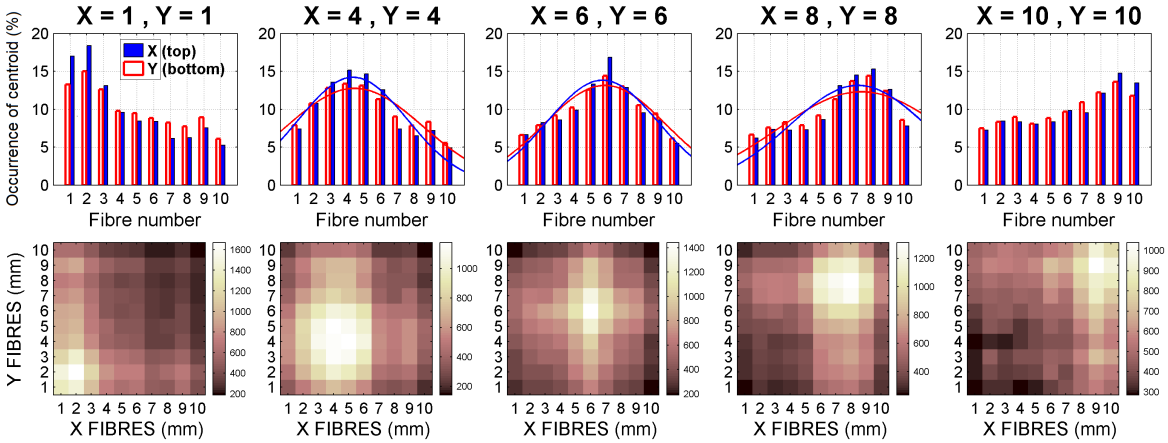

Figure 4.11: Results obtained with algorithm B (centroid of 2 neighbouring fibres with maximum summed output) for different collimator hole positions.

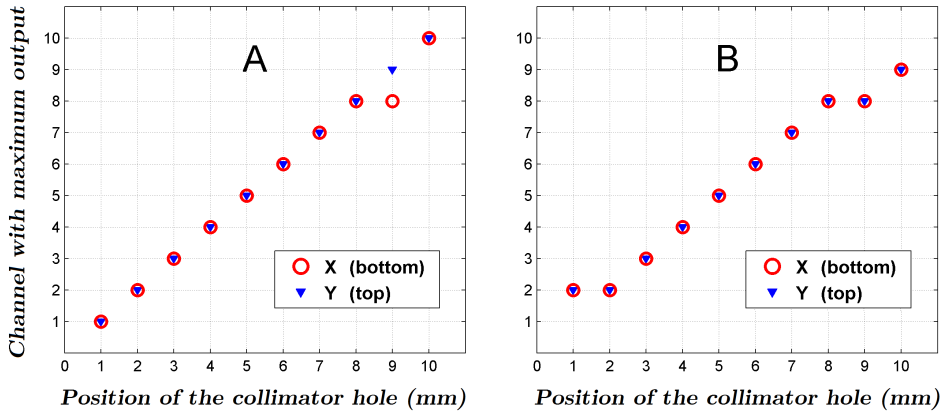

Figure 4.12: Position of the maximum ouput channel for algorithms A and B, along the 10 mm scanned in 1 mm steps in both directions.

Positioning results obtained with the two algorithms are similar, and shown in Figures 4.10 and 4.11. Algorithm B can better smooth differences between neighbour channels and apparently lead to slightly higher SNR and position resolution in more central positions, because it reduces the occurrence of events in edge positions (1 and 10). This, however, results in a degradation of position linearity at the edges, which is visible in Figure 4.12 B, where the highest response channel is plotted against the position of the collimator hole.

Nevertheless, algorithm B has the advantage of allowing smaller image pixels, while the pixel size of images obtained with algorithm A is limited to 1 mm. Figure 4.13 displays the same image obtained for collimator hole position (X=6, Y=6), but with twice the number of pixels in each direction, evidencing the edge effect.

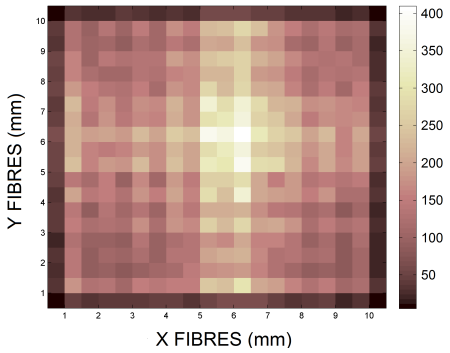

Figure 4.13: Image obtained with algorithm B for collimator position (X=6, Y=6), using 20×20 pixels (0.5×0.5 mm^2 pixel size).

4.2.3 Prototype with 10+10 SiPMs

A 10×10 mm^2 FOV prototype was assembled, using 10+10 SiPMs with the individual readout circuit developed earlier. As in the previous experiments, the gamma camera head, consisting of the scintillating crystal with WSFs, SiPMs and energy PMT, together with the corresponding front-end readout electronics, was placed inside a dark chamber, with various

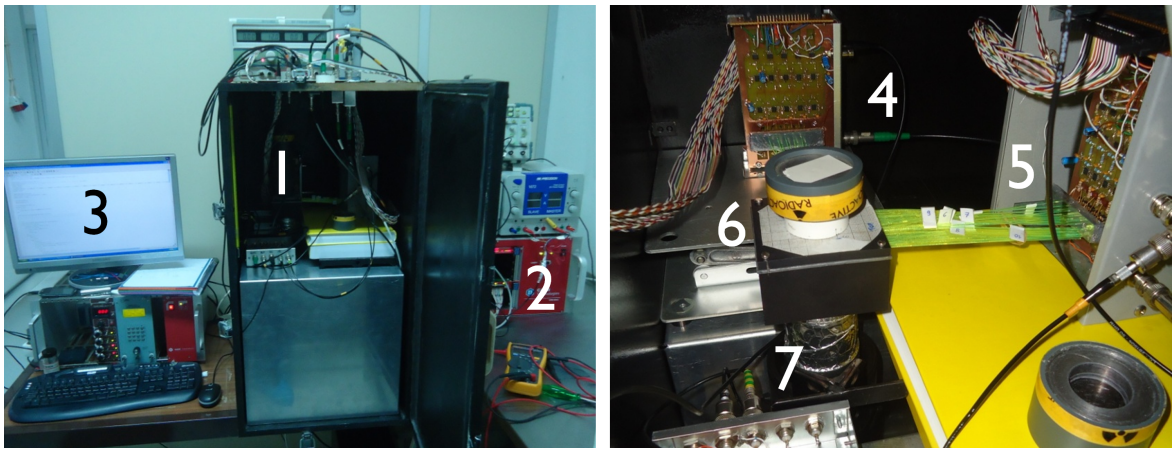

Figure 4.14: Photographs of the experimental setup of the SiPM WSF prototype gamma camera . Legend: 1 - dark chamber, 2 - ADC, 3 - PC, 4 and 5 - X and Y SiPMs with readout electronics, 6 - ^{57}Co source, Pb collimation and CsI(Na) crystal with WSFs, 7 - E-PMT.

connections to the outside, namely to power supplies and to the ADC, further connected to a computer via USB. Photographs of the experimental setup are shown in Figure 4.14.

From the 50 fibres of the crystal/WSF assembly in each direction, the central 10 were coupled to SiPMs. A common bias voltage was used for the 10 SiPMs in each direction, provided by an Ortec 710 bias supply. To ensure similar behaviour, two groups of 10 SiPMs were selected with similar gain and dark count rate, as tested by the manufacturer.

Initial temperature for all measurements presented in this section was kept at approximately 20°C. Bias voltage was manually adjusted during acquisitions in order to keep the supply current constant , so as to maintain the gain of the SiPMs as stable as possible. Without this adjustment, there would be an undesired decrease of the gain and consequently a decrease of the photon detection efficiency of the SiPMs, due to a temperature increase of 1-2°C inside the dark box. The rise of the temperature is caused by the heat dissipated by the front-end readout electronics located not far from the SiPMs. Figure 4.15 illustrates the current behaviour when voltage is left unchanged, for two different initial temperatures. Temperature was measured with a K thermocouple placed next to the SiPMs and connected to a multimeter with a resolution of 1°C.

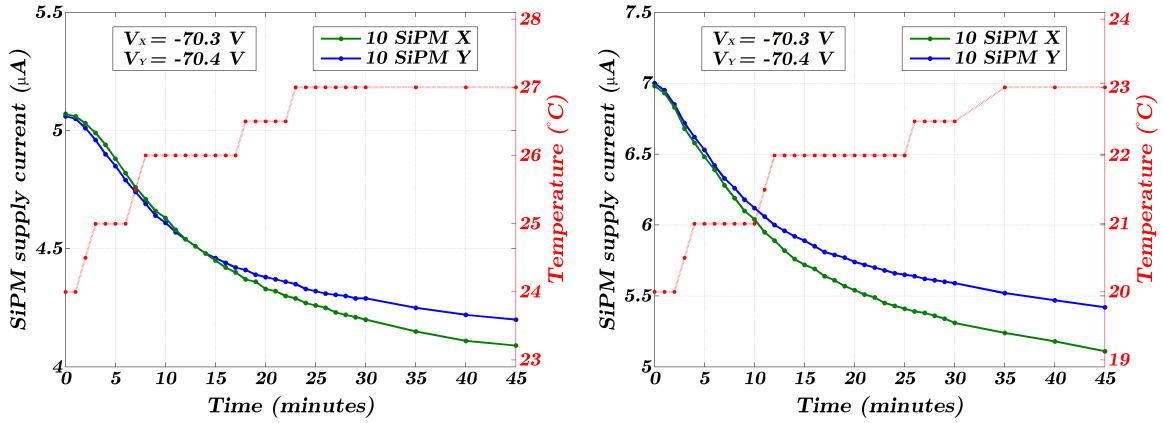

Figure 4.15: Decrease of SiPMs supply current (*i.e.* gain) due to temperature increase over operation time, for a constant supply voltage and two different initial conditions.

The usual acquisition time for most of the images obtained with this prototype was 10 to 15 minutes. As visible from the plots, the largest current decrease occurs in this initial period, being about 0.5 and more than 1 μA for the initial condition of about 5 and 7 μA, respectively. The lower variation observed in the former case indicates that a constant current supply of 5 μA requires a less intense adjustment and thus is preferable.

4.2.3.1 Collimation

A 4 mm thick cylindrical lead container cover with a 1 mm diameter hole was used for ^{57}Co collimation and position calibration of the 10+10 SiPMs prototype, as shown in Figure 4.16.

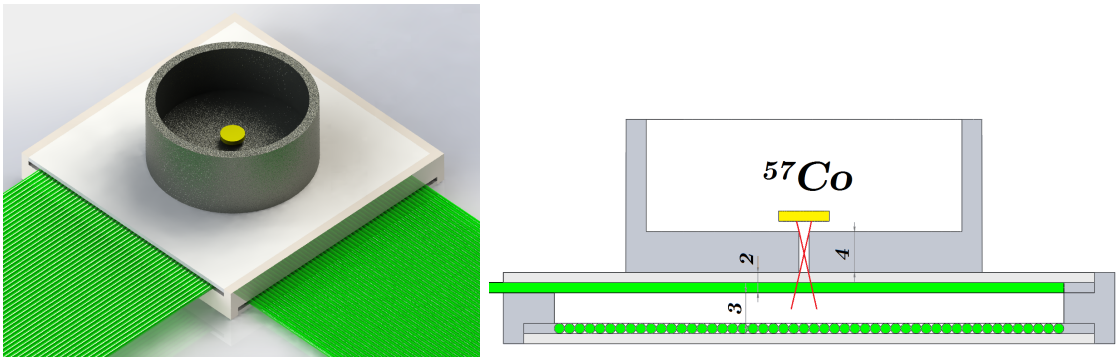

Figure 4.16: Schematics of Pb collimation used for ^{57}Co source (represented in yellow) in 2D imaging studies. Left: overall 3D sketch. Right: 2D profile illustrating the spread of the γ beam through the 1 mm hole.

The percentage of 122 keV photons transmitted through 4 mm of Pb is less than 0.01%. Regardless of this, due to geometrical parameters defined by the experimental conditions, in the central plane of the crystal the image source will have a 2.75 mm diameter, as can be seen in the figure. A thicker collimator would focus the beam further but would not provide an efficient acquisition due to the low activity of the used source. Therefore, a compromise was found which allows a relatively narrow focusing while acquiring sufficient image statistics.

4.2.3.2 Calibration and software

Similarly to what was done previously for 10 SiPMs, calibration was accomplished by performing a diagonal scan (x = y) with the ^{57}Co source through the imaging area, placing the 1 mm collimator hole in ten different positions. In this way, both directions could be calibrated simultaneously. For each position, 100.000 events were acquired and a $\pm$20% energy window applied around the 122 keV photopeak. The method for obtaining gain calibration factors was the same described before (4.2.2.1). A dedicated MatLab® software was developed, which allows to apply gain calibration factors for the 20 channels and show the resulting images obtained through algorithms A and B for a definable energy window and common threshold value. Images can be visualised as 2D or 3D histograms, in the raw form or after application of a symmetric Gaussian low-pass filter with adjustable size and standard deviation σ. In the case of alg. B, the number of image pixels can be defined and the neighbour signals to sum can be chosen as 2 or 3. As shown in Figure 4.17, this software allows also to visualise the frequency of the centroids calculated in each direction, for both algorithms, as well as the individual SiPM spectra before and after calibration. Imaging efficiency values are provided, together with an estimate of the energy resolution. In addition, for each 2D image it is possible to analyse profiles across chosen pixel lines or regions of interest, in order to estimate spatial resolution. Images and energy spectrum can be saved, together with the imaging parameters used, for later analysis.

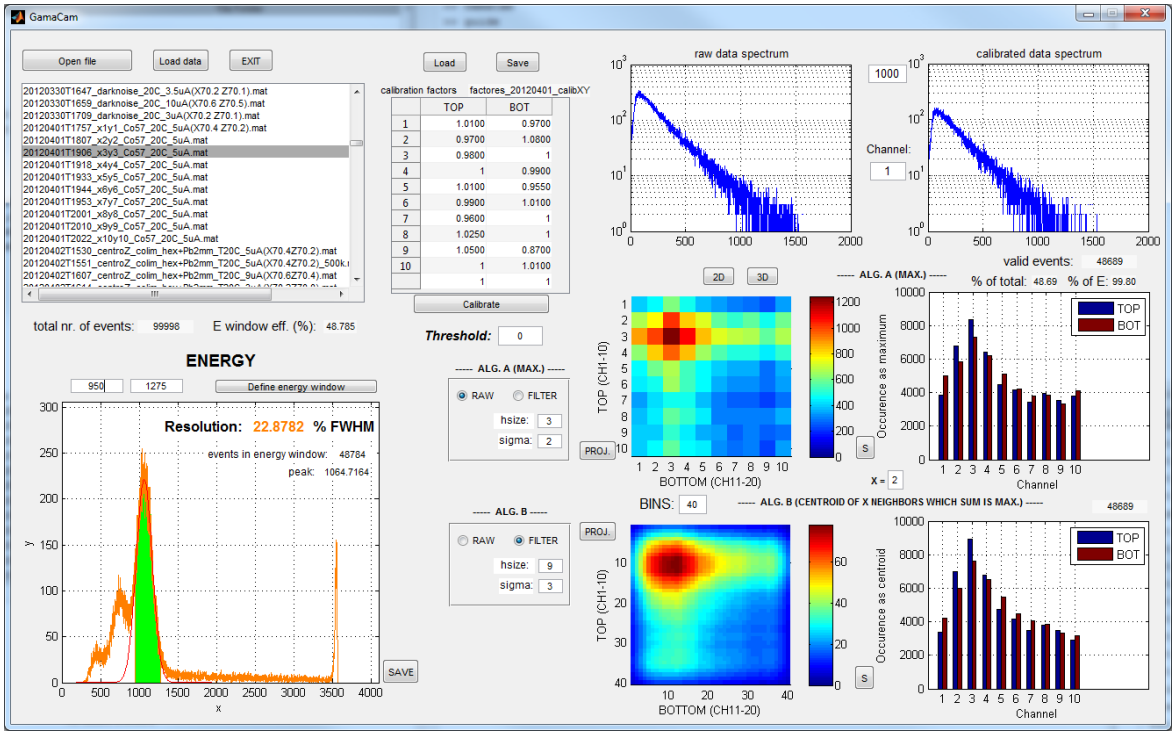

Figure 4.17: MatLab® graphical user interface developed for calibration, image reconstruction and analysis with the 10×10 mm^2 SiPM WSF gamma camera prototype.

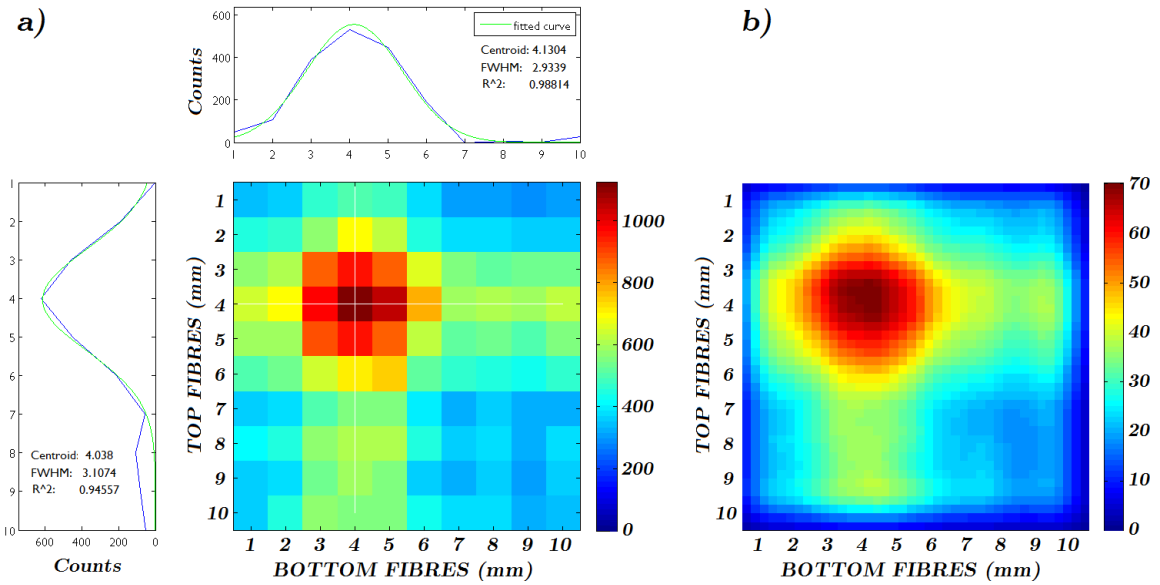

Figure 4.18: a) Raw image reconstructed through alg. A for ^{57}Co acquisition with collimator hole in (4,4) and plots of the profiles across highest intensity pixel lines, fitted by Gaussian curves. b) Image reconstructed through alg. B for the same acquisition, using 40×40 pixels and after application of a Gaussian low-pass filter (size 9×9, σ=2).

4.2.3.3 Results

The diagonal scan allowed measuring the position linearity of the system, as well as evaluating its spatial resolution with ^{57}Co. For each measurement, about 55% of the events were inside the energy window and the centroids in x and y directions were calculated through algorithms A and B (please see section 4.2.2.2), reconstructing 2D images. For the raw 10×10 pixel images, profiles across the highest intensity pixel lines were measured after subtracting the background, as exemplified in Figure 4.18. The FWHM of these profiles is considered an approximation to the intrinsic spatial resolution and results are presented in Figure 4.19, with the calculated spread of the γ-beam diameter subtracted in quadrature. In the case of filtered images with a higher number of pixels, equivalent results were obtained using the same method applied to a user-defined region of interest. Average values around 3 mm were obtained with alg. A and slightly higher with alg. B. A best detector intrinsic spatial resolution of about 2 mm FWHM was measured. There is a significant variability of the values obtained at each position, mainly due to a deficient calibration method, which relies on the manual scan of the source with its associated error. Fluctuations result also from differences between individual channels, which are considerable for some particular channels, such as top channel 1 or bottom channels 1 and 9, further complicating the calibration and contributing to the non-uniformity of the spatial resolution. Plots of the measured versus real position of the collimated source along the scan are shown in Figure 4.20 and demonstrate good position linearity. Values are not presented for the edge positions, because a Gaussian fit is not possible or properly done in these cases. The situation, however, is similar to the one presented in Figure 4.12, where even at the edge mm positions alg. A keeps linearity, while alg. B shifts the centroid to the penultimate position thus losing linearity at the edges.

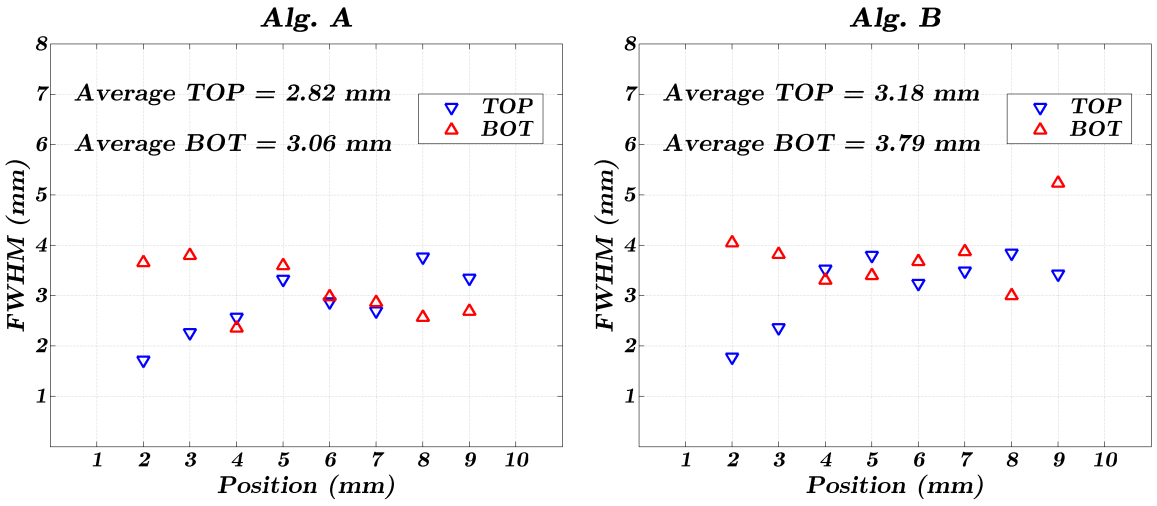

Figure 4.19: Corrected FWHM of the profiles across the highest intensity pixel lines, for the different positions along the diagonal scan with collimated ^{57}Co source.

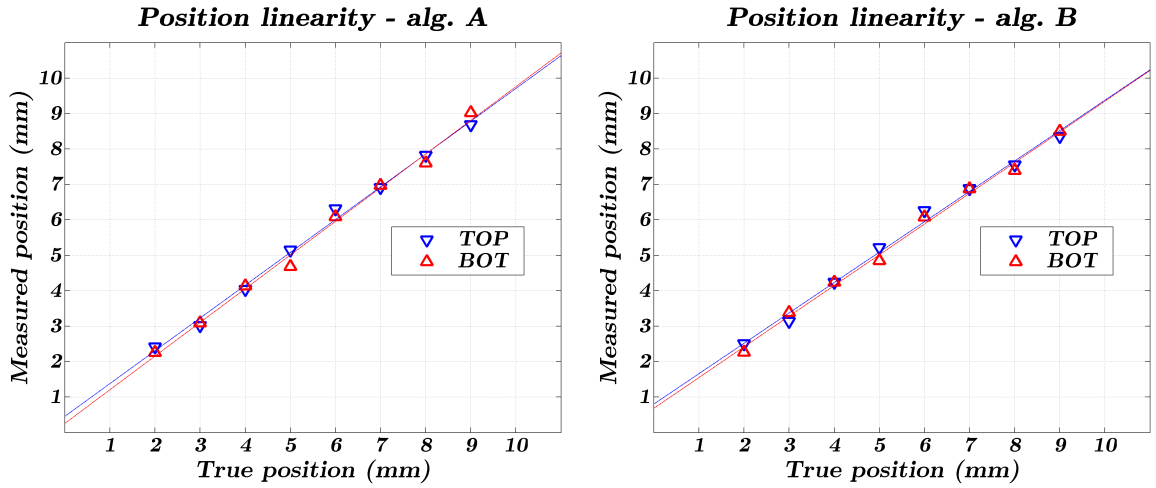

Figure 4.20: Measured positions along the diagonal scan with collimated ^{57}Co source across the imaging area of the SiPM WSF gamma camera prototype, for top and bottom fibres.

4.3 Discussion and conclusions

A small prototype SiPM WSF gamma camera with a FOV of 10×10 mm^2 has been successfully assembled and tested with a ^{57}Co source. Energy resolution is approximately 23% FWHM for the 122 keV γ-rays using a CsI(Na) crystal with embedded WSFs, which is slightly worse than the nearly 19% of a similar crystal without fibres measured in the same conditions. Nevertheless, this loss of energy resolution due to the fibres is not critical for the resulting image, considering the spatial resolution that may be obtained with the WSFs. It is possible to define a relatively narrow window around the photopeak while keeping a good imaging efficiency.

SiPM devices have very promising features such as high gain and PDE, small size and low power consumption, which make them interesting for application in a WSF gamma camera, potentially allowing the development of a compact imager with very good spatial resolution (R_i < 2 mm). However, their noise can become a serious drawback for an efficient WSF readout, when working at room temperature with the low light levels transmitted by the fibres during the slow scintillation decay of CsI(Na). A long pulse integration time was needed to detect this light ($\sim$ 1 μs), which came with the price of a higher influence of SiPM dark counts.

Nevertheless, initial tests with 10 SiPMs reading out 10 WSFs one direction at a time demonstrated the feasibility of using SiPMs for positioning in a CsI(Na) WSF gamma camera operating at room temperature. Given the experimental limitations and margin for improvement, these initial results were encouraging, leading to the assembly of a real 2D imaging prototype (10+10 channels), whose intrinsic performance was characterised. Good position linearity was observed after calibration and an average intrinsic spatial resolution of approximately 3 mm FWHM was measured with ^{57}Co, which is comparable to the performance of

modern Anger cameras or of the WSF gamma camera using MaPMTs.

Results obtained at 20°C and the observed dependence of the detection efficiency with temperature suggest that further cooling is necessary to achieve better positioning results than previous work using MaPMTs. Furthermore, having different bias voltages applied to smaller groups of SiPMs or, ideally, individually adjustable bias voltages, together with a more accurate position calibration method (*e.g.* with a ^{57}Co flood source), would improve uniformity and imaging results.

CHAPTER

5

PRE-CLINICAL EVALUATION OF THE DEVELOPED PROTOTYPE

The performance of the small prototype with 10+10 SiPMs, presented in the last chapter, was tested with the most used medical radionuclide, ^{99m}Tc, and using a parallel-hole collimator. This allowed evaluating the performance of the SiPM WSF gamma camera in a more realistic context, closer to the desired clinical application. Besides imaging tests performed with small line phantoms filled with a ^{99m}Tc solution, a pre-clinical evaluation of the developed prototype was done by imaging a small mouse injected with a ^{99m}Tc-based radiopharmaceutical.

5.1 Phantom imaging with ^{99m}Tc

5.1.1 Collimation

For ^{99m}Tc acquisitions, a low energy high resolution (LEHR) hexagonal parallel-hole collimator taken from a large FOV gamma camera was used. A piece with about 40×40 mm^2 (Figure 5.1) was cut from the larger collimator and placed on top of a 2.2 mm thick lead sheet with a 10×10 mm^2 central opening. This second collimator was employed to limit the imaging region of the crystal to the volume covered by the fibres that are read out by SiPMs, excluding all the remaining volume which would otherwise contribute with spurious events to the image.

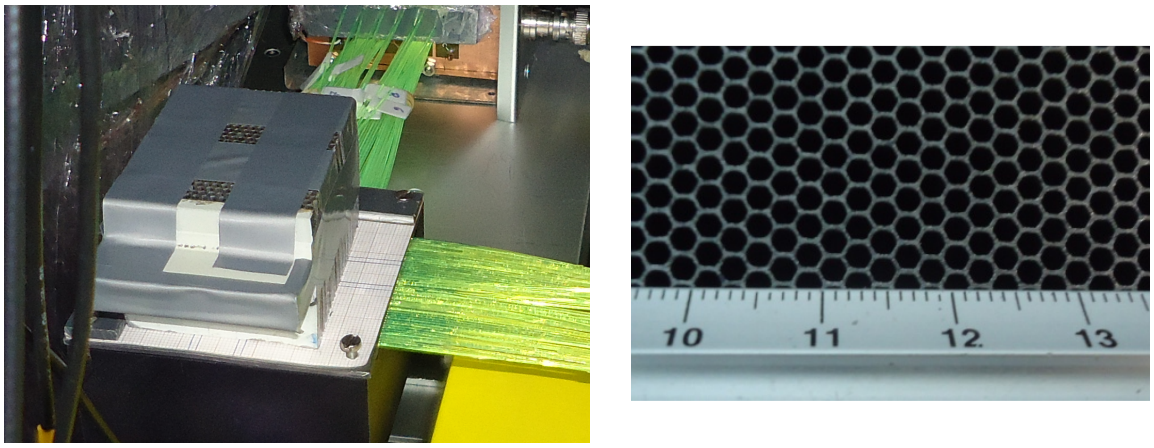

Figure 5.1: Photographs of the parallel-hole collimator used for ^{99m}Tc. Left: in experimental context, on top of a 2.2 mm thick Pb sheet with a 10×10 mm^2 opening, over the crystal. Right: detailed view of the holes.

The collimator's dimensions are: length $L = 40$ mm, hole diameter $d = 2$ mm (for an imaginary circle confining the hexagon) and septal thickness $t \approxeq 200$ μm, resulting in a geometric spatial resolution of nearly 7.2 mm FWHM at 10 cm, as given by equation 1.7 considering $L_e \approx 39.925$ mm at 140 keV and $c = 3.5$ mm (1 mm glass window + 1 mm fibre layer + 1.5 mm till the centre of the crystal). For the experimental conditions, taking into account the addition of the 2.2 mm lead sheet under the collimator, the resolution is approximately 2.3 mm at the collimator surface, calculated through the same equation.

On the other hand, the geometric efficiency g of this collimator, obtained through equation 1.8, is approximately 0.0498%, considering $K \approx 0.9798$ as given by [17] for round holes in a hexagonal array.

5.1.2 Procedure

The ^{99m}Tc source (E_γ=140.51 keV, $T_{1/2}$=6.01 h) was obtained from the Nuclear Medicine department of Coimbra University Hospital (HUC), in the form of an aqueous solution with a total initial activity of 4 mCi in a volume of about 1 ml. In order to get to know its spatial distribution, and for safety reasons, the ^{99m}Tc solution was coloured with a red dye (food colorant). Small amounts of the solution were then drawn into a syringe and introduced into 1 mm holes drilled horizontally in pieces of PMMA (poly(methyl methacrylate)).

With the exception of collimator and source, the experimental setup and conditions were the same as described above for imaging with ^{57}Co, in section 4.2.3.

5.1.3 Results

Energy resolution and energy windows

The energy spectrum for an acquisition of 500.000 events is shown in Figure 5.2. A cut in the lower part of the spectrum is visible, which corresponds to the threshold level used in the comparator circuit required for trigger generation from the E-PMT signal. The measured energy resolution was approximately 21% at 140 keV. A ±10% energy window was selected for imaging, as it represents a good compromise between rejecting scattered photons and obtaining sufficient image statistics. 52.6% of all events are within this ±10% energy window, while ±5% and ±20% windows include 31% and 68.2% of the events, respectively.

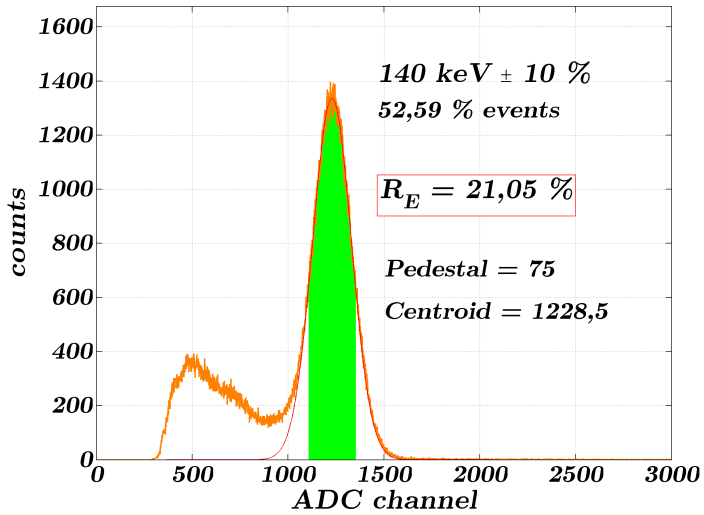

Figure 5.2: Energy spectrum for ^{99m}Tc, highlighting ±10% energy window used for imaging.

Spatial resolution

Figure 5.3 shows a photograph of a 1 mm line phantom placed over the imaging area and the corresponding image obtained with the SiPM WSF gamma camera prototype.

The profile for the coordinate perpendicular to the direction of the hole was fitted to a Gaussian curve after background subtraction: the FWHM of this fit, 3.02 mm, is considered an approximation to the extrinsic spatial resolution of the system (R) at a SCD of 0 mm, since the ^{99m}Tc line was practically on the collimator surface.

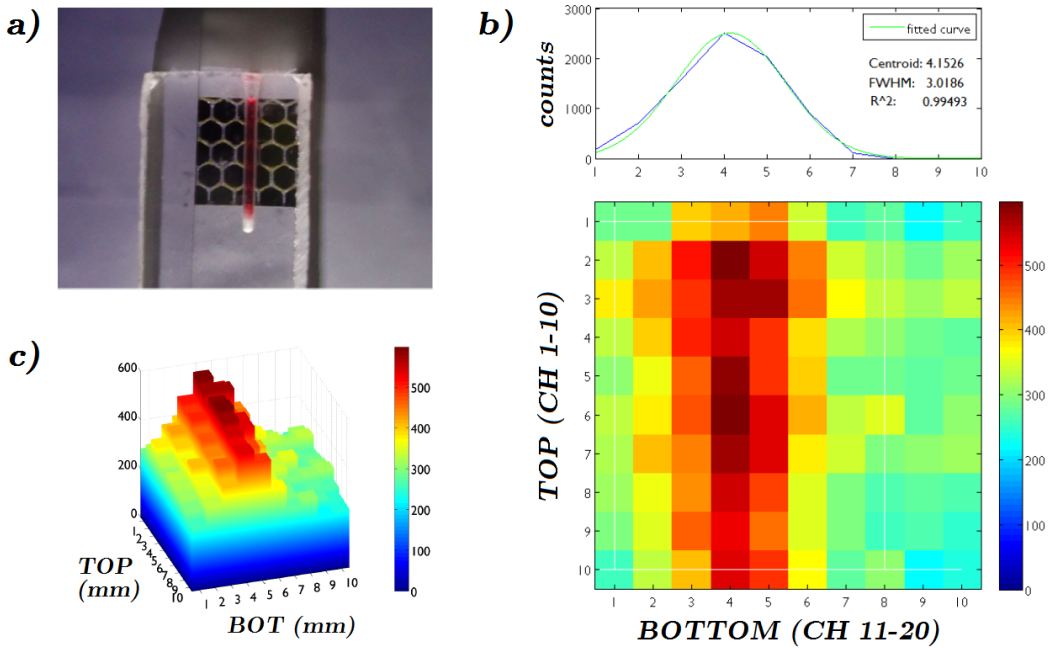

Figure 5.3: a) Photo of 1 mm hole drilled in PMMA, filled with ^{99m}Tc and placed over the imaging area, parallel to bottom WSFs; b) Corresponding 2D image reconstructed with alg. A and plot of the 1D profile for delimited region; c) 3D histogram of the same image.

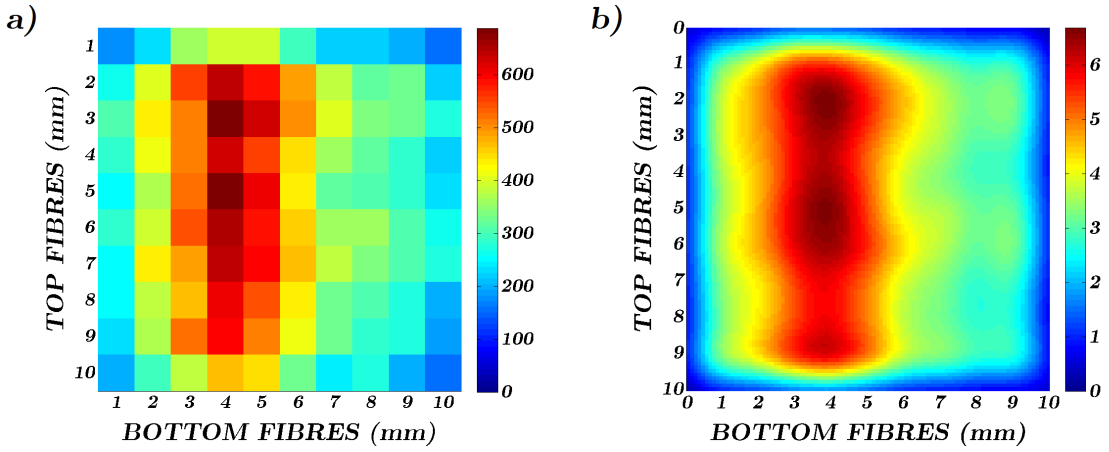

Figure 5.4: Image of 1 mm ^{99m}Tc line reconstructed with alg. B: a) 10×10 pixels raw image; b) 100×100 pixels image after application of Gaussian low-pass filter (size 33×33, σ=5.75).

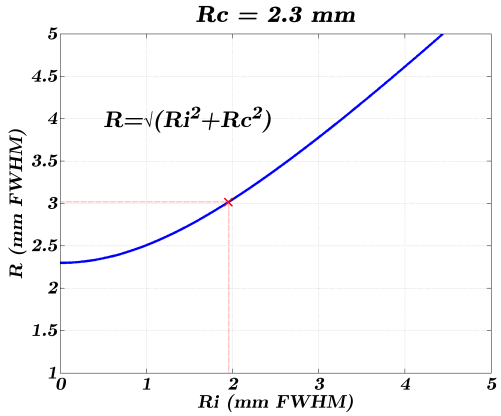

Figure 5.5: Overall spatial resolution R of a gamma camera as a function of its intrinsic spatial resolution R_i, for a fixed geometric collimator resolution R_c of 2.3 mm (fixed SCD).

As in a conventional gamma camera, the overall spatial resolution R is limited by the geometric resolution of the collimator R_c, as well as by the intrinsic spatial resolution R_i. From the equation of R as a function of R_i for the R_c of this collimator, plotted in Figure 5.5 for the fixed SCD used in these experiments, the value of R measured corresponds to an intrinsic detector spatial resolution of approximately 2 mm (1.95 mm) FWHM with ^{99m}Tc.

The image of the ^{99m}Tc line reconstructed through alg. B can be seen in Figure 5.4 a), using the same pixel size as that allowed by alg. A (1 mm^2). The spatial resolution obtained with alg. B is equivalent to the one measured with alg. A. Even though alg. B does not provide a visible improvement of the spatial resolution, it allows a higher image definition, as shown in Figure 5.4 b), the same image but with a pixel size of 100×100 μm and after application of a Gaussian low-pass filter.

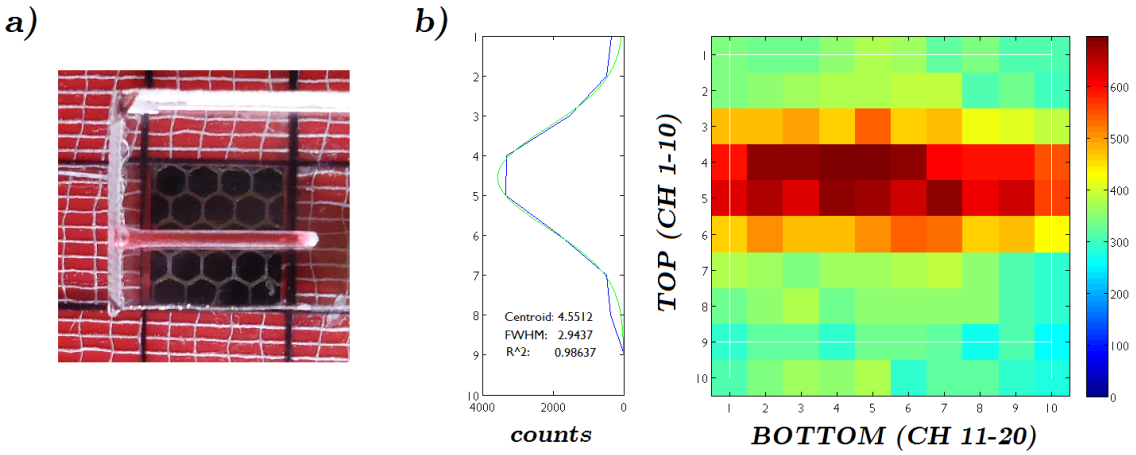

Figure 5.6: a) Photograph of 1 mm hole drilled in PMMA, filled with ^{99m}Tc and placed over the imaging area, parallel to top WSFs; b) Corresponding 2D image reconstructed with alg. A and plot of the 1D profile for delimited region of interest.

The ^{99m}Tc line was placed over the imaging area in the orthogonal direction, *i.e.*, in the direction of the fibres on the top side of the crystal. The resulting image is shown in Figure 5.6. The FWHM of the profile in the top fibres' direction (after background subtraction) is under 3 mm (2.95 mm), which corresponds to a slightly better spatial resolution in this direction, in agreement with previous measurements with ^{57}Co (Figure 4.19, page 91). The better alignment with the collimator holes may also be contributing to the better spatial resolution observed when the line is parallel to the top fibres.

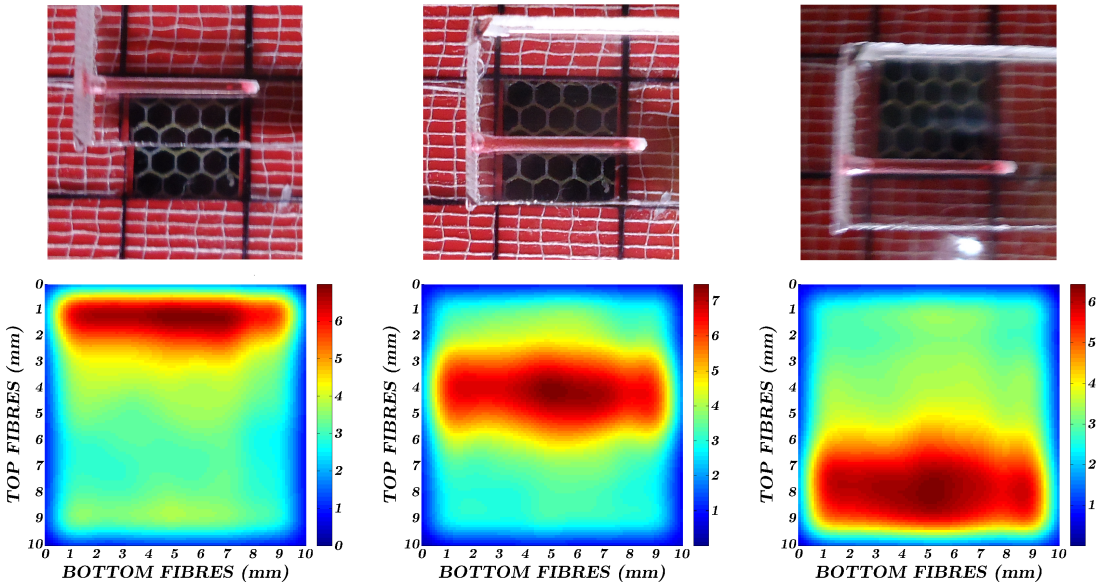

Figure 5.7: Images of ^{99m}Tc line parallel to top WSFs, in different positions.

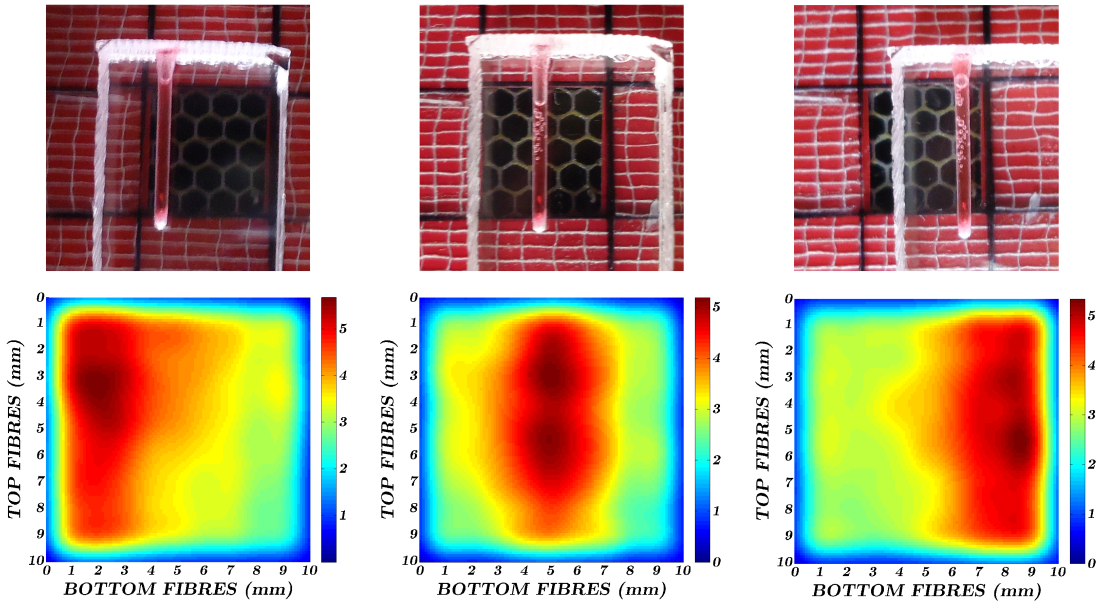

Figure 5.8: Images of ^{99m}Tc lines parallel to bottom WSFs, in different positions.

This is also visible in the images shown in Figures 5.7 and 5.8, obtained with alg. B using 100×100 pixels and a Gaussian low-pass filter of size 33×33 and σ=6. The agreement of the line's position in the images to its real position is clearly visible.

Images obtained from two 1 mm holes separated by 4 mm are shown in Figure 5.9. The two lines are clearly distinguishable, including in the case of partially filled holes (a)). Again, the spatial resolution is better for the case where the line is parallel to the top fibres, possibly due to a better alignment with the collimator holes in this direction.

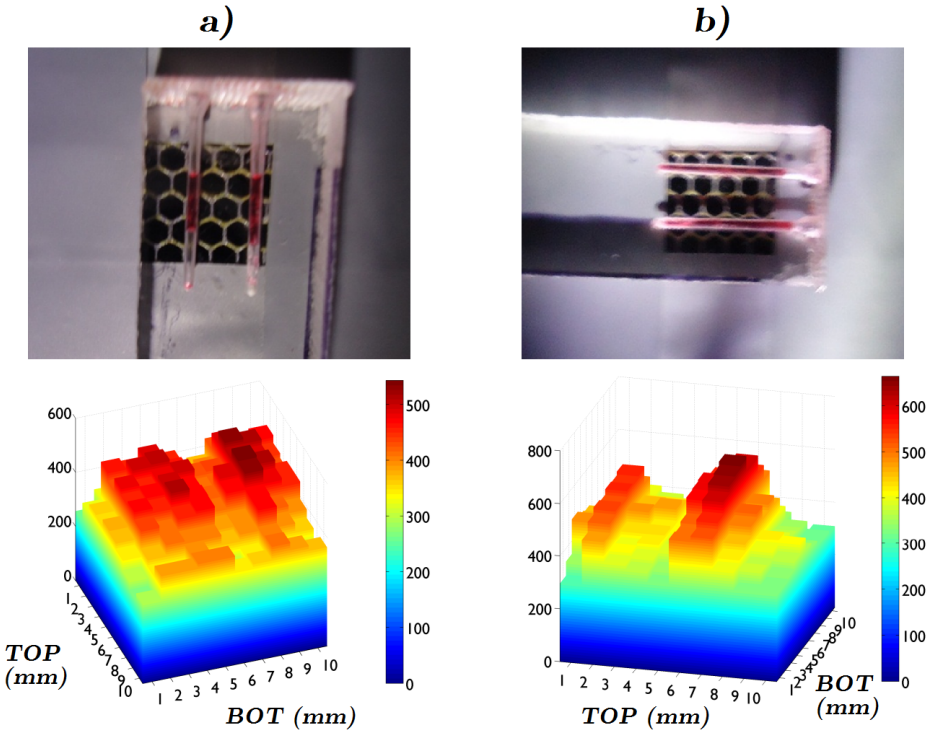

Figure 5.9: Top: photographs of PMMA phantom with two 1 mm holes separated by 4 mm, filled with ^{99m}Tc and placed over the imaging area, parallel to bottom (a) and top fibres (b). Bottom: corresponding images with alg. A. Image was rotated in (b) for better visualisation.

Sensitivity

The sensitivity of the small SiPM WSF gamma camera prototype was evaluated by imaging a ^{99m}Tc sample of known activity during a fixed period of time (10 minutes). The sample was a small volume contained in a syringe, with initial activity of 286 μCi measured by a well-ionisation chamber at IBILI - *Instituto Biomédico de Investigação de Luz e Imagem* (Coimbra). The parallel-hole collimator was removed and the sample was placed over the 1 cm^2 imaging area limited by the lead sheet described in section 5.1.1.

Since acquisitions were performed only several hours after the initial activity measurement, source decay was taken into account, considering the activity to be that given by

$$A = 286 \times e^{-(ln(2)t/6.01)}, \tag{5.1}$$

where t was the number of hours passed since the activity measurement until the middle of the acquisition and 6.01 is the half-life time ($T_{\frac{1}{2}}$) of ^{99m}Tc, in hours.

By dividing the number of events obtained within a ±10% energy window by the 10 minutes of the acquisition and by A, an intrinsic sensitivity of 80.18 cpm/μCi was measured (Figure 5.10 a)). This value, however, is well below the intrinsic capability of the WSF gamma camera. This was acknowledged when comparing the sensitivity of the prototype in two situations:

- using the triggered ADC to read out the energy signal (as in all measurements presented in chapters 4 and 5);
- simply replacing the ADC with a Nucleus PCA-II multi-channel analyser, while keeping all other experimental conditions.

From the resulting spectra, plotted in Figure 5.10 b), it is clear that the external triggering of the ADC needs optimisation and that the sensitivity of the SiPM WSF gamma camera system can be substantially improved. Even though sensitivity is predominantly limited by the collimator, the higher statistics provided by the improvement of the intrinsic sensitivity to its full potential, would certainly have a positive impact on the imaging performance of the camera, while lowering acquisition time.

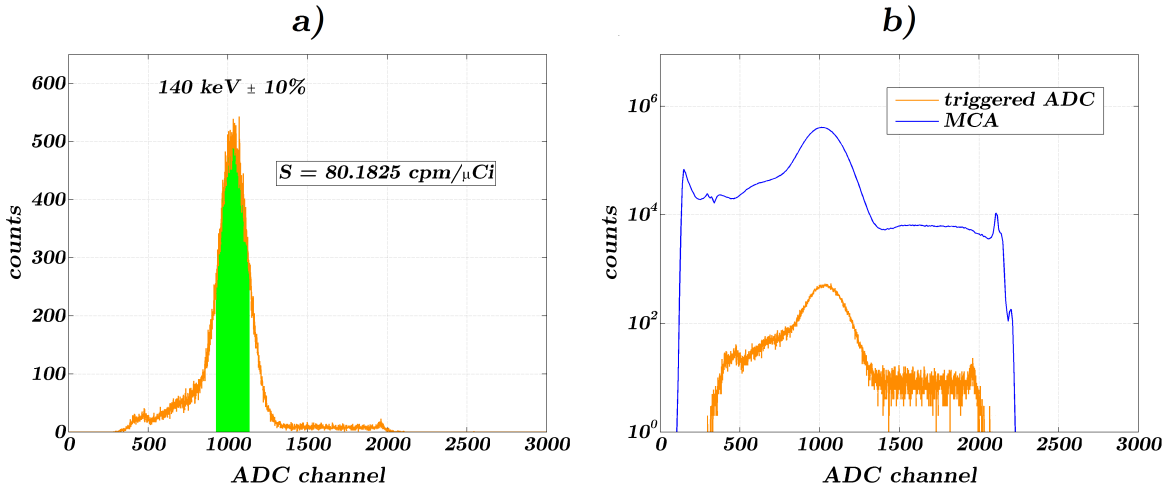

Figure 5.10: a) Energy spectrum of 10-minute aquisition of a sample with known activity with the SiPM WSF gamma camera prototype (readout by triggered ADC); b) Comparison with identical measurement using MCA readout.

5.2 Small animal imaging with ^{99m}Tc-HMDP

With the collaboration of Professor Cristina Santos from IBILI, a small mouse was imaged with ^{99m}Tc-HMDP, a bone tracer.

5.2.1 Experimental procedure

After anaesthesia, the mouse was injected with 0.1 ml of ^{99m}Tc-HMDP (tail vein injection), with an initial activity of 1.39 mCi. The initial uptake of the radiopharmaceutical was monitored by imaging the small mouse with a large FOV commercial NaI(Tl)-PMT gamma camera existent at IBILI (Figure 5.11), a GE 400AC equipped with a LEHR parallel-hole collimator and using a Xeleris imaging workstation. This allowed also to make a qualitative assessment and comparison between the imaging performance of a typical Anger camera and that of the developed SiPM WSF gamma camera prototype, which was used to scan the same mouse afterwards.

Because of the very small FOV of the SiPM WSF gamma camera prototype, several 1 cm^2 scans were consecutively performed over a larger area of the mouse. For this purpose, a cm^2 grid was drawn on two transparent thin plastic sheets. The first sheet was glued with double-sided tape to the top surface of the collimator, aligning the grid with the fibres in both directions and centring it at the imaging area. The mouse was fixed onto the second sheet and both sheets were then overlaid and fixed together in each acquisition, aligning the grids. In between scans, the top sheet with the mouse was moved to the next cm^2.

The experimental setup of the prototype was the same as before, with each SiPM group kept at 5 μA and E-PMT biased at -1 kV. The initial temperature of the system was approximately 21°C for all acquisitions. Calibration of the SiPM response in these conditions

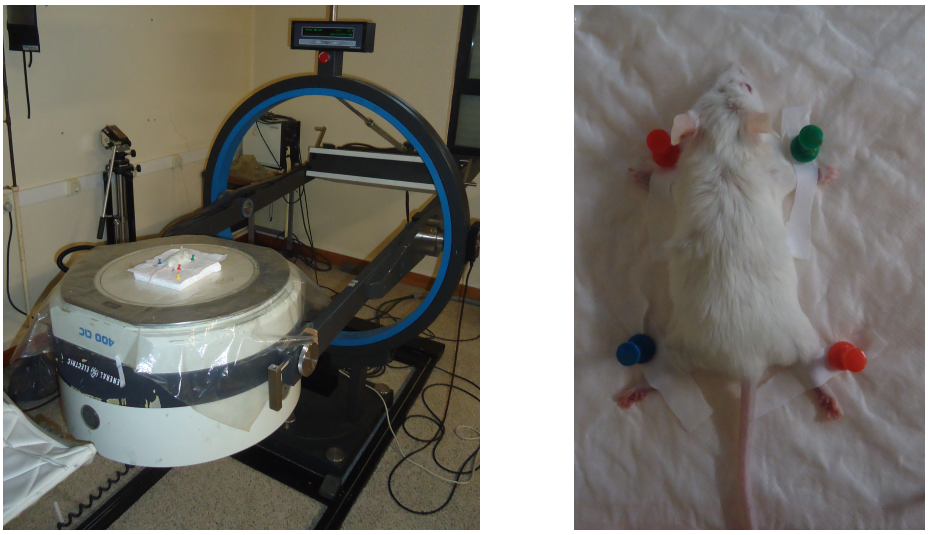

Figure 5.11: GE 400AC gamma camera used to image a small mouse.

was performed with ^{57}Co, as previously described in section 4.2.3.1. Acquisition time of the first scan was 5 minutes and that of the following scans was prolonged in accordance to the source's half-life, so as to have an equivalent number of decays in all acquisitions. Algorithm A was used for image reconstruction.

Since the energy spectra for acquisitions of separate areas of the mouse was naturally different and a similar energy window of ±15% was applied to all images, each cm^2 image was composed of a different number of events, considerably different in some cases. For this reason, the images had to be normalised, using the image with the highest number of events as a reference and multiplying all the others by a correction factor. This factor was determined for each image by its respective number of events, but ultimately adjusted in order to ensure continuity between neighbour images.

5.2.2 Imaging results and discussion

Figure 5.12 (next page) shows images of 2 minute acquisitions with the Anger camera, soon after the injection and one hour after. In the first acquisition, the syringe with ^{99m}Tc was placed in three different positions, to be used as references in the image: the right line is at the mouse's nose tip, the medium line is at the animal's upper limbs and the left line at the start of its tail. This allowed having a notion of the total size of the animal and its proportions in the image. In this first acquisition, a lead plate was also placed under the mouse's tail, to cover the background activity from the injection site and better visualise the initial body uptake. The relatively high activity at the injection site is still visible in the image obtained one hour after. At this time, it is visible from the image that the radiopharmaceutical is distributed mostly in the thoracic region. Relatively to the first acquisition, there is a spread of the radiopharmaceutical into the mouse's bone structure, showing uptake by the skull and vertebral spine, but this spread is nevertheless lower and less visible than what would be expectable after one hour. A contour around the limbs is discernible but not obvious, particularly considering that these were spread open, as shown in Figure 5.11. The cause for this lower-than-expected spread of the radiopharmaceutical was that the mouse's body ceased to function sometime between 30 and 60 minutes after injection, preventing further blood circulation and biodistribution of the ^{99m}Tc-HMDP.

For this reason, the image obtained from the subsequent acquisitions with the SiPM WSF gamma camera prototype should then represent the same distribution as the last image acquired by the Anger camera. In fact, this is what was observed, as can be seen in Figure 5.13, the resulting image from all the scans after normalisation and application of a Gaussian low-pass filter (size 5×5, σ=1.5). This filter was useful to blur the differences in the borders between squares in the image, which were visible even after normalisation and were mainly due to the imprecision of the positioning method at the edges.

The need for normalisation of the several cm^2 images when adding them together in a

single image was obvious. For instance, the percentage of valid events (*i.e.*, within the energy window) was as high as 32.8% for an acquisition in the thoracic region and as low as 1.6% for the acquisition of the left lower limb (corner square in the image), where the majority of events resulted from Compton scattering. Some squares were not imaged because the energy spectrum observed from their acquisition was composed practically of only Compton events and it was decided to move to the next square. The resulting image is in very good agreement with the distribution observed with the Anger camera, showing a higher concentration of ^{99m}Tc-HMDP in the thoracic region.

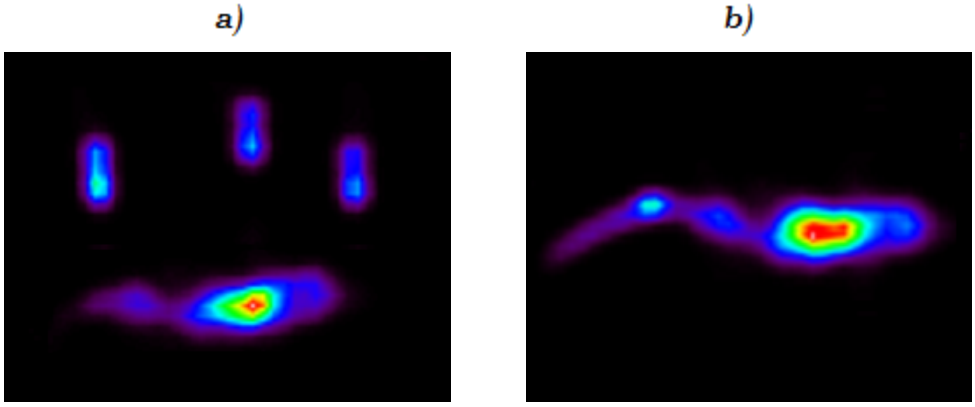

Figure 5.12: Whole mouse images obtained with Anger camera (GE 400AC), a few minutes after injection of 1.39 mCi of ^{99m}Tc-HMDP (a) and 1 h after (b). The 3 lines in a) are from a syringe and were used for position reference (please, see text).

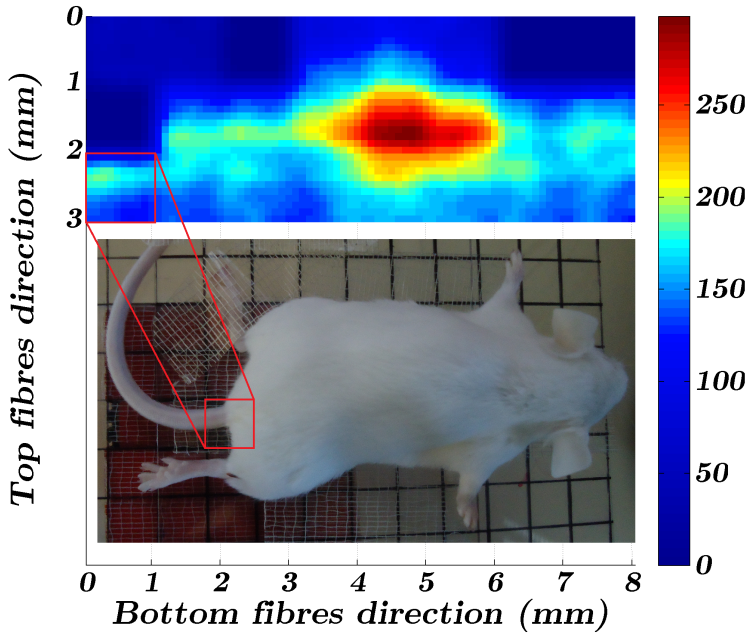

Figure 5.13: ^{99m}Tc-HMDP mouse image (8×3 cm^2) obtained from several 1 cm^2 scans with the SiPM WSF gamma camera prototype (darker squares were not acquired).

The shape of the skull and activity along the vertebral spine are also clearly visible. Despite all the limitations of the experimental setup and techniques used to obtain a larger image with the small SiPM WSF gamma camera prototype, the result indicates that, comparatively to the image obtained with the Anger camera, a better granularity and detail is possible.

5.2.3 Second trial

Due to the unexpected early death of the mouse before the proper biodistribution of the radiopharmaceutical, the experiment was repeated on a second mouse, at a different occasion.

The experimental procedure was the same described in 5.2.1. However, some of the experimental conditions differed: the initial activity of ^{99m}Tc-HMDP injected was 250 μCi (more than 5 times lower), the number of 1 cm^2 scans was larger (in order to image the largest possible area of the mouse) and the average temperature during these scans was a little higher, 23°C (calibration of the prototype had to be performed at this temperature). All the other experimental conditions were the same.

The image obtained with the GE gamma camera approximately 2 hours after injection is shown in Figure 5.14. The mouse was then euthanised and scanned with the SiPM WSF gamma camera prototype, over 43 adjacent positions, 5 minutes in each (adjusted for ^{99m}Tc decay time). The resulting image after normalisation and application of a Gaussian low-pass filter (size 7×7, σ=2) is presented in Figure 5.15. As in the previous experiment, some squares were not imaged, as it was visible that they were not including practically any valid events or, in the case of the last square (bottom right), because the correspondent image file was corrupted.

Again, the agreement between the images obtained with the different cameras is clear, this time showing a significantly higher concentration of radioactive tracer in the bladder, but also the distribution of HMDP in the mouse's bone structure, namely in the femurs, tail, spine, thorax cage and skull. Despite the lower image statistics (due to lower amount of radioactivity injected in the mouse) and the longer duration of the study, which made it even harder to control experimental conditions, the result once more demonstrates the high-resolution γ-imaging potential of the SiPM WSF gamma camera.

Figure 5.14: Whole mouse image obtained with Anger camera (GE 400AC), nearly 2 hours after injection of 250 μCi of ^{99m}Tc-HMDP.

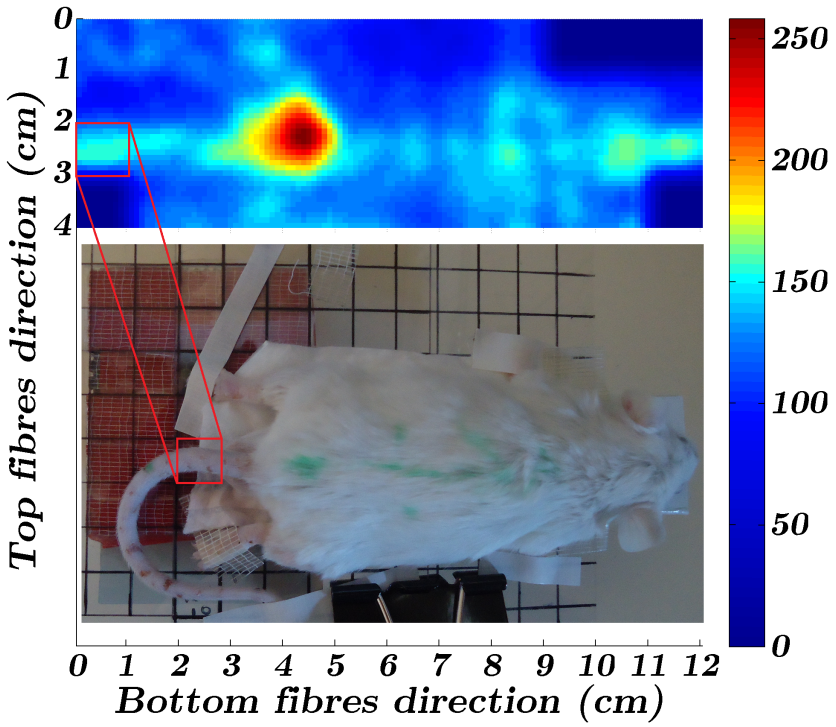

Figure 5.15: ^{99m}Tc-HMDP mouse image (12×4 cm^2) obtained from several 1 cm^2 scans with the SiPM WSF gamma camera prototype (darker squares were not acquired).

CHAPTER

6

SCALING UP TO A LARGER PROTOTYPE

A larger prototype of 100+100 SiPMs (10×10 cm^2) is being built, using the same principles of the small prototype developed, but scaled up by an order of magnitude in each direction, *i.e.*, with a total imaging area 100 times larger. Some components are identical to the ones used in the small prototype, such as the parallel-hole collimator, scintillator crystal, WSFs and SiPMs, which were simply scaled up in dimension or quantity. Other components, however, have been introduced or changed, such as the E-PMTs, power supplies or the electronic readout and data acquisition system, in order to optimise the camera's performance and be able to respond to the needs of power supply and electronic readout of a high number of individual channels. Furthermore, these changes allow the transition from a laboratory proof-of-concept prototype to a more autonomous final prototype with appropriate dimensions and weight for application in dedicated scintigraphy, namely in BSGI.

6.1 Components of the larger camera

6.1.1 Collimator

The collimator for the 10×10 cm^2 FOV camera was cut from the same large collimator as before, therefore it has the same physical characteristics of the collimator used in the small prototype (please see section 5.1.1). A photo of the 10×10 cm^2 collimator inserted in plastic and lead frames, used for mechanical support and further shielding, is shown in Figure 6.1.

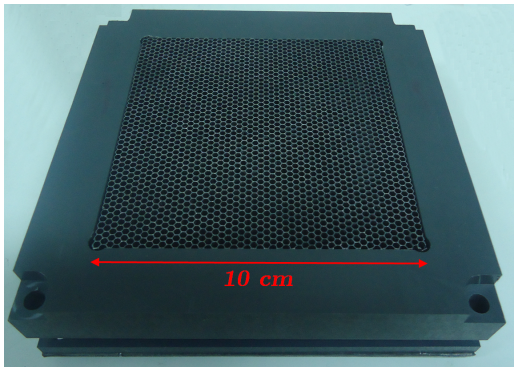

Figure 6.1: 10×10 cm^2 lead collimator.

6.1.2 Scintillator and WSFs

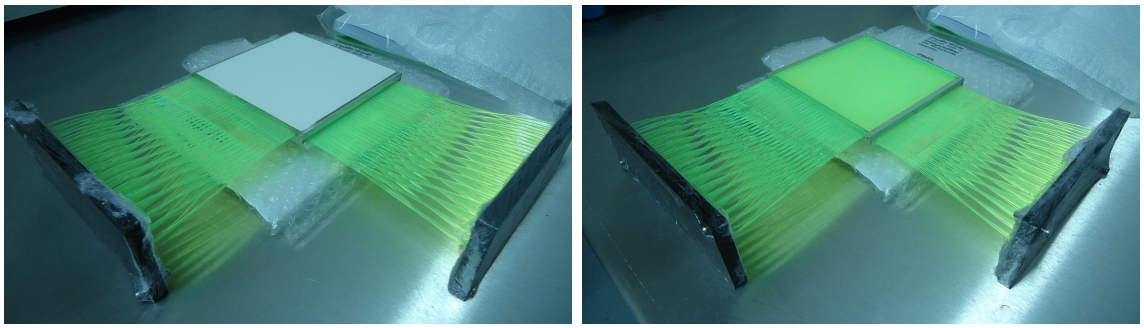

Figure 6.2: Photos of 10×10 cm^2 CsI(Na) crystal with embedded WSFs glued to SiPM coupling pieces. Left: top side with reflective surface. Right: bottom side with transparent glass window to be read out by energy PMTs

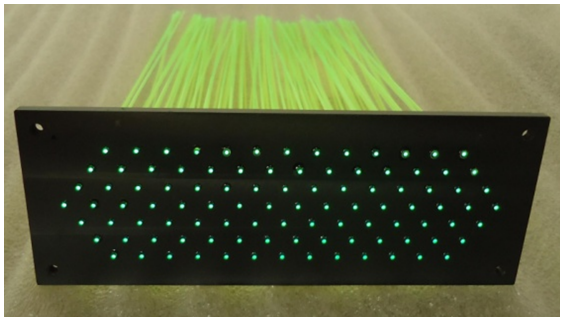

Figure 6.3: Intermediate piece with honeycomb-like hole distribution, used for coupling WSFs to SiPMs.

As with the small prototype, a custom production order was made for a $10\times10\times3$ cm^3 CsI(Na) crystal encapsulated with embedded WSFs, ∼22 cm long (Figure 6.2).

Using Epotek® 302-3M epoxy, the polished fibre ends were previously glued to plastic pieces with 1 mm holes for the fibres on one side and larger holes for the metal-packaged SiPMs on the other side. The holes have a honeycomb-like distribution (Figure 6.3), designed to provide the most compact coupling of the fibres to the SiPMs.

6.1.3 Readout electronics and data acquisition

The electronic control and readout system of the larger SiPM WSF gamma camera is composed of two main parts: firstly a series of interface boards and readout ASICs developed and assembled in cooperation with Professor Ian Cullum (England) and ISA S.A. (Coimbra, Portugal), and secondly a PC based X3-10M ADC board produced by Innovative Integration (California, U.S.A.). As in the small prototype, the trigger for the readout and digitisation sequence is given by the energy PMT signal in response to a scintillation event in the crystal. The E-PMT readout and trigger generation circuit is identical to the one developed for the small prototype, except that 4 PMTs and thus 4 channels are used and their outputs summed before connection to the comparator (please see section 6.1.5).

The readout of the 200 SiPMs is to be accomplished by 32-channel specialised front-end

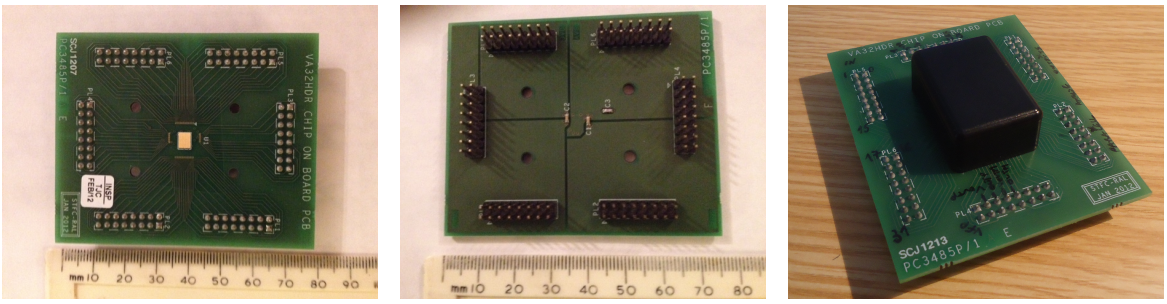

Figure 6.4: Photos of the ASIC daughter board (top, bottom and fully assembled views).

ASICs, four per detector side, each of which is fitted to a small daughter board (Figure 6.4). This method offers a simple way to cope with failure of a single ASIC, since it allows an easy replacement. Daughter boards were designed by Ian Cullum and produced at RAL (Rutherford Appleton Laboratory, England), including chip bonding.

Each ASIC channel consists of a charge sensitive preamplifier, a first order semi-Gaussian CR-RC shaper and a sample-and-hold unit. The output of all channels in each ASIC is connected to the inputs of a 32 channel multiplexer, whose output goes directly out of the chip via a differential output buffer. The eight ASICs used in the gamma camera can therefore read out up to 256 channels (at a maximum rate of 10 MHz) and output them in 8 differential analogue signals, which can then be digitised by the 8 channels of the X3-10M board and thus demultiplexed.

For each detector side, a SiPM front-end board has been developed to support the SiPMs, deliver the bias voltages provided by a SiPM power supply board (described in next section) to groups of SiPMs and break out their individual signals into 8×2 pin connectors. This board was designed in Aveiro and two boards were produced and assembled at ISA. Male connectors on the bottom side of the SiPM board attach directly to female connectors on a so called intermediate board, whose sole job is to route signals between the various boards making up the data acquisition system, *e.g.* to route the signals of the individual SiPMs from the SiPM board to the ASICs' inputs in the daughter boards (also attached to the intermediate board, as shown in Figure 6.5 right). Orange connectors carry SiPM bias voltages. Intermediate boards were designed by Ian Cullum and two units were produced and assembled at ISA.

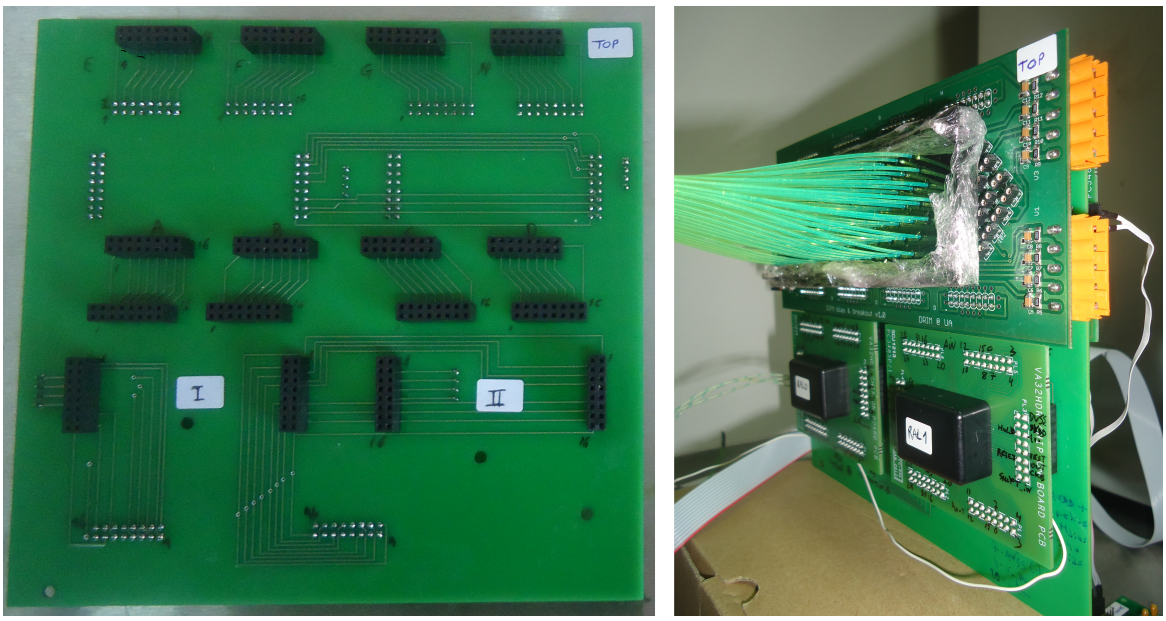

Figure 6.5: Photos of intermediate board used in each detector side - left: isolated; right: with attached SiPM board (front) and daughter boards (2 at the front and 2 at the back).

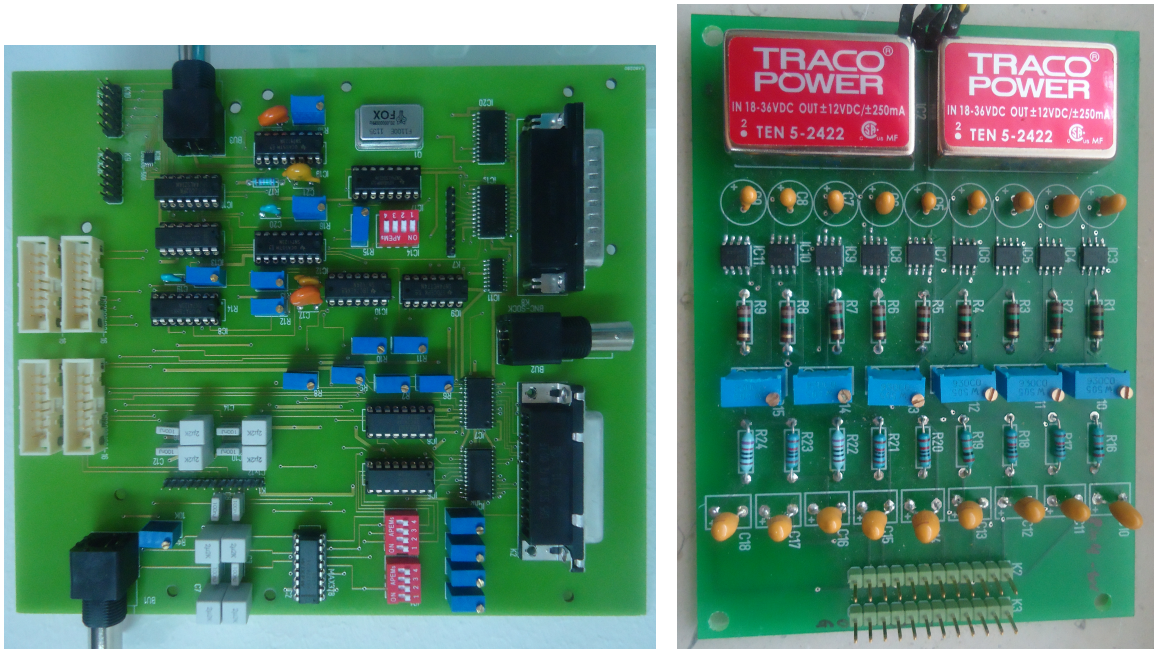

Figure 6.6: Photos of main control board (left) and voltage supply board (right) of electronic readout and data acquisition system.

One main board is responsible for the digital control and timing of the ASIC readout sequence, as well as for dealing with both analogue and digital interfacing to the X3-10M ADC board. The main board is connected directly to the two intermediate boards (one per detector side) through ribbon cables and to the X3-10M ultimately through MDR (mini delta ribbon) cables. The main board was designed by Ian Cullum and assembled at ISA.

X3-10M is an FPGA-based ADC board directly connected to a PC through a PCI-XMC

Figure 6.7: X3-10M board connected to PC, with cable connections for analogue inputs from readout ASICs (front) and digital inputs/outputs used for system control (rear).

adapter (Figure 6.7). It has 8 sampling channels of 16 bits, which can be flowed continuously and simultaneously at a maximum rate of 10 MHz, each used to digitise the output of a readout ASIC. Furthermore, it has a digital I/O port with 44 usable bits, accessible through a rear MDR-68 connector, which is used to control different parts of the system, such as the SiPM power supply boards, the main board and readout ASICs. A small PCB was assembled at the end of the MDR-68 cable to allow the connection of all the control signals from and to the X3-10M (22 of the 44 digital lines were necessary and programmed as required).

All connections between different boards were set up and the system tested. The current development stage has to do with troubleshooting of the main board circuits, so as to correctly synchronise the serial analogue outputs from the ASICs with the X3-10M digitisation, in terms of external trigger and clock signals. Several problems were encountered during testing and significant changes made to the original design of the main board, shown in Figure 6.6 (left).

In addition, a power supply board designed to provide the different low voltages necessary for all the system boards including the readout ASICs (Figure 6.6 right), needs to be repaired since its voltage outputs drop when connected to the main board. This is most likely due to a low current limitation of the voltage regulators used in the supply board (MAX663), which need to be replaced. The supply board was designed by Ian Cullum and produced by ISA. However, due to the above-mentioned problems, tests performed so far on the readout and acquisition system have been done using bench power supplies to replace it. Further troubleshooting is necessary in the main board and also in this power supply board, in order to complete the development of the readout and acquisition system, without which the full and autonomous operation of the larger camera has not yet been possible.

Data acquisition and imaging software

The X3-10M board comes with an example application (Snap), which was used as a base for the development of the software for data acquisition, system control and image reconstruction in the larger gamma camera prototype. The program for interaction with X3-10M is divided in two parts: graphical interface and board interaction. The former can be done in a large variety of development environments and languages, while the latter is done in C++. The development environment chosen for programming was Qt Creator, which allows the creation of a graphical user interface through the framework Qt®. Routines for FPGA programming, communication with the board and data acquisition were already created. Therefore, it was only necessary to determine the desired parameters for data acquisition through the 8 A/D channels and to create methods for the use of the digital I/O port (*e.g.* to control SiPM supply boards) and for image reconstruction, display and storage. Software development has been done in the context of this thesis with the cooperation of ISA, particularly of Eng. Miguel Ferreira. Since the main board hardware is not fully operational, a proper acquisition of the signals from the ASICs by the ADC board has not yet been possible, therefore the

software could not be tested in the real gamma camera setup yet. Nevertheless, the software was tested with signals from a pulse generator and lookup tables were implemented in order to correctly reconstruct a real-time image from the multiplexed inputs carrying the signals from the SiPMs reading out the WSFs. In addition, raw image data is saved in a file for later analysis.

6.1.4 SiPM power supplies

A power supply board was developed for the SiPMs, having 16 channels with a tunable output voltage approximately between 69 and 73 V. An 8-bit DAC (digital-to-analog converter) in each channel allows adjusting individual outputs with a step of about 15 mV. SiPM supply boards, with 16.5×10.5 cm^2, were designed and assembled by ISA and have been successfully tested in Aveiro (Figure 6.8). The plan is to use two of these boards in the SiPM WSF gamma camera, one per detector side. This allows biasing all the SiPMs in groups of 8 similar units, which means smaller groups than the ones used in the small prototype (of 10 units) and therefore should provide slightly more uniform results.

In collaboration with ISA, the control software for the two 16-channel SiPM power supply boards has been developed, including the automatic adjustment of the bias voltages in response to temperature changes. A tab in the graphical user interface (Figure 6.9) allows adjusting each of the 32 channels individually or simultaneously, using 14 digital outputs of the X3-10M board (7 digital lines are needed to control each SiPM supply board). The temperature is measured through a K thermocouple to be placed next to the SiPMs and

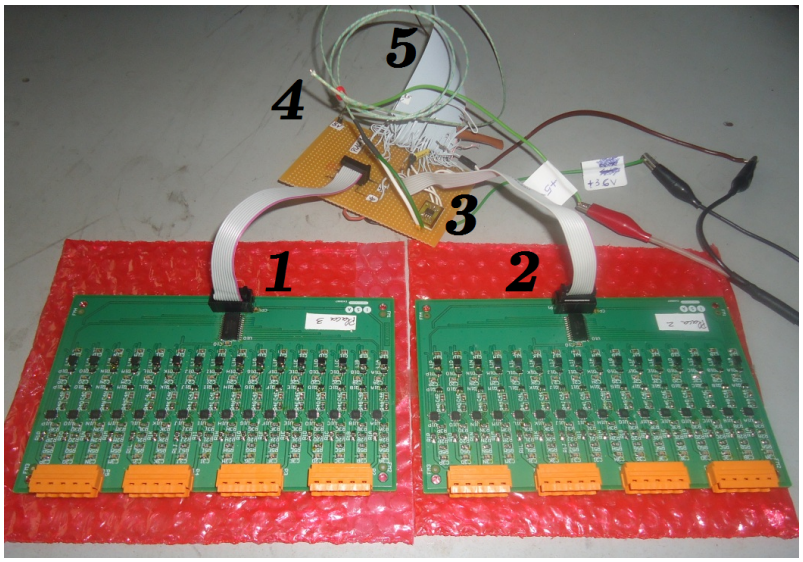

Figure 6.8: Two 16-channel SiPM power supply boards, with output voltages controlled by X3-10M. Legend: 1 and 2 - power supply boards (one per camera side), 3 - MAX31855, 4 - thermocouple, 5 - MDR-68 cable to X3-10M digital I/O port.

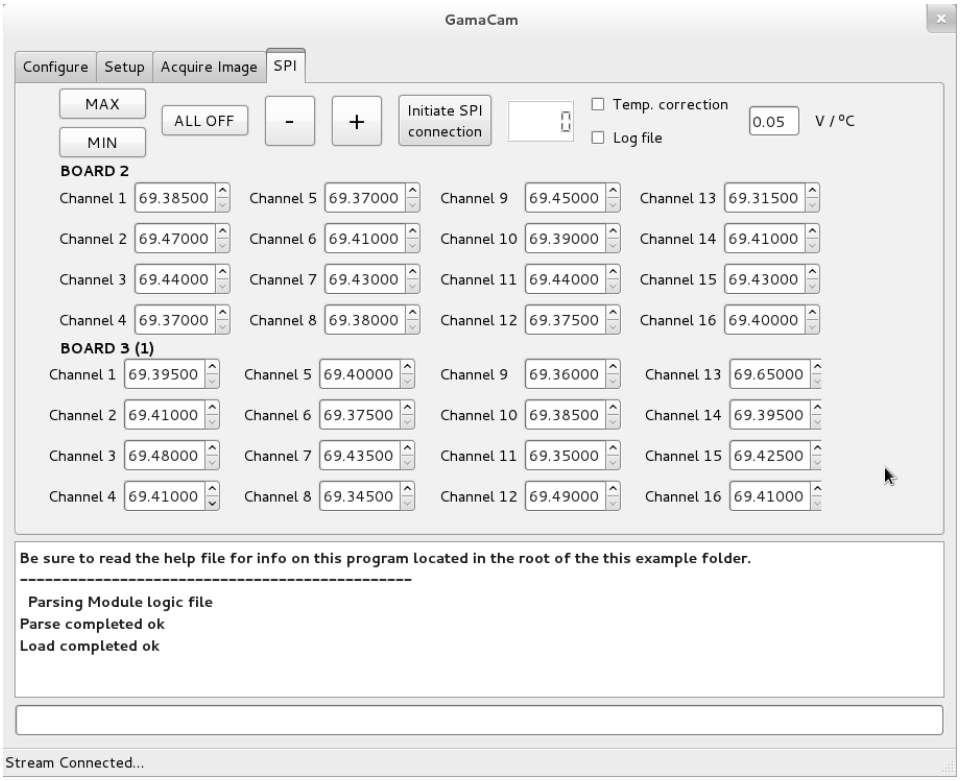

Figure 6.9: Screenshot of the data acquisition and imaging software GUI, showing the tab developed for SiPM bias voltage control with optional automatic temperature correction.

whose signal is sampled by a MAX31855 thermocouple-to-digital converter, with a resolution of 0.25°C. The output of this IC is sent to the X3-10M board via SPI (serial peripheral interface), *i.e.* using 3 digital lines, with the board being programmed to read the temperature at a given frequency (*e.g.* every five seconds) and allow the automatic adjustment of SiPM supply voltages. This adjustment is done according to the equation

$$V_{new} = V_{old} + \kappa \Delta T, \tag{6.1}$$

where ΔT is the temperature variation measured in each period and κ is the given temperature coefficient of SiPM reverse bias voltage (50 mV/°C according to Hamamatsu)[30].

6.1.5 E-PMTs

The energy signal of the larger prototype is given by 4 square PMTs with 60×60 mm^2 (Hamamatsu R6236), independently biased by 4 compact high-voltage modules (Hamamatsu C11152-51) regulated through external potentiometers and mounted on a PCB, specifically designed for this purpose (Figure 6.10). The potentiometers allow calibrating the position of the photopeak thus aligning the gains of the PMTs after similar amplification. The 4

Figure 6.10: Square PMTs used for the energy signal in the larger camera prototype (left) and PCB with their HV power supplies regulated by external potentiometers (right).

calibrated PMT signals are then summed by a non-inverting op-amp summing amplifier and the resulting energy signal is used as an input to a comparator circuit (identical to the one used in the small prototype) which generates a trigger signal (TTL or NIM logic), needed to initiate both ASIC readout and X3-10M acquisition.

A front-end readout PCB was built with the 4 E-PMT preamplifier and amplifier channels, together with the summing and comparator circuits. The board, shown in Figure 6.11, allows changing the RC constant of the initial charge preamplifier as well as the gain of the second amplifying stage, through the use of 2 potentiometers in each channel (blue components). Three additional potentiometers allow adjusting the comparator threshold and also the width and delay of the trigger signal.

This setup allowed testing the energy measuring part of the larger WSF gamma camera prototype, by digitising the summed energy signal (please see section 6.2.2). In order to digitise this analogue summed energy signal with the X3-10M board and apply digital energy

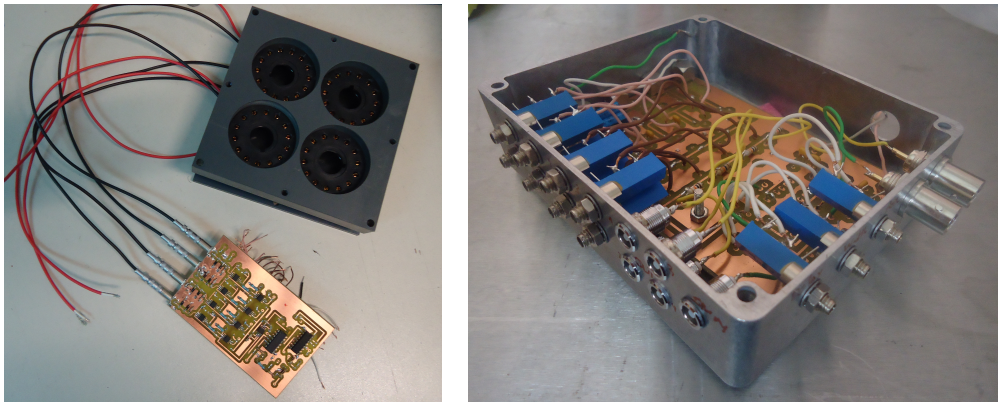

Figure 6.11: Front-end PCB to read out 4 E-PMTs and generate trigger from summed signal.

windowing, one of the board's 8 input channels has to be used for it. However, this is not desirable in the final prototype, since 8 ASICs are used and thus all the board's channels will be occupied. An alternative is to use 4 available ASIC channels to read out the 4 E-PMTs, digitise and demultiplex their signals together with the SiPM signals and then digitally sum them and apply energy windowing. In any case, the front-end E-PMT board is needed to generate the trigger signal for the main board and from there to the ASICs and X3-10M. Another alternative is not to digitise the energy signal with the X3-10M and apply analogue energy windowing, by optimising the trigger comparator circuit to include not only a low-level threshold but also a high-level one (*i.e.*, a single-channel analyser), such that all triggers generated and leading to ASIC readout and digitisation correspond to scintillation events within the desired energy window.

6.1.6 Mechanical structure

An internal mechanical structure has been designed and built for the 10×10 cm^2 SiPM WSF gamma camera prototype. Several plastic parts were produced to support the collimator, the crystal with embedded fibres, the 4 E-PMTs and their power supplies, mounted on a PCB located underneath. These parts are held together by 4 threaded rods, 25 cm long, using aluminium tube spacers and nuts, as shown in Figure 6.12. Additionally, two aluminium plates were produced to support the WSF-SiPM coupling pieces in each side.

A light-tight enclosure with a support structure for all the remaining PCBs is necessary. The cable connections needed between the gamma camera head and the outside are only the

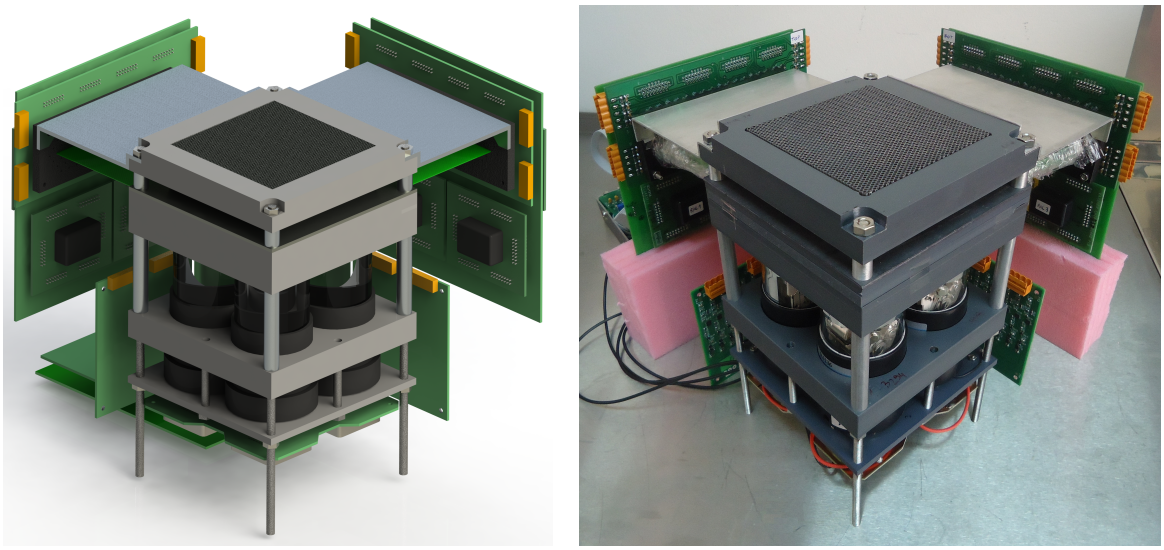

Figure 6.12: Solidworks® CAD drawing (left) and photo (right) of the internal structure designed and built for the 10×10 cm^2 SiPM WSF gamma camera prototype (all components drawn to scale).

two MDR cables to the X3-10M board and a ±18 V connection from an outside power supply, required by the main supply board to deliver all the system low voltages. A platform trolley to have the PC and a mechanical arm are also envisaged for a clinical prototype.

6.1.7 Temperature cooling system

As shown in the previous chapters, SiPM performance is very much affected by temperature, particularly in terms of dark noise, gain and photon detection efficiency. A higher operating temperature means a lower gain for a fixed voltage and a higher level of dark pulses, having a great influence in the results obtained with the SiPM WSF gamma camera prototype, because we are dealing with a very low number of photons and we need to integrate the SiPM signal for a relatively long time. During this integration time, it is desirable to have the minimum dark pulses possible, and the solution to achieve that while keeping a high gain and PDE, is to lower the temperature. Therefore, the inclusion of a temperature cooling system in the camera was naturally considered.

The most effective way to homogeneously lower the temperature of the 200 SiPMs would be through a cooling system with circulating fluid to cool down the pieces into which the SiPMs are coupled, which would then have to be larger and made of copper or aluminium, instead of nylon. This would require the acquisition of a thermoelectric cooler with customised cold plates, as well as tubes, fittings and accessories which would always have to accompany the gamma camera.

As this introduces a great level of complexity, design changes and costs, going against the key objectives of overall cost-efficiency and simplicity for a new WSF gamma camera design, the idea of applying such a temperature cooling system was not materialised. For the sake of simplicity, it was preferred to rely on a controlled and stable room temperature, as low as possible, and use the temperature monitoring and SiPM bias voltage correction system developed.

6.2 Characterisation

6.2.1 Size and weight

The weight of the gamma camera head, supported by the internal mechanical structure just described, is approximately 7 kg, including all the PCBs necessary and components developed so far. This excludes the PC and X3-10M ADC board, as well as any external enclosure and surrounding shielding, but includes the collimator and lead frame around it.

An external enclosure to contain the gamma camera head and associated electronics should have the approximate size of a cube with sides of length 30 cm, accounting for some free space which can be used to place air extracting fans or other additional components.

6.2.2 Energy resolution and uniformity

The energy measuring part of the larger SiPM WSF gamma camera prototype was characterised using the collimated ^{57}Co source (Figure 4.16) and the setup described in section 6.1.5, composed of four Hamamatsu R6236 PMTs, respective individual high-voltage supplies and common amplifier board developed. Optical grease was used to couple the PMTs to the crystal.

Even though the X3-10M board was successfully used to digitise the energy signal using the TTL external trigger given by the amplifier board after conversion to low-voltage TTL in the main board, the summed signal from the 4 PMTs was fed to a multi-channel analyser (Amptek MCA8000A), which requires no external trigger.

The individual gain of the 4 E-PMTs after similar amplification was previously calibrated, by adjusting the supply voltages with the external potentiometers so that the position of the 122 keV photopeak was the same in each PMT's spectrum when the ^{57}Co source was aligned with its centre. Examples of spectra obtained from the summed signal after calibration, with the source positioned over the centre of each PMT, are shown in Figure 6.13.

The uniformity of the energy resolution was measured, by scanning the ^{57}Co source over the whole 10×10 cm^2 FOV, performing 3 independent acquisitions at each position. Averaged results are presented in Figure 6.14. A best energy resolution of about 19.3% FWHM was achieved at 122 keV, for positions between the centre of each PMT and the centre of the 4 units. One should notice that the centre of each PMT does not correspond to the centre of each quadrant of the 10×10 cm^2 crystal, since the total area of the 4 PMTs is 12×12 cm^2. Therefore, the outer cm of the square PMTs is not covered by the crystal.

Energy resolution values naturally degrade a few % in the borders between PMTs and more pronouncedly in the exterior borders and corners. Nevertheless, the values are quite uniform within the crystal area that excludes 5 mm from the edges, with an average of 20.37% and standard deviation of 0.695% for the measurements performed.

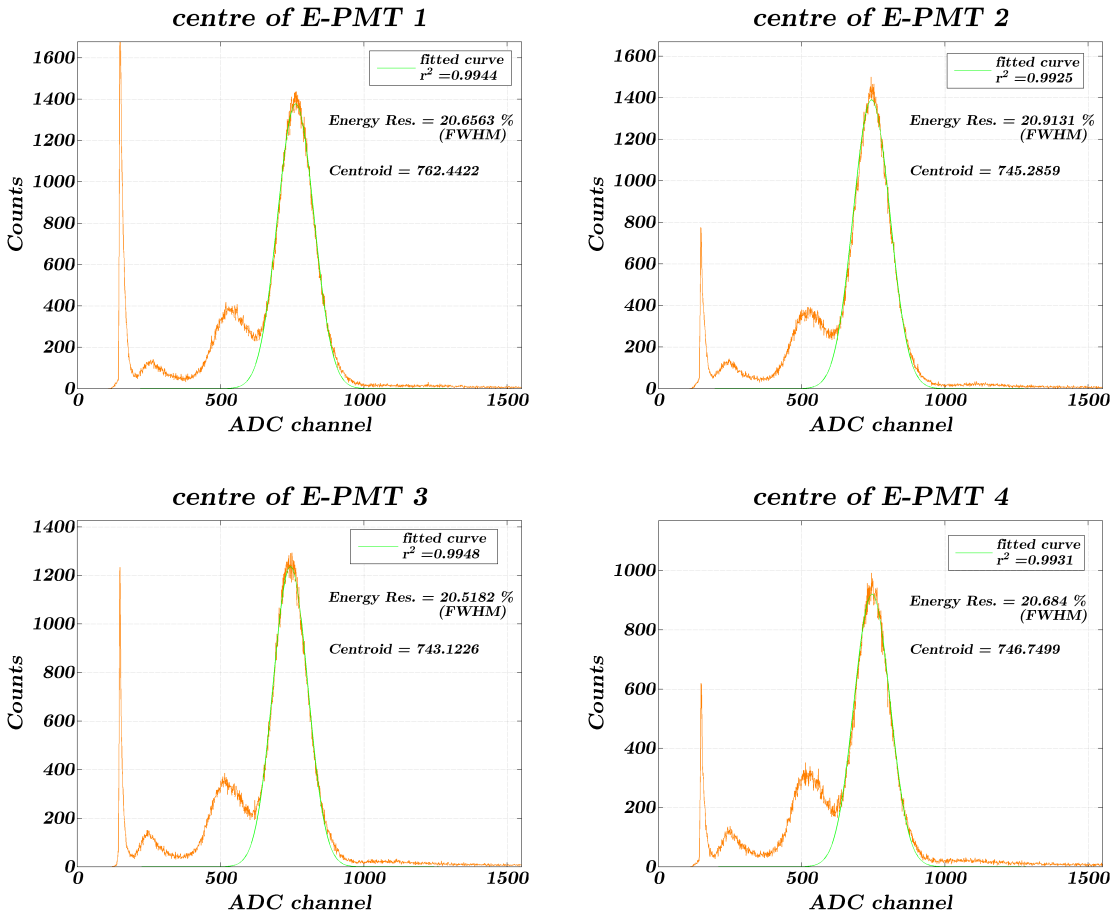

Figure 6.13: ^{57}Co energy spectra obtained with the 10×10 cm^2 CsI(Na) crystal with embedded WSFs read out by 4 PMTs, for different positions of the source.

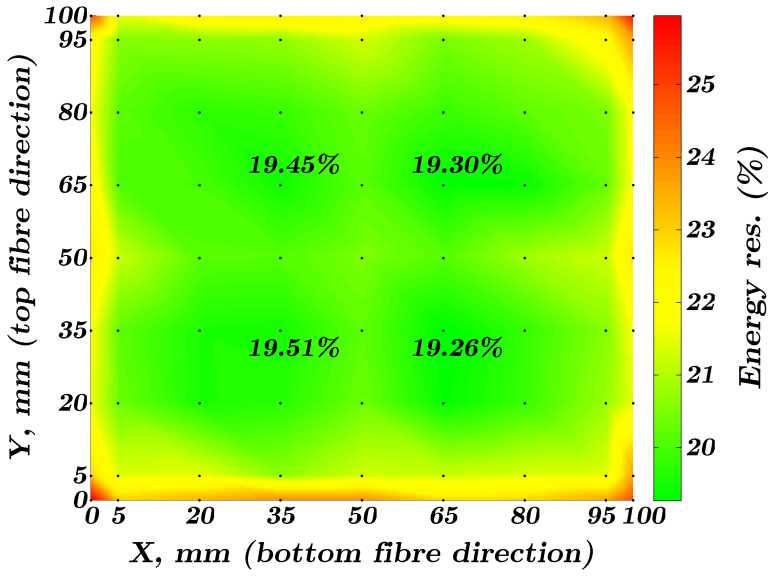

Figure 6.14: Energy resolution map for the 10×10 cm^2 prototype, using ^{57}Co (122 keV). Dots represent positions of experimental measurements. Remaining values are interpolated.

CHAPTER

7

CONCLUSIONS AND FUTURE WORK

7.1 Conclusions

The development of small FOV gamma cameras dedicated to small organs and specific applications like breast-specific gamma imaging has been essential to overcome the limitations of general purpose Anger cameras in such applications. Unlike these bulky devices, compact cameras can be positioned in direct contact with the breast, avoid background emission and acquire mammography-like projections, being much more effective in the early detection of small tumours and reduction of unnecessary biopsies. Due to these proven benefits, the use of BSGI is already recommended as an adjunct modality to mammography, particularly for cases where mammography has lower sensitivity. The best performances of commercial breast-dedicated gamma cameras have been obtained with CZT-based cameras, which are however rather expensive. For instance [137], a single-detector version of Lumagem® camera has a commercial value of about 250.000 € and a dual-headed model about 430.000 €.

Based on evidence from the previous work of Soares *et al.*, this thesis describes the development of a wavelength-shifting fibre gamma camera applying recently available silicon photomultipliers as the photodetectors used for positioning. The design of the WSF gamma camera is very flexible allowing the coverage of different imaging areas and the development of compact cameras with only a few mm of dead space at the edges, an important feature to allow the detection of deep breast tumours by placing the camera directly against the chest wall. The concept has the advantage of using N+N instead of N×N photodetectors to cover an identical imaging area, and was applied for the first time using SiPMs.

The main advantage of SiPMs over previously applied MaPMTs is their higher photon detection efficiency, about 3 times higher at the wavelength of re-emission of the WSFs, therefore an improvement of the camera's intrinsic spatial resolution was expected, from 3-4 mm to less than 2 mm FWHM. Moreover, because they don't require high voltages, SiPMs allow building a less power consuming compact camera, aimed for breast imaging.

However, the main drawback of SiPMs is their thermal noise, which at room temperature consists of about half a million pulses per second, undistinguishable from photon-generated pulses. Even though the majority of SiPM dark pulses has an amplitude equivalent to a pulse generated by one or two G-APD firing cells, higher amplitude dark pulses also occur. Dark pulses affect the efficiency of WSF readout, particularly considering that only about 10 to 15 photons are expected at the end of the fibres, for a 140 keV interaction. Nevertheless, the simulation of the image of a ^{99m}Tc point source with a SiPM WSF gamma camera indicated that a spatial resolution around 1 mm FWHM is possible, despite the effects of dark pulses.

A prototype CsI(Na)-WSF-SiPM gamma camera with 10×10 mm^2 was assembled and tested, including the development of customised readout electronics and software and final integration of all components. This system has shown to be capable of high resolution gamma imaging. An average intrinsic spatial resolution of approximately 3 mm FWHM for the 122

keV of ^{57}Co and nearly 2 mm FWHM for the 140 keV of ^{99m}Tc was measured, which is comparable or superior to the performance of modern Anger cameras. However, spatial resolution is below the best expectations from simulation. This is because, in practice, SiPM signals had to be shaped and integrated for a longer time than expected, integrating also more noise, and therefore the impact of dark noise was underestimated by simulation. In addition, simulation did not consider the non-uniformity of SiPM response.

Good position linearity was observed only after calibration, which needs to be performed prior to imaging acquisitions, to compensate for the differences between individual SiPMs. Very important is also a bias voltage adjustment during acquisitions, to compensate for the temperature sensitivity of these photodetectors. Nevertheless, positioning results are satisfactory, especially considering the possible improvements, namely in the optimisation of readout electronics and ADC triggering, calibration method, reduction of the operating temperature or individualisation of SiPM bias voltages. The great potential of this technology was finally demonstrated by a pre-clinical imaging test of a mouse injected with ^{99m}Tc-HMDP, where the images resulting from several scans with the small FOV prototype compared favourably to the ones obtained by a conventional large FOV Anger camera, despite all the experimental limitations of the method and possible optimisations in the system.

An energy resolution of 23% for 122 keV and 21% for 140 keV γ-photons has been measured with the small prototype. A better performance was observed with ^{99m}Tc, both in energy and spatial resolutions, due to the higher number of scintillation photons. The worse energy resolution comparatively to a conventional gamma camera is explained by the presence of the fibres between the scintillator and the energy PMT, which absorb a fraction of the scintillation photons.

A larger prototype with a FOV of 10×10 cm^2 was assembled using 100+100 SiPMs and 4 energy PMTs, having demonstrated an average energy resolution of 20% FWHM at 122 keV. The better performance compared to the smaller prototype can be explained by the larger and more efficient PMTs used. Despite being poor when compared to the best energy resolutions obtained with modern Anger cameras (∼9-10%) or state-of-the-art CZT cameras (∼5%), an energy resolution under 20% at 140 keV is considered acceptable, specially taking into account that a compact WSF gamma camera can be positioned close to the object and avoid a great part of scattered photons. The advantages of a more favourable field-of-view and proximity partially compensate the inferior energy resolution.

Most of the hardware and software for the larger prototype has been developed and successfully tested, with the exception of some parts of the main control board of the readout and acquisition system. The use of the developed system for temperature monitoring and automated SiPM bias voltage correction, as well as of the more stable and less power-dissipating ASIC readout (105 mW each chip), is expected to improve the uniformity of positioning results. However, a significant improvement in spatial resolution, to levels comparable to

state-of-the-art dedicated gamma cameras, can only be reached through a temperature reduction. A cooling system capable of keeping a low and stable operation temperature for all the SiPMs would improve their PDE and lower dark noise contribution significantly.

The production cost of a SiPM WSF gamma camera, even including a cooling system, is relatively inexpensive when compared to Anger cameras or breast-specific gamma imagers. Furthermore, the cost of SiPMs has dropped considerably in the last years, paving the way for the development of an even more competitive system. This is due to the many developments from different research institutes and manufacturers, as well as to the mass production of SiPMs for several applications such as high-energy physics experiments. An estimate for the total cost of the components that make up a 10×10 cm^2 camera, based on the price of all components including the temperature cooling system considered in 6.1.7, is around 20.000-25.000€ .

7.2 Future Work

Future work is needed to have a fully functional 10×10 cm^2 prototype, which can then be completely characterised and clinically applied. Unfortunately, due to delays in the production and delivery of several parts of the main readout electronics system (*e.g.* daughter boards with bonded ASICs), whose final integration requires significant troubleshooting and development work, it wasn't possible to finish the development of the large gamma camera prototype in useful time.

In parallel to the development of this 10×10 cm^2 prototype, even though not presented in this thesis, a similar prototype with a FOV of 12×12 cm^2 and using two 64-anode MaPMTs to read out 120 WSFs in each direction, has been also under development. The development of this MaPMT prototype is at the same stage as the one presented, *i.e.* it is only dependent on the completion of the readout and data acquisition system, which is identical. It would be very interesting to compare the performance of both prototypes, as soon as the whole readout system can be fully operational.

REFERENCES

[1] J. Cal-Gonzalez et al., "*Positron Range Effects in High Resolution 3D PET Imaging*", 2009 IEEE Nuclear Science Symposium Conference Record, Vols 1-5, pp. 2788-2791, 2009.

[2] M. M. Alauddin, "*Positron emission tomography (PET) imaging with (18)F-based radiotracers*", Am J Nucl Med Mol Imaging, vol. 2, no. 1, pp. 55-76, 2012.

[3] M. Conti, "*State of the art and challenges of time-of-flight PET*", Phys Med, vol. 25, no. 1, pp. 1-11, 2009.

[4] T. K. Lewellen, "*Recent developments in PET detector technology*", Physics in Medicine and Biology, vol. 53, no. 17, pp. R287-317, 2008.

[5] J. L. Humm, A. Rosenfeld and A. Del Guerra, "*From PET detectors to PET scanners*", Eur J Nucl Med Mol Imaging, vol. 30, no. 11, pp. 1574-97, 2003.

[6] P. Zanzonico, "*Positron emission tomography: a review of basic principles, scanner design and performance, and current systems*", Seminars in Nuclear Medicine, vol. 34, no. 2, pp. 87-111, 2004.

[7] F. Bray et al., "*Global estimates of cancer prevalence for 27 sites in the adult population in 2008*", International Journal of Cancer, vol. 132, no. 5, pp. 1133-1145, 2013.

[8] M. Malvezzi et al., "*European cancer mortality predictions for the year 2013*", Annals of Oncology, vol. 24, no. 3, pp. 792-800, 2013.

[9] A. Jemal et al., "*Cancer statistics, 2008*", CA Cancer J Clin, vol. 58, no. 2, pp. 71-96, 2008.

[10] N. F. Boyd et al., "*Mammographic density and the risk and detection of breast cancer*", N Engl J Med, vol. 356, no. 3, pp. 227-36, 2007.

[11] M. Pollan et al., "*Mammographic density and risk of breast cancer according to tumor characteristics and mode of detection: a Spanish population-based case-control study*", Breast Cancer Res, vol. 15, no. 1, pp. R9, 2013.

[12] J. G. Elmore et al., "*Ten-year risk of false positive screening mammograms and clinical breast examinations*", N Engl J Med, vol. 338, no. 16, pp. 1089-96, 1998.

[13] O. Schillaci et al., "*Clinical utility of scintimammography: From the Anger-camera to new dedicated devices*", Nuclear Instruments & Methods in Physics Research Section A - Accelerators Spectrometers Detectors and Associated Equipment, vol. 569, no. 2, pp. 281-285, 2006.

[14] R. F. Brem et al., "*Breast-specific gamma imaging as an adjunct imaging modality for the diagnosis of breast cancer*", Radiology, vol. 247, no. 3, pp. 651-7, 2008.

[15] "*The Supply of Medical Radioisotopes: Review of Potential Molybdenum-99/Technetium-99m Production Technologies*", Nuclear Energy Agency - Organisation for Economic Co-operation and Development, 2010.

[16] Online database of radionuclide decay data, www.nucleide.org/DDEP-WG/DDEPdata.htm. Access date: March, 2013.

[17] G. B. Saha, "*Physics and radiobiology of nuclear medicine*", Springer, 3rd ed., 2006.

[18] I. Khalkhali et al., "*Procedure guideline for breast scintigraphy. Society of Nuclear Medicine*", J Nucl Med, vol. 40, no. 7, pp. 1233-5, 1999.

[19] S. J. Goldsmith et al., "*SNM practice guideline for breast scintigraphy with breast-specific gamma-cameras 1.0*", J Nucl Med Technol, vol. 38, no. 4, pp. 219-24, 2010.

[20] H. O. Anger, "*Scintillation Camera*", Review of Scientific Instruments, vol. 29, no. 1, pp. 27-33, 1958.

[21] J. Prekeges, "*Nuclear medicine instrumentation*", Jones & Bartlett Learning, 2nd ed., 2013.

[22] "*Efficiency calculations for selected scintillators*", Technical information note, Saint-Gobain Crystals, 2004.

[23] T. E. Peterson and L. R. Furenlid, "*SPECT detectors: the Anger Camera and beyond*", Physics in Medicine and Biology, vol. 56, no. 17, pp. R145-R182, 2011.

[24] C. W. E. Eijk, "*Inorganic-scintillator development*", Nuclear Instruments & Methods in Physics Research Section A - Accelerators Spectrometers Detectors and Associated Equipment, vol. 460, no. 1, pp. 1-14, 2001.

[25] R. Y. Zhu, "*Crystal Calorimeters in the Next Decade*", 2009 IEEE Nuclear Science Symposium Conference Record, Vols 1-5, pp. 2238-2244, 2009.

[26] M. Moszynski et al., "*Absolute light output of scintillators*", IEEE Transactions on Nuclear Science, vol. 44, no. 3, pp. 1052-1061, 1997.

[27] H. T. Dam et al., "*Optical Absorption Length, Scattering Length, and Refractive Index of LaBr3:Ce3+*", IEEE Transactions on Nuclear Science, vol. 59, no. 3, pp. 656-664, 2012.

[28] J. T. M. Haas and P. Dorenbos, "*Advances in yield calibration of scintillators*", IEEE Transactions on Nuclear Science, vol. 55, no. 3, pp. 1086-1092, 2008.

[29] List of measured scintillation properties of innorganic materials, administered by Stephen Derenzo, Lawrence Berkeley National Laboratory, http://scintillator.lbl.gov/. Access date: March, 2013.

[30] Hamamatsu Photonics K.K., Japan, www.hamamatsu.com.

[31] K. Nakamura et al., "*Latest bialkali photocathode with ultra high sensitivity*", Nuclear Instruments & Methods in Physics Research Section A - Accelerators Spectrometers Detectors and Associated Equipment, vol. 623, no. 1, pp. 276-278, 2010.

[32] E. K. Papanastassiou et al., "*The variation of intrinsic spatial resolution across the UFOV of scintillation cameras*", Computerized Medical Imaging and Graphics, vol. 30, no. 8, pp. 417-426, 2006.

[33] M. Ricard, "*Imaging of gamma emitters using scintillation cameras*", Nuclear Instruments & Methods in Physics Research Section A - Accelerators Spectrometers Detectors and Associated Equipment, vol. 527, no. 1-2, pp. 124-129, 2004.

[34] N. J. Bird, S. E. Old and R. W. Barber, "*Gamma camera positron emission tomography*", British Journal of Radiology, vol. 74, no. 880, pp. 303-306, 2001.

[35] M. N. Wernick and J. N. Aarsvold, "*Emission tomography: the fundamentals of PET and SPECT*", Elsevier, 2004.

[36] R. Taillefer, "*Clinical applications of ^{99m}Tc-sestamibi scintimammography*", Seminars in Nuclear Medicine, vol. 35, no. 2, pp. 100-15, 2005.

[37] C. B. Hruska and M. K. O'Connor, "*CZT detectors: How important is energy resolution for nuclear breast imaging*", Physica Medica, vol. 21, pp. 72-75, 2006.

[38] C. B. Hruska and M. K. O'Connor, "*A Monte Carlo model for energy spectra analysis in dedicated nuclear breast imaging*", IEEE Transactions on Nuclear Science, vol. 55, no. 1, pp. 491-500, 2008.

[39] A. J. Soares et al., "*Development of a compact wavelength-shifting fibre gamma camera*", IEEE Transactions on Nuclear Science, vol. 47, no. 3, pp. 1058-1064, 2000.

[40] W. Worstell et al., "*Scintillator crystal readout with wavelength-shifting optical fibers*", Nuclear Science Symposium & Medical Imaging Conference - 1994 IEEE Conference Record, Vols 1-4, pp. 1869-1873, 1994.

[41] D. Michael, "*The MINOS experiment*", Progress in Particle and Nuclear Physics, Vol 48 No 1, vol. 48, no. 1, pp. 99-109, 2002.

[42] E. Tarkovsky, "*The HERA-B electromagnetic calorimeter*", Nuclear Instruments & Methods in Physics Research Section A - Accelerators Spectrometers Detectors and Associated Equipment, vol. 379, no. 3, pp. 515-517, 1996.

[43] V. Hagopian, "*The Hadron Calorimeter of the compact muon solenoid (CMS)*", Nuclear Physics B, pp. 47-51, 1998.

[44] D. J. Herbert et al., "*A compact PET detector array using wavelength shifting fibres*", 1999 IEEE Nuclear Science Symposium - Conference Record, Vols 1-3, 1999.

[45] E. Bolle et al., "*AX-PET: A novel PET concept with G-APD readout*", Nuclear Instruments & Methods in Physics Research Section A - Accelerators Spectrometers Detectors and Associated Equipment, vol. 695, pp. 129-134, 2012.

[46] A. J. Soares, "*Development of a compact high resolution gamma camera*", PhD thesis, University College London, 2001.

[47] G. F. Knoll, "*Radiation detection and measurement*", John Wiley & Sons, 4th ed., 2010.

[48] Saint-Gobain Crystals scintillating optical fiber brochure, http://www.detectors.saint-gobain.com/fibers.aspx. Access date: June, 2013.

[49] A. Gomes et al., "*Comparative study of WLS fibres for the ATLAS tile calorimeter*", Nuclear Physics B, pp. 106-111, 1998.

[50] C. P. Achenbach, J. H. Cobb and D. Wahl, "*Development of a compact scintillator hodoscope with wavelength-shifting fibre read-out*", Nuclear Instruments & Methods in

Physics Research Section A - Accelerators Spectrometers Detectors and Associated Equipment, vol. 539, no. 1-2, pp. 112-124, 2005.

[51] F. Quarati et al., "*X-ray and gamma-ray response of a 2 " x 2 " LaBr3 : Ce scintillation detector*", Nuclear Instruments & Methods in Physics Research Section A - Accelerators Spectrometers Detectors and Associated Equipment, vol. 574, no. 1, pp. 115-120, 2007.

[52] R. Pani et al., "*LaBr3(Ce) and NaI(Tl) Performance Comparison for Single Photon Emission Imaging*", 2011 IEEE Nuclear Science Symposium and Medical Imaging Conference (NSS/MIC), pp. 4433-4436, 2011.

[53] A. J. Soares et al., "*Development of a small gamma camera using wavelength-shifting fibres coupled to inorganic scintillation crystals for imaging 140 keV gamma rays*", IEEE Transactions on Nuclear Science, vol. 46, no. 3, pp. 576-582, 1999.

[54] F. Scopinaro et al., "*High-resolution scintimammography improves the accuracy of technetium-99m methoxyisobutylisonitrile scintimammography: use of a new dedicated gamma camera*", European Journal of Nuclear Medicine, vol. 26, no. 10, pp. 1279-88, 1999.

[55] Y. Sun et al., "*Clinical usefulness of breast-specific gamma imaging as an adjunct modality to mammography for diagnosis of breast cancer: a systemic review and meta-analysis*", Eur J Nucl Med Mol Imaging, vol. 40, no. 3, pp. 450-463, 2013.

[56] R. F. Brem et al., "*Invasive lobular carcinoma: detection with mammography, sonography, MRI, and breast-specific gamma imaging*", AJR Am J Roentgenol, vol. 192, no. 2, pp. 379-83, 2009.

[57] J. Prekeges, "*Breast imaging devices for nuclear medicine*", J Nucl Med Technol, vol. 40, no. 2, pp. 71-8, 2012.

[58] R. F. Brem, M. Fishman and J. A. Rapelyea, "*Detection of ductal carcinoma in situ with mammography, breast specific gamma imaging, and magnetic resonance imaging: a comparative study*", Acad Radiol, vol. 14, no. 8, pp. 945-50, 2007.

[59] T. D. Milster et al., "*A Modular Scintillation Camera for Use in Nuclear-Medicine*", IEEE Transactions on Nuclear Science, vol. 31, no. 1, pp. 578-580, 1984.

[60] Y. Yoshizawa and J. Takeuchi, "*The latest vacuum photodetector*", Nuclear Instruments & Methods in Physics Research Section A - Accelerators Spectrometers Detectors and Associated Equipment, vol. 387, no. 1-2, pp. 33-37, 1997.

[61] F. Cusanno et al., "*Preliminary evaluation of compact detectors for hand-held gamma cameras*", Physica Medica, vol. 20, no. 2, pp. 65-70, 2004.

[62] R. Pani et al., "*Scintillating array gamma camera for clinical use*", Nuclear Instruments & Methods in Physics Research Section A - Accelerators Spectrometers Detectors and Associated Equipment, vol. 392, no. 1-3, pp. 295-298, 1997.

[63] R. Pani et al., "*Dedicated gamma camera for single photon emission mammography (SPEM)*", 1997 IEEE Nuclear Science Symposium - Conference Record, Vols 1 & 2, pp. 1615-1619, 1998.

[64] R. Pani et al., "*Multi-PSPMT scintillation camera*", IEEE Transactions on Nuclear Science, vol. 46, no. 3, pp. 702-708, 1999.

[65] R. Pani et al., "*Compact large FoV gamma camera for breast molecular imaging*", Nuclear Instruments & Methods in Physics Research Section A - Accelerators Spectrometers Detectors and Associated Equipment, vol. 569, no. 2, pp. 255-259, 2006.

[66] R. Pani et al., "*LaBr3 : Ce scintillation gamma camera prototype for X and gamma ray imaging*", Nuclear Instruments & Methods in Physics Research Section A - Accelerators Spectrometers Detectors and Associated Equipment, vol. 576, no. 1, pp. 15-18, 2007.

[67] R. Pani et al., "*Investigation on a small FoV gamma camera based on LaBr(3):Ce continuous crystal*", Nuclear Physics B - Proceedings Supplements, vol. 197, pp. 202-205, 2009.

[68] M. B. Williams et al., "*Performance of a PSPMT based detector for scintimammography*", Physics in Medicine and Biology, vol. 45, no. 3, pp. 781-800, 2000.

[69] S. Majewski et al., "*Optimization of dedicated scintimammography procedure using detector prototypes and compressible phantoms*", IEEE Transactions on Nuclear Science, vol. 48, no. 3, pp. 822-829, 2001.

[70] S. Majewski et al., "*Optimization of a mini-gamma camera based on a 2 x 2 array of Hamamatsu H8500 PSPMTs*", Nuclear Instruments & Methods in Physics Research Section A - Accelerators Spectrometers Detectors and Associated Equipment, vol. 569, no. 2, pp. 215-219, 2006.

[71] M. J. More et al., "*Evaluation of gamma cameras for use in dedicated breast Imaging*", IEEE Transactions on Nuclear Science, vol. 53, no. 5, pp. 2675-2679, 2006.

[72] R. Pani, "*Potentialities and present status of LaBr3:Ce scintillation crystals for nuclear medicine imaging*", presented at the Workshop On Developments of new Scintillator Detectors for Gamma Spectroscopy and Imaging, Milano, Italy, November 2009., .

[73] M. J. More et al., "*Limited angle dual modality breast imaging*", IEEE Transactions on Nuclear Science, vol. 54, no. 3, pp. 504-513, 2007.

[74] M. B. Williams et al., "*Dual-Modality Breast Tomosynthesis*", Radiology, vol. 255, no. 1, pp. 191-198, 2010.

[75] S. Majewski et al., "*Phantom evaluations of a dedicated dual-head scintimammography system*", Phys Med, vol. 21 Suppl 1, pp. 35-8, 2006.

[76] P. G. Judy et al., "*Molecular breast imaging with directly opposing compact gamma cameras*", 2007 IEEE Nuclear Science Symposium Conference Record, Vols 1-11, pp. 4040-4043, 2007.

[77] F. Garibaldi et al., "*A novel high resolution and high efficiency dual head detector for molecular breast imaging: New results from clinical trials*", Nuclear Instruments & Methods in Physics Research Section A - Accelerators Spectrometers Detectors and Associated Equipment, vol. 617, no. 1-3, pp. 227-229, 2010.

[78] F. Sanchez et al., "*Design and tests of a portable mini gamma camera*", Med Phys, vol. 31, no. 6, pp. 1384-1397, 2004.

[79] F. Sanchez et al., "*Performance tests of two portable mini gamma cameras for medical applications*", Med Phys, vol. 33, no. 11, pp. 4210-20, 2006.

[80] P. D. Olcott et al., "*Performance characterization of a miniature, high sensitivity gamma ray camera*", IEEE Transactions on Nuclear Science, vol. 54, no. 5, pp. 1492-1497, 2007.

[81] S. Yamamoto et al., "*Development of a compact and high spatial resolution gamma camera system using LaBr3(Ce)*", Nuclear Instruments & Methods in Physics Research Section A - Accelerators Spectrometers Detectors and Associated Equipment, vol. 622, no. 1, pp. 261-269, 2010.

[82] J. A. Neves and C. Collaboration, "*The ClearPEM breast imaging scanner*", Nuclear Instruments & Methods in Physics Research Section A - Accelerators Spectrometers Detectors and Associated Equipment, vol. 628, no. 1, pp. 444-447, 2011.

[83] V. Schulz et al., "*SiPM based preclinical PET/MR Insert for a human 3T MR: first imaging experiments*", 2011 IEEE Nuclear Science Symposium and Medical Imaging Conference (NSS/MIC), pp. 4467-4469, 2011.

[84] G. Delso et al., "*Performance Measurements of the Siemens mMR Integrated Whole-Body PET/MR Scanner*", Journal of Nuclear Medicine, vol. 52, no. 12, pp. 1914-1922, 2011.

[85] D. Beznosko et al., "*Investigation of a solid-state photodetector*", Nuclear Instruments & Methods in Physics Research Section A - Accelerators Spectrometers Detectors and Associated Equipment, vol. 545, no. 3, pp. 727-737, 2005.

[86] C. Labanti et al., "*Design and construction of the Mini-Calorimeter of the AGILE satellite*", Nuclear Instruments & Methods in Physics Research Section A - Accelerators Spectrometers Detectors and Associated Equipment, vol. 598, no. 2, pp. 470-479, 2009.

[87] B. Davin et al., "*LASSA: a large area silicon strip array for isotopic identification of charged particles*", Nuclear Instruments & Methods in Physics Research Section A - Accelerators Spectrometers Detectors and Associated Equipment, vol. 473, no. 3, pp. 302-318, 2001.

[88] G. Di Cocco et al., "*PICsIT detector for gamma-ray astronomy: pixels qualification campaign*", Nuclear Instruments & Methods in Physics Research Section A - Accelerators Spectrometers Detectors and Associated Equipment, vol. 477, no. 1-3, pp. 556-560, 2002.

[89] D. Renker and E. Lorenz, "*Advances in solid state photon detectors*", Journal of Instrumentation, vol. 4, 2009.

[90] W. S. Choong et al., "*A compact 16-module camera using 64-pixel CsI(Tl)/Si P-I-N photodiode imaging modules*", IEEE Transactions on Nuclear Science, vol. 49, no. 5, pp. 2228-2235, 2002.

[91] G. J. Gruber et al., "*A compact 64-pixel CsI(Tl)/Si PIN photodiode imaging module with IC readout*", IEEE Transactions on Nuclear Science, vol. 49, no. 1, pp. 147-152, 2002.

[92] Digirad Corporation, product brochure, www.digirad.com/. Access date: May, 2013.

[93] N. Fukumitsu et al., "*Use of Digirad 2020tc Imager (TM), a multi-crystal scintillation camera with solid-state detectors in one case for the imaging of autografts of parathyroid glands*", Annals of Nuclear Medicine, vol. 15, no. 6, pp. 533-536, 2001.

[94] C. Fiorini et al., "*A monolithic array of silicon drift detectors coupled to a single scintillator for gamma-ray imaging with sub-millimeter position resolution*", Nuclear Instruments & Methods in Physics Research Section A - Accelerators Spectrometers Detectors and Associated Equipment, vol. 512, no. 1-2, pp. 265-271, 2003.

[95] C. Fiorini et al., "*A monolithic array of 77 Silicon Drift Detectors for X-ray spectroscopy and gamma-ray imaging applications*", IEEE Transactions on Nuclear Science, vol. 52, no. 4, pp. 1165-1170, 2005.

[96] C. Fiorini and F. Perotti, "*Small prototype of Anger camera with submillimeter position resolution*", Review of Scientific Instruments, vol. 76, no. 4, 2005.

[97] C. Fiorini et al., "*Present and future Anger Cameras based on Silicon Drift Detectors*", 2007 IEEE Nuclear Science Symposium Conference Record, Vols 1-11, pp. 2318-2322, 2007.

[98] C. Fiorini et al., "*The HICAM Gamma Camera*", IEEE Transactions on Nuclear Science, vol. 59, no. 3, pp. 537-544, 2012.

[99] L. Menard et al., "*Performance characterization and first clinical evaluation of a intra-operative compact gamma imager*", IEEE Transactions on Nuclear Science, vol. 46, no. 6, pp. 2068-2074, 1999.

[100] S. Pitre et al., "*A hand-held imaging probe for radio-guided surgery: physical performance and preliminary clinical experience*", Eur J Nucl Med Mol Imaging, vol. 30, no. 3, pp. 339-343, 2003.

[101] K. Kerrou et al., "*The Usefulness of a Preoperative Compact Imager, a Hand-Held gamma-Camera for Breast Cancer Sentinel Node Biopsy: Final Results of a Prospective Double-Blind, Clinical Study*", Journal of Nuclear Medicine, vol. 52, no. 9, pp. 1346-1353, 2011.

[102] E. Netter et al., "*The Tumor Resection Camera (TReCam), a multipixel imaging probe for radio-guided surgery*", 2009 IEEE Nuclear Science Symposium Conference Record, Vols 1-5, pp. 2573-2576, 2009.

[103] B. W. Miller, "*High-resolution gamma-ray imaging with columnar scintillators and CCD/CMOS sensors, and FastSPCECT III: a third-generation stationary SPECT imager*", PhD thesis, The University of Arizona, 2009.

[104] J. E. Lees et al., "*A high resolution Small Field Of View (SFOV) gamma camera: a columnar scintillator coated CCD imager for medical applications*", Journal of Instrumentation, vol. 6, 2011.

[105] F. J. Beekman and G. A. Vree, "*Photon-counting versus an integrating CCD-based gamma camera: important consequences for spatial resolution*", Physics in Medicine and Biology, vol. 50, no. 12, pp. N109-N119, 2005.

[106] J. W. T. Heemskerk et al., "*An enhanced high-resolution EMCCD-based gamma camera using SiPM side detection*", Physics in Medicine and Biology, vol. 55, no. 22, pp. 6773-6784, 2010.

[107] M. Bergeron et al., "*Performance Evaluation of the LabPET APD-Based Digital PET Scanner*", IEEE Transactions on Nuclear Science, vol. 56, no. 1, pp. 10-16, 2009.

[108] P. Despres et al., "*Investigation of a continuous crystal PSAPD-based gamma camera*", IEEE Transactions on Nuclear Science, vol. 53, no. 3, pp. 1643-1649, 2006.

[109] S. Kim et al., "*Phantom experiments on a PSAPD-based compact gamma camera with submillimeter spatial resolution for small animal SPECT*", IEEE Trans Nucl Sci, vol. 57, no. 5, pp. 2518-2523, 2010.

[110] S. Yamamoto et al., "*Development of a high-resolution Si-PM-based gamma camera system*", Physics in Medicine and Biology, vol. 56, no. 23, pp. 7555-7567, 2011.

[111] R. E. Henkin et al., "*Nuclear Medicine*", Elsevier Mosby, 2nd ed., 2006.

[112] S. Del Sordo et al., "*Progress in the Development of CdTe and CdZnTe Semiconductor Radiation Detectors for Astrophysical and Medical Applications*", Sensors, vol. 9, no. 5, pp. 3491-3526, 2009.

[113] B. Mueller et al., "*Evaluation of a small cadmium zinc telluride detector for scinti-mammography*", Journal of Nuclear Medicine, vol. 44, no. 4, pp. 602-609, 2003.

[114] I. M. Blevis et al., "*CZT gamma camera for scintimammography*", Physica Medica, vol. 21, pp. 56-59, 2006.

[115] http://www.gammamedica.com/, Gamma Medica, Inc. website, MBI-LumaGEM^{TM} product information. Access date: May, 2013.

[116] C. B. Hruska et al., "*Proof of concept for low-dose molecular breast imaging with a dual-head CZT gamma camera. Part II. Evaluation in patients*", Med Phys, vol. 39, no. 6, pp. 3476-3483, 2012.

[117] Y. Eisen et al., "*NUCAM3 - A gamma camera based on segmented monolithic CdZnTe detectors*", IEEE Transactions on Nuclear Science, vol. 49, no. 4, 2002.

[118] M. Tsuchimochi et al., "*A prototype small CdTe gamma camera for radioguided surgery and other imaging applications*", Eur J Nucl Med Mol Imaging, vol. 30, no. 12, pp. 1605-1614, 2003.

[119] X. Llopart et al., "*Medipix2: a 64-k pixel readout chip with 55 mu m square elements working in single photon counting mode*", IEEE Transactions on Nuclear Science, vol. 49, no. 5, pp. 2279-2283, 2002.

[120] P. Russo et al., "*Imaging performance comparison between a LaBr3:Ce scintillator based and a CdTe semiconductor based photon counting compact gamma camera*", Med Phys, vol. 36, no. 4, pp. 1298-1317, 2009.

[121] P. Russo et al., "*Evaluation of a CdTe semiconductor based compact gamma camera for sentinel lymph node imaging*", Med Phys, vol. 38, no. 3, pp. 1547-1560, 2011.

[122] H. Kim et al., "*SemiSPECT: A small-animal single-photon emission computed tomography (SPECT) imager based on eight cadmium zinc telluride (CZT) detector arrays*", Med Phys, vol. 33, no. 2, pp. 465-474, 2006.

[123] A. G. Gasanov et al., "*Effect of Local Heterogeneities on Characteristics of Cumulative Photodetectors in Semiconducting Substrate*", Lett. J. Techn. Phys., vol. 16, no. 1, pp. 14-17, 1990.

[124] V. Golovin, "*Avalanche Photodetector*", Russian Agency for Patents and Trademarks, Patent No. RU 2142175, 1998.

[125] Z. Sadygov, "*Avalanche Detector*", Russian Agency for Patents and Trademarks, Patent No. RU 2102820, 1998.

[126] A. Akindinov et al., "*Scintillation counter with MRS APD light readout*", Nuclear Instruments & Methods in Physics Research Section A - Accelerators Spectrometers Detectors and Associated Equipment, vol. 539, no. 1-2, pp. 172-176, 2005.

[127] Z. Sadygov et al., "*Three advanced designs of micro-pixel avalanche photodiodes: Their present status, maximum possibilities and limitations*", Nuclear Instruments & Methods in Physics Research Section A - Accelerators Spectrometers Detectors and Associated Equipment, vol. 567, no. 1, pp. 70-73, 2006.

[128] T. Frach et al., "*The Digital Silicon Photomultiplier - Principle of Operation and Intrinsic Detector Performance*", 2009 IEEE Nuclear Science Symposium Conference Record, Vols 1-5, pp. 1959-1965, 2009.

[129] N. Anfimov et al., "*Novel micropixel avalanche photodiodes (MAPD) with super high pixel density*", Nuclear Instruments & Methods in Physics Research Section A - Accelerators Spectrometers Detectors and Associated Equipment, vol. 628, no. 1, pp. 369-371, 2011.

[130] J. Ninkovic et al., "*The avalanche drift diode - A back illumination drift silicon photomultiplier*", Nuclear Instruments & Methods in Physics Research Section A - Accelerators Spectrometers Detectors and Associated Equipment, vol. 580, no. 2, pp. 1013-1015, 2007.

[131] W. S. Choong and S. E. Holland, "*Back-Side Readout Silicon Photomultiplier*", IEEE Transactions on Electron Devices, vol. 59, no. 8, pp. 2187-2191, 2012.

[132] K. Yamamoto et al., "*Development of multi-pixel photon counter (MPPC)*", 2007 IEEE Nuclear Science Symposium Conference Record, Vols 1-11, pp. 1511-1515, 2007.

[133] P. Eckert et al., "*Characterisation studies of silicon photomultipliers*", Nuclear Instruments & Methods in Physics Research Section A - Accelerators Spectrometers Detectors and Associated Equipment, vol. 620, no. 2-3, pp. 217-226, 2010.

[134] K. Yamamoto et al., "*Development of Multi-Pixel Photon Counter (MPPC)*", 2006 IEEE Nuclear Science Symposium Conference Record, Vol 1-6, pp. 1094-1097, 2006.

[135] H. Otono et al., "*Study of MPPC at liquid nitrogen temperature*", in proceedings of "International Workshop on new Photon-Detectors", PoS(PD07)007, 2007.

[136] P. Finocchiaro et al., "*Characterization of a Novel 100-Channel Silicon Photomultiplier - Part II: Charge and Time*", IEEE Transactions on Electron Devices, vol. 55, no. 10, pp. 2765-2773, 2008.

[137] Advances in Molecular Breast Imaging, AuntMinnie.com special report, sponsored by GammaMedica, Inc., http://mbipdf.auntminnie.com/. Access date: June, 2013.